Computational Investigations of Ruthenium-Catalyzed Olefin Metathesis and Rhodium-Catalyzed Olefin Hydroboration Reactions

by

Huiling Shao

Bachelor of Science, University of Richmond, 2014

Submitted to the Graduate Faculty of

the Dietrich School of Arts and Sciences in partial fulfillment

of the requirements for the degree of

Doctor of Philosophy

University of Pittsburgh

2019

UNIVERSITY OF PITTSBURGH

DIETRICH SCHOOL OF ARTS AND SCIENCES

This dissertation was presented

by

Huiling Shao

It was defended on

February 28th, 2019

And approved by

Daniel S. Lambrecht, Assistant Professor, University of Pittsburgh

Kazunori Koide, Professor, University of Pittsburgh

Kevin Noonan, Associate Professor, Carnegie Mellon University

Dissertation Advisor: Peng Liu, Assistant Professor, University of Pittsburgh

Computational Investigations on Ruthenium-Catalyzed Olefin Metathesis and Rhodium-Catalyzed Olefin Hydroboration Reactions

Huiling Shao, PhD

University of Pittsburgh, 2019

Transition metal catalysis has proven to be a powerful strategy for olefin functionalization and polymerization reactions. Ancillary ligands play an important role in controlling the reactivity and selectivity of these catalytic reactions. Mechanistically guided rational design of ancillary ligands to achieve desired reaction outcomes has been a long-standing challenge in transition metal catalyzed olefin hydrofunctionalization and metathesis reactions because multiple properties of the ligand, including electron donating ability, steric hindrance, and ligand flexibility, could contribute simultaneously to affect the reaction mechanism, reactivity, and selectivity. To date, development of new catalytic systems has been largely dependent on trial-and-error, as well as chemical intuition. Computational investigation is emerging as an effective tool to provide molecular level understanding of reaction mechanisms, substrate effects, and ligand effects. These theoretical insights can rationalize experimental observations and facilitate ligand design. In this thesis, I present a series of computational studies to probe ligand effects in transition metal catalyzed olefin metathesis and hydroboration reactions. The specific catalytic systems investigated include effects of phosphine ligands on the initiation rate of 2nd generation Grubbs catalyst, effects of switchable *N*-heterocyclic carbene (NHC) ligands on reactivity of Ru-catalyzed ring-opening metathesis polymerization reactions, and effects of NHC, phosphine, and asymmetric phosphite ligands on reactivity, regio-, and stereoselectivity of Rh-catalyzed olefin hydroboration reactions.

As a prerequisite to evaluate ligand effects, computational mechanistic investigations will be conducted for each catalytic reaction to identify the rate- and selectivity-determining transition states. Various computational approaches including ligand distortion energy analysis, steric and electronic ligand parameters, ligand steric contour plots, and linear free energy relationships will then be applied to gain molecular level of understanding in effects of ligands on reactivity and selectivity. The revealed dominating catalyst-substrate interactions and electronic and steric properties of ligands will provide experimental chemists with insights into design of new catalysts with improved catalytic activity, controlled selectivity, and greater substrate scope.

TABLE OF CONTENTS

LIST OF TABLES

LIST OF FIGURES

CHAPTER 1. INTRODUCTION

Transition metal catalysis is an effective strategy to achieve novel reactivity and selectivity in various synthetic organic reactions. With decades of effort, this area is now an essential aspect of modern synthetic organic chemistry with a wide range of applications from academia to industry. The development of new catalytic reactions often relies on a thorough understanding of reaction mechanisms and factors controlling rate and selectivity. Ancillary ligands exemplified by phosphine ligands and N-heterocyclic carbene (NHC) ligands largely contributes to delicate control over reactivity and selectivity of transition metal catalyzed reactions. Modification of ligand structure can often lead to dramatic influences on ligand steric and electronic properties and consequently the reaction outcomes. However, it remains challenging to design ancillary ligands from pure chemical intuition given the complexity of ligand effects - as multiple factors (electron donating ability, steric bulkiness, rigidity, etc.) may all contribute in a transition metal catalyzed reaction. Experimental investigations of reaction mechanisms and ligand effects are also often challenging due to the difficulty in characterization of the short-living reactive organometallic intermediates.

Computational analyses have been widely applied to almost all types of transition metal catalyzed reactions to predict the most favorable reaction pathway, to understand the effects of ligands and substituents, and to provide plausible suggestions to design new catalysts. Although reaction mechanisms of most transition metal catalyzed reactions, exemplified by Rh catalyzed hydroboration reactions, have been well accepted, some mechanistic details like reversibility of elementary steps, substrate effects and ligand effects on reaction mechanism remain unclear.

Through the last few decades, density functional theory (DFT) calculations have evolved to be an important tool to study mechanisms of transition metal catalyzed hydrofunctionalization reactions. The generally accepted procedure to probe the reaction mechanism involves optimization of reaction intermediates and transition states and calculation of energy along a plausible proposed reaction mechanism to construct an energy profile. Conventionally, the proposed reaction mechanism is constructed by well-defined elementary steps containing various competing chemo-, regio-, and enantio- isomeric reaction pathways. The rate- and selectivity- determining steps can be determined by comparing computed Gibbs free energies of each competing pathways. The identified key intermediates and transition states will be further analyzed to provide chemically meaningful interpretation of ligand-controlled reactivity and selectivity in complicated reaction systems and to build predictive models for rational catalyst design. Following computational tools are used in this thesis: electronic and steric ligand parameters, steric contour plots and linear free energy relationships.

In this thesis, I applied various ligand steric and electronic parameters to quantitatively describe the effects of ligand on the reactivity and selectivity of catalytic reactions. For example, Tolman electronic parameter (TEP) is a widely accepted electronic parameter that describes the electron-donating ability of the ligand. It is defined as the symmetric stretching frequency of the C-O bond in tetrahedral Ni(CO)3L. TEP can be determined both experimentally by infrared spectroscopy and computationally by DFT calculations with comparable accuracy.3 Better electron donor ligands have smaller TEP because they increase electron density on the metal center and enhance the CO-metal π back bonding, which weaken the CO vibrational frequency. Other existing electronic ligand parameters, including Lever electronic parameter, trans M-X bond length, ligand dissociation energy, and NMR chemical shifts are also helpful to interpret

experimental results. Ligand steric properties also show crucial influences on the observed reactivity and selectivity. Tolman cone angle, which is defined as the solid angle formed with the metal at the vertex and the hydrogen atoms at the perimeter of the cone, has been widely applied to describe the steric hindrance of the monodentate tertiary phosphine ligands.3 Percent buried volume can be applied to demonstrate the overall bulkiness of both tertiary phosphine and NHC ligands. It is defined as the percentage of the total volume of the first coordination sphere occupied by a ligand.

Ligand distortion and conformation change in transition states are also important factors contributing to reactivity and selectivity. Our group have applied ligand steric contour plots to visualize and rationalize ligand-substrate interactions in key transition states. Ligand steric contour map is derived from the van der Waals surface of the ancillary ligand from the optimized structures of interest. The contour map was created following the previously reported procedure : The optimized molecule is rotated and translated so that the transition metal atom is placed at the origin of the Cartesian coordinate system and the z-axis is oriented along the metal−X bond (X represents center atom of the ancillary ligand). The contour line of zero is drawn through all points on the van der Waals surface having the same z-coordinate as the metal atom. The positive contour lines (colored in green and blue) indicate regions on the ligand van der Waals surface having a positive z-coordinate, i.e., more distant from substrates cis to the ligand and less likely to experience ligand-substrate steric repulsion. Yellow and red indicate regions closer to the substrates cis to the ligand and more significant ligand-substrate steric clashes are expected. The optimized substrate structures could also be embedded on top of the contour plot to create an overlay plot.

Linear free energy relationship (LFER), analog to the Taft equation, is also being applied to describe the quantitative relationship between reactivity/selectivity and ligand parameters to understand ligand effects in transition metal catalysis. This method is important when any single parameter failed to describe a reaction and where both electronic and steric effects are proven significant. Construction of a predictive and quantitative model to describe effects of ligands on reactivity and selectivity of Rh- and Ru-catalyzed olefin functionalization and polymerization reactions can largely help future rational catalyst design by pre-synthetic scanning. Similar predictive model building has been reported by the Sigman group using parameterization-based approach to study effects of ligands on enantioselectivity of Pd-catalyzed coupling reactions.

In this thesis, I present computational studies on Ru-catalyzed ring-opening metathesis polymerization (ROMP), ring-closing metathesis (RCM), and Rh-catalyzed alkene hydroboration reactions. The overall objectives of my studies include investigation of reaction mechanisms, analysis of ligand effects and construction of predictive models.

- Chapter 2 demonstrates a computational investigation on effects of aminophosphine ligand initiation rate of in Ru- olefin metathesis catalyst.
- Chapter 3 presents a series of DFT analysis on effects of photo- and redox- switchable ligands on reactivity and selectivity of Ru-catalyzed ROMP and RCM reactions.
- Chapter 4 presents a computational study on effects of photo-switchable NHC ligands on reaction mechanism, reactivity and regioselectivity in Rh-catalyzed hydroboration reactions.
- Chapter 5 demonstrates reaction mechanism of Rh-catalyzed directed catalytic asymmetric hydroboration of aryl olefins and identifies effects of ligand on enantioselectivity and effects of directing group on regioselectivity.

CHAPTER 2. DISENTANGLING LIGAND EFFECTS ON METATHESIS CATALYST ACTIVITY: EXPERIMENTAL AND COMPUTATIONAL STUDIES OF RUTHENIUM–AMINOPHOSPHINE COMPLEXES

A significant part of this chapter was published as Chu, C. K., Lin, T. P.; Shao, H.; Liberman-Martin, A. L.; Liu, P.; Grubbs, R. H. *Journal of the American Chemical Society*, **2018**, *140*(16), 5634-5643. In this work, I designed and carried out DFT calculations and analysis of computational results. Experimental synthesis of catalysts and kinetic studies were carried out by Chu, C.K. and Lin, T. of the Grubbs, R. H. group at California Institute of Technology.

2.1 INTRODUCTION

Olefin metathesis reactions, exemplified by ring-opening metathesis polymerization (ROMP), have enabled the synthesis of new functional materials[1] and have led to important industrial applications.[2 3 4] Ru-alkylidene complex represents one of the most important olefin metathesis catalyst since first discovery of **G1** by Grubbs in 1995 (Figure 1a).[5] The lower reactivity of G1 in comparison to molybdenum catalysts was later addressed through the development of second-generation ruthenium olefin metathesis catalysts, notably **G2**,[6] in which a phosphine is substituted with an 1,3-dimesitylimidazol-2-ylidene (IMes) ligand.[7,]

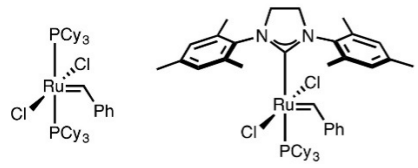

G1 G2

Figure 1. Established Ru alkylidene olefin metathesis catalysts

The initiation mechanism of Ru-catalyst has been probed both experimentally and computationally. Mechanistic studies of olefin metathesis promoted by second-generation ruthenium catalysts have suggested that these reactions occur via a dissociative mechanism, in which phosphine dissociation occurs to form a 14-electron intermediate in an initiation step prior to olefin binding (Figure 2).[8,9] The activity of these catalysts is affected by the rate of phosphine dissociation (k_1; initiation rate) and the relative rate of phosphine reassociation (k_{-1}), and consequently the electronic and steric properties of the PR_3 ligand.[10]

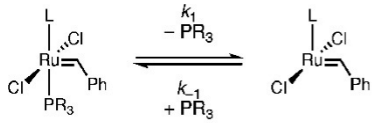

Figure 2. Proposed dissociative mechanism of G2 catalyst

Although the dissociative mechanism is well accepted, the effect PR_3 ligand on catalyst initiation rate is less investigated. Our collaborator at Grubbs group synthesized a series of second-generation ruthenium olefin metathesis catalysts bearing aminophosphine ligands in place of the tricyclohexylphosphine present in catalyst **G2**. (Figure 3)

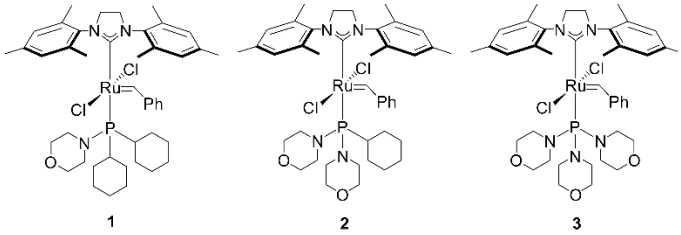

Figure 3. Structures of morpholino substituted Ru alkylidene complex 1-3

In order to understand effects of morpholino substitution on the strength of phosphine binding in second-generation ruthenium catalysts (**1** - **3**), our collaborator conducted a series of kinetic experiments to determine phosphine dissociation rate constant (k_1), phosphine

reassociation rate constants (k_{-1}), and dissociation equilibrium constant (K_{assoc}). All values are normalized with respect to the highest value in each data set (denoted by shading). (Figure 4) Increasing the number of morpholino substituents causes a steady increase in initiation rates when comparing catalysts **G2**, **1**, and **2**. However, the tris(morpholino)phosphine ligand dissociates at a significantly slower rate leading to a U-shaped trend in phosphine association constants.

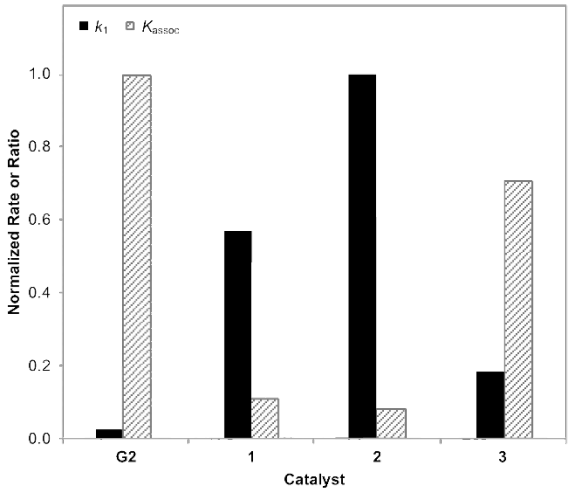

Figure 4. Comparisons of k_1 and K_{assoc} for catalyst series bearing G2 and morpholinophosphine ligands (1–3)

The goal of computational studies in this chapter is to gain understanding of the electronic and steric properties of the morpholinophosphine ligands. The interesting U-shaped trends of K_{assoc} do not correlate well with inductive effects expected with morpholino substituents. For example, the tris(morpholino)phosphine ligand (**L3**) is the most electron deficient ligand in the series due to the inductive effect of more electronegative atoms and is expected to dissociate at the highest rate. However, the observed U-shaped trends of K_{assoc} suggested **L3** dissociates at a significantly slower rate comparing to mono(morpholino) ligand (**L1**) and di(morpholino) ligand (**L2**). Experimental observations suggested that multiple factors including ligand-ligand steric repulsion, ligand conformation change, and inductive effects could contribute to the observed phosphine

dissociation rate. To be more specific, I study the inductive effects of the ligand by computed Tolman electronic parameters (TEP) and investigate ligand distortion when bonded onto Ru-catalyst. The ligand-ligand steric repulsion will then be analyzed by evaluation of the optimized catalyst geometries. The higher dissociation rate (k_1) of **2** comparing to **1** will also be analyzed by computational study of the phosphine dissociation transition state. The gained molecular level of understanding shall provide further guidance for future design of efficient ruthenium olefin metathesis catalysts.

2.2 COMPUTATIONAL METHODS

Geometry optimizations of complexes **G2**, **1-3**, and the corresponding phosphine ligands were performed using M06[11] functional, with the def2SVP basis set.[12] Single point energies were calculated using M06 with the def2TZVP basis set. Solvation effects were considered by performing single point calculations with the SMD model[13] in toluene ($\varepsilon = 2.38$)[14]. All calculations were performed with Gaussian 09.[15] The reported Gibbs free energies and enthalpies include zero-point vibrational energies and thermal corrections at 298K. The quasiharmonic approximation from Cramer and Truhlar[16] was applied to compute the vibrational entropies. In the quasiharmonic approximation, vibrational frequencies lower than 100 cm^{-1} were raised to 100 cm^{-1} as a way to avoid spurious results associated with the harmonic-oscillator model for very low-frequency vibrations.[17]

Tolman electronic parameterswere calculated with model complex $Ni(CO)_3L$ using B3LYP[18] and a mixed basis set of LANL2DZ for Ni and 6-31G(d) for other atoms.[19] The

computed A_1 stretch frequency was reported with a scaling factor of 0.962.[20] To reduce computational cost, structures in the reaction coordinates (Figure 7) were optimized using B3LYP and a mixed basis set of LANL2DZ for Ru and 6-31G(d) for other atoms. Single point energies were performed using M06 and a mixed basis set of SDD for Ru and 6-311+G(d,p) for other atoms.

2.3 DFT-OPTIMIZED GEOMETRIES AND COMPUTED PHOSPHINE DISSOCIATION ENERGIES FOR MORPHOLINOPHOSPHINE RU- CATALYSTS

2.3.1 Structure and conformational flexibility of L2

The morpholine-containing catalysts **1**−**3** investigated via computational studies to understand factors affecting phosphine dissociation energies.[21] Catalyst **2**, ligated with cyclohexyl-bis(morpholino)phosphine **L2**, was of special interest since it is the fastest-initiating complex of both series. The structure and conformational flexibility of **L2** were studied by DFT calculations. Two conformations were identified for the morpholinophosphine ligand, with varied orientation of substituents in relation to the phosphorus lone pair, positioned along the z-axis.[22] These low-energy conformations are consistent with the conformation of the PCy3 ligand in crystal structures.[23] Conformation A, which is less stable in the case of the free ligand, contains a morpholine substituent that is coplanar with the phosphorus xy-plane (Figure 5). The ring in this position will be referred to as the "coplanar" substituent. In conformation A, the nitrogen lone pair of the coplanar ring is anti-periplanar to the phosphorus lone pair. Previous spectroscopic studies of aminophosphines have suggested that one nitrogen lone pair must take an unprivileged

orientation, resulting in a repulsive, pseudo-π interaction with the phosphorus lone pair.[24] The lone pair−lone pair repulsive interaction results in conformation A being the less stable conformer. Furthermore, the orthogonal cyclohexyl ring present in this ligand conformation exhibits significant steric clash with both morpholine rings. In comparison, conformation B contains two orthogonal morpholine rings and a coplanar cyclohexyl ring with respect to the phosphorus xy-plane, and is the favored conformation for the free phosphine.

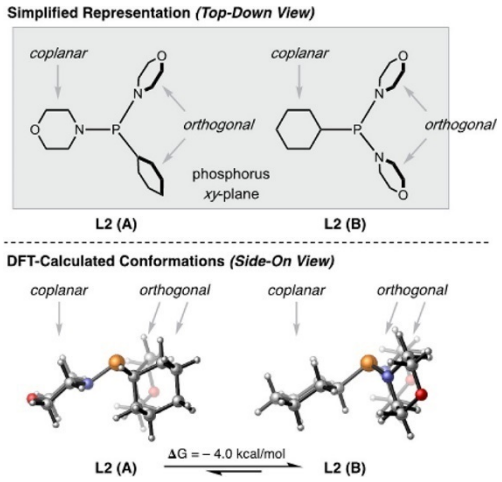

Figure 5. Two perspectives of conformations A and B of ligand L2 and the computed relative energies

2.3.2 Effects of aminophosphine ligand on association constants, K_{assoc}

In order to provide insight into the origin of the relative aminophosphine association constants, K_{assoc}, shown in Figure 4, the DFT-optimized geometries (Figure 6) as well as the Gibbs free energies (ΔG_d) and enthalpies (ΔH_d) of phosphine dissociation (Table 2), were computed for parent catalyst **G2** and complexes **1**–**3**. Ligand dissociation energies ΔG_d and ΔH_d are defined as the Gibbs free energy and enthalpy differences, respectively, between the optimized catalyst and the 14-electron complex plus the free phosphine. Ligand distortion energy ($\Delta E_{distort}$) is defined as the energy difference between the metal-bound phosphine ligand geometry and the optimized free

ligand geometry. The calculated ΔG_d and ΔH_d values agree with the U-shaped trend from experimentally determined K_{assoc}; lower phosphine dissociation energies were calculated for complexes **1** and **2** in comparison to **G2** and **3**. The optimized catalyst structures depict variations in ligand conformation and steric repulsions between the coplanar phosphine substituent and the NHC mesityl group. We surmised that the U-shaped trend in phosphine dissociation energy is the combined result of these factors as well as inductive effects derived from increased heteroatom incorporation. Therefore, this section presents a detailed computational analysis of the contributions of these individual factors.

The parent complex **G2**, bearing a PCy3 ligand, displays an unfavorable steric interaction between the NHC mesityl and the coplanar cyclohexyl ring (Figure 6). Similarly, in complex **1**, a coplanar cyclohexyl ring is oriented toward the N-mesityl, this conformation is corroborated by the crystal structure of the analogous monopiperidinophosphine-ligated identified by our experimental collaborator. These steric clashes between the P-cyclohexyl and N-mesityl promote phosphine dissociation from catalysts **G2** and **1**; the lower ΔG_d of **1** can be attributed to the inductive effect of the morpholine substituent leading to lower phosphine donor strength. In contrast, the optimized structures of complexes **2** and **3** both contain a coplanar morpholine ring oriented toward the *N*-mesityl. The decreased pyramidalization of the morpholine nitrogen atom compared to the cyclohexyl carbon leads to smaller phosphine-NHC repulsions in **2** and **3** compared to the repulsions observed in **G2** and **1** (Figure 6).

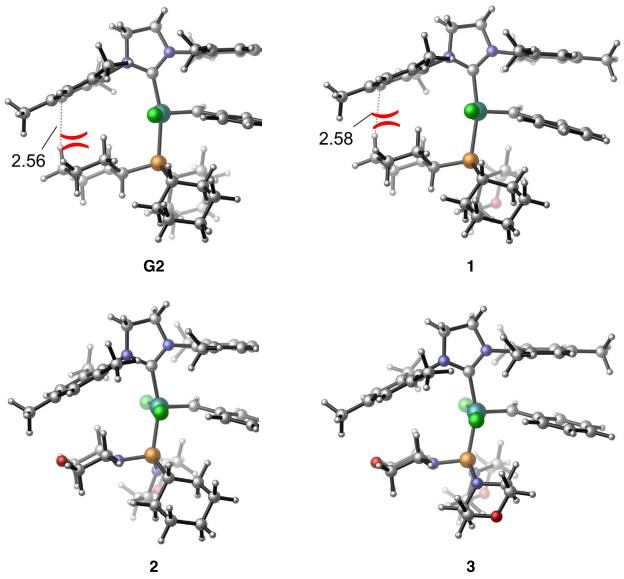

Figure 6. DFT-optimized structures for complexes G2 and 1–3 depicting steric repulsions between the N-mesityl and P-cyclohexyl groups in G2 and 1 and the preferred ligand conformations in 1 and 2

While dissociation of ligands with more cyclohexyl substituents (e.g. **G2** and **1**) is promoted by steric interactions, the dissociation of ligands with more morpholine substituents (e.g. **2** and **3**) is promoted by inductive effects of the nitrogen atoms, which decrease the donor ability of the phosphorus lone pair. This electronic effect is corroborated by the computed Tolman Electronic Parameter (TEP) values for PCy3 and **L1**–**L3** (Table 1). The TEPs are computed in the gas phase in $Ni(CO)_3L$, and the computed frequencies are scaled with a scaling factor of 0.962. As discussed in section 2.4.1, conformation A contains a morpholine ring coplanar to the phosphorus *xy*-plane, whereas conformation B features a coplanar cyclohexyl ring, (Figure 5). TEP values that correspond to the preferred phosphine conformations in complexes **G2** and **1–3** are highlighted in bold. As expected, morpholine substitution increases TEP values within a single ligand conformation, indicating decreased phosphine donor strength. For ligands **L1** and **L2**, two different conformations, which contain either a coplanar morpholine (A) or a coplanar cyclohexyl group

(B) were individually considered. In these cases, conformation A, which features anti-periplanar geometry of the nitrogen and phosphorus lone pairs, exhibits higher phosphine donor strength than conformation B.[25] Thus, the donor ability of the phosphine ligand is dependent on both inductive effects and the preferred ligand conformation in the catalyst. The lowest energy phosphine ligand conformations in complexes **1** and **2**, **L1(B)** and **L2(A)**, have similar TEP values (2064.3 cm^{-1} and 2063.5 cm^{-1}, respectively), suggesting that these two ligands have similar donor strength. Nonetheless, the phosphine donor strength alone cannot explain the dissociation energy trend. While complex **3** exhibits the strongest inductive effects expected to promote phosphine dissociation, a relatively high ΔG_d is observed, indicating the significant contributions of other factors, notably steric interactions and ligand distortion, in promoting ligand dissociation.

Table 1. Calculated Tolman Electronic Parameter (TEP) Values of Phosphine Ligands.

	Conformation A	**Conformation B**
ligand	TEP (cm^{-1})	TEP (cm^{-1})
PCy_3	---	**2060.0**
L1	2058.5	**2064.3**
L2	**2063.5**	2068.3
L3	**2068.3**	---

Distortion of the aminophosphine ligand is another factor that promotes phosphine dissociation. The computed ligand distortion energies ($\Delta E_{distort}$) in complexes **G2** and **1**–**3** clearly indicate more significant distortion of ligand **L2** in complex **2** compared to those of the other phosphine ligands (Table 2). The enhanced distortion of **L2** is due to a conformational change upon binding to the ruthenium center. In comparison to the free ligand, the metal-bound ligand **L2** adopts a higher energy conformation with a coplanar morpholine ring (Conformation A, Figure 5) to minimize steric clashes with the NHC mesityl group. Thus, while it does not exhibit the

phosphine-NHC steric interactions that promote phosphine dissociation in complexes **G2** and **1**, complex **2** has a low ΔG_d due to a significant contribution from ligand distortion energy.

The computational analysis thus revealed that the combined contributions from steric interactions, inductive effects, and ligand distortion result in the U-shaped trends in K_{assoc} and ΔH_d. Accounting for the key promoters of ligand dissociation for each complex, listed in Table 2, provides an explanation for this trend. "Steric" refers to aforementioned steric repulsions between the coplanar cyclohexyl ring on the phosphine ligand and the NHC mesityl group. "Inductive" describes the inductive effect arising from electron-withdrawing morpholine substituents. "Distortion" refers to distortion of the phosphine ligand in the catalyst.

Ligand dissociation is promoted in **G2** and **1** by phosphine-NHC steric repulsions, and ΔH_d is further reduced in **1** due to inductive effects of the morpholine substituent. Dissociation from complex **2** is promoted by inductive effects and greater distortion of the phosphine ligand. The dissociation from complex **3** is promoted by increased inductive effects; however, significant contributions from phosphine-NHC steric interactions and ligand distortion are not observed to promote the dissociation of **L3**.

Table 2. Calculated Phosphine Ligand Dissociation (ΔG_d, ΔH_d) and Distortion ($\Delta E_{distort}$) Energies.

catalyst	ΔG_d (kcal/mol)	ΔH_d (kcal/mol)	$\Delta E_{distort}$ (kcal/mol)	Promoters of Ligand Dissociation
G2	12.6	30.3	2.9	Steric
1	9.9	27.8	2.7	Steric, Inductive
2	9.5	27.6	5.7	Inductive, Distortion
3	11.9	29.2	1.9	Inductive

2.4 MODELING OF THE REACTION COORDINATE OF LIGAND DISSOCIATION FOR FAST-INITIATING CATALYST 2

Computational studies of the reaction coordinate for phosphine ligand dissociation along dissociative mechanism were performed to determine the origin of the high initiation rate for catalyst **2**, and the reason for faster phosphine dissociation for **2** in comparison to **1**. The reaction coordinate diagrams for the dissociation of catalysts **1** and **2** are created by optimization of series of Ru-complexes with fixed Ru-P distance. (Figure 7) The corresponding ligand conformation is designated in parentheses (see Figure 5). Both conformations A (more distorted with a coplanar morpholine ring) and B (less distorted with a coplanar cyclohexyl ring) are considered for catalyst 2. The lowest-energy dissociation pathway of catalyst 2 follows the solid line, starting from conformation A and continuing on to conformation B at longer Ru–P distances.

While ligand **L1** in catalyst **1** maintains the same conformation (B) throughout the dissociation process, **L2** undergoes a conformational change after the Ru–P distance is elongated to greater than 3.0 Å. As discussed above, in the ground state of catalyst **2**, **L2** adopts the more distorted conformation A ($\Delta E_{distort}$ = 5.7 kcal/mol) to minimize phosphine-NHC steric repulsions. As the Ru–P bond lengthens during phosphine dissociation, the phosphine-NHC repulsion diminishes, and thus the less distorted conformation B becomes more favorable. Although location of the phosphine dissociation transition states was not successful, the computed reaction coordinate diagrams suggest that the dissociation of **L2** is kinetically more favorable than that of **L1** due to the adoption of a lower energy conformation of **L2** in the transition state region. Therefore, the stabilizing effect resulting from this conformational change from A to B is proposed to be the

reason that catalyst **2** has a higher rate of phosphine dissociation (k_1) than **1** and is the fastest-initiating catalyst in the series.

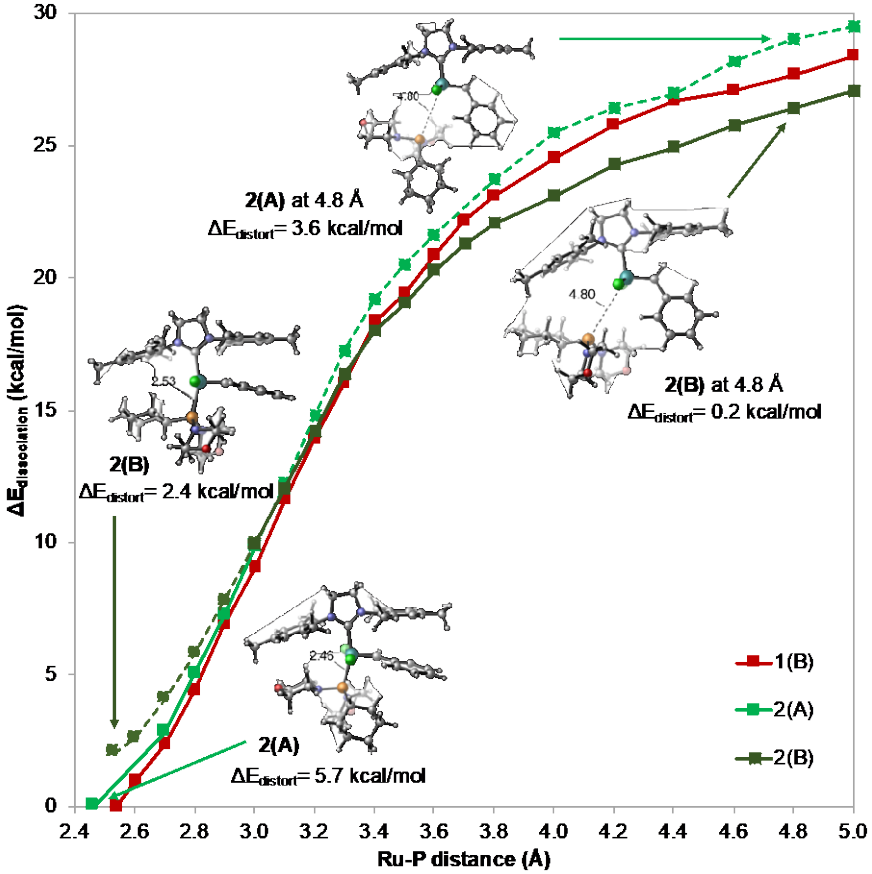

Figure 7. Reaction coordinate diagrams of phosphine ligand dissociation for catalysts 1 and 2

2.5 SUMMARY

Due to the complexity of the ligand effects, multiple computational tools are applied to disentangle the effects of ligands on observed U-shaped trends in K_{assoc} and ΔH_d . For example, Tolman electronic parameter is computed to quantify the inductive effects of morpholinophosphine ligand. Ligand conformational changes, evidenced by computed $\Delta E_{distort}$, lead to rapid dissociation of the fastest-initiating catalyst **2** of these series, which bears a

cyclohexyl-bis(morpholino)phosphine ligand **L2**. Overall, computational analysis presented in this chapter revealed that the combined contributions from steric interactions, inductive effects, and ligand distortion result in the U-shaped trends in K_{assoc} and ΔH_d. Take the complex **3** with tri(morpholino)phosphine ligand **L3** for example, although electronic inductive effect promotes dissociation of **L3**, lack of significant contributions from phosphine-NHC steric interactions and ligand distortion lead to the overall slow initiation rate. Computational investigation on the ligand dissociation transition states with **L1** and **L2** revealed that ligand conformation change in transition state further promotes the initiation rate of catalyst **2**. Studies presented in this chapter revealed important considerations for designing efficient ruthenium olefin metathesis catalysts. (Figure 8)

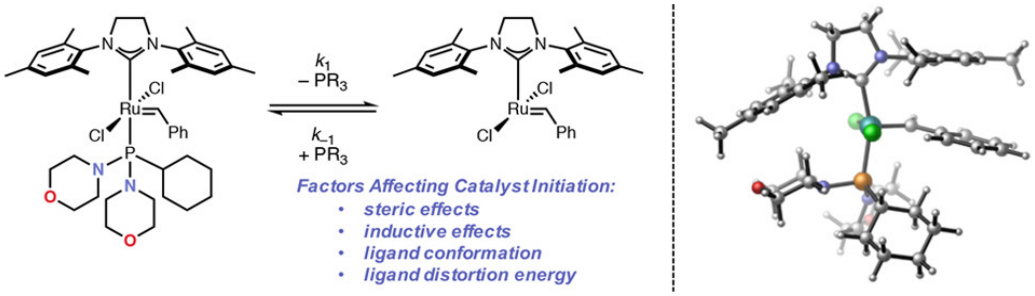

Figure 8. Key factors contributing to Second-generation ruthenium olefin metathesis catalyst initiation

CHAPTER 3. EFFECTS OF PHOTO- AND REDOX-SWITCHABLE LIGANDS IN RU-CATALYZED RING-OPENING METATHESIS POLYMERIZATION AND RING-CLOSING METATHESIS REACTIONS

A significant part of this chapter were published as Teator, A. J.; Shao, H.; Lu, G.; Liu, P.; Bielawski, C. W. *Organometallics*, **2017**, 36(2), 490-497; Lastovickova, D. N.; Shao, H.; Lu, G.; Liu, P.; Bielawski, C. W. *Chem. Eur. J.* **2017**, 23, 5994-6000; Lastovickova, D. V.; Teator, A. J.; Shao, H.; Liu, P.; Bielawski, C. W. *Inorg. Chem. Front.* **2017**, 4, 1525-1532. In this work, I designed and carried out DFT calculations and analysis of computational results. Experimental synthesis of catalysts and kinetic studies were carried out by Lastovickova, D. N. and Teator, A. J. of Bielawski, C. W. at University of Texas at Austin (Currently at UNIST in South Korea).

3.1 INTRODUCTION

Historically, improvements to existing homogeneous catalysts have focused on enhancing intrinsic catalytic properties, such as activity, selectivity, and/or functional group tolerance. An ability to "switch" the performance displayed by a catalyst over the course of a reaction could facilitate access to products with uniquely tailored structures or properties that vary in response to changing environments. Such enhanced control over reaction pathways has fueled the field of switchable catalysis, whereby stimuli responsive functional groups are incorporated into known catalysts.[26] (Figure 9) The switchable ancillary ligand controls the catalyst activity by through bond electronic effects and through space steric repulsions. Computational investigation on electronic and steric properties of switchable ligands and the effects of ligands on reactivity could potentially impede advanced switching functions to alternate monomer selection and achieve copolymerization with defined microstructure.

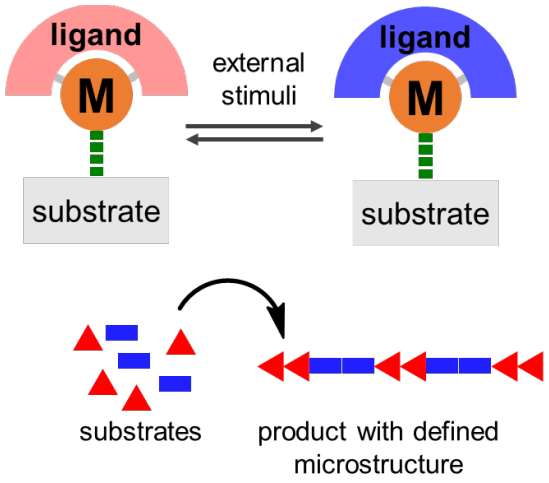

Figure 9. Effects of switchable ligands on product selectivity

In recent years, a variety of switchable catalytic methods have been disclosed, however, few examples have been reported that involve modulation of the activities displayed by transition-metal-based catalysts.[27] Our collaborator, the Bielawski group, successfully incorporated photo- and redox-switchable *N*-heterocyclic carbene (NHC) ligands onto Ru olefin metathesis catalyst. Two switchable catalysts have been subsequently applied in ring-opening metathesis polymerization (ROMP) and ring-closing metathesis (RCM) reactions to explore the catalyst-controlled reactivity and monomer selectivity.

Although the proposed reaction mechanisms of Ru-catalyzed ROMP (Figure 10) and RCM (Figure 11) reactions are generally accepted, the rate-determining transition state and resting state remain substrate dependent. [28] From the Dewar–Chatt–Duncanson adduct [29] (**1**), [2+2] cycloaddition (**TS1**) takes place to form the fused bicyclic metallacyclobutane intermediate (**2**). The 4-membered ring is then cleaved through a retro [2+2] cycloaddition (**TS2**) and the coordination of another cycloalkane regenerates **3**. Ring strain energy of the fused metallacyclobutane intermediate is a key factor to determine RDS. In 2012, Cramer and Hillmyer published a series of study on the computed energies of the intermediates and transition states of

the ROMP of norbornene, cyclopentene, cycloheptene, and Z-cyclooctene. Their results indicated **TS2** to be barrierless with norbornene substrate, and a very low barrier of 1.4 kcal/mol with cyclopentene, and thus making **TS1** the RDS. In case of substrates with larger rings such as cycloheptene and Z-cyclooctene, **TS2** became rate-determining due to the smaller strain-release in **TS2** and the increased steric repulsion between substrate and the ligand in **TS1**. [30]

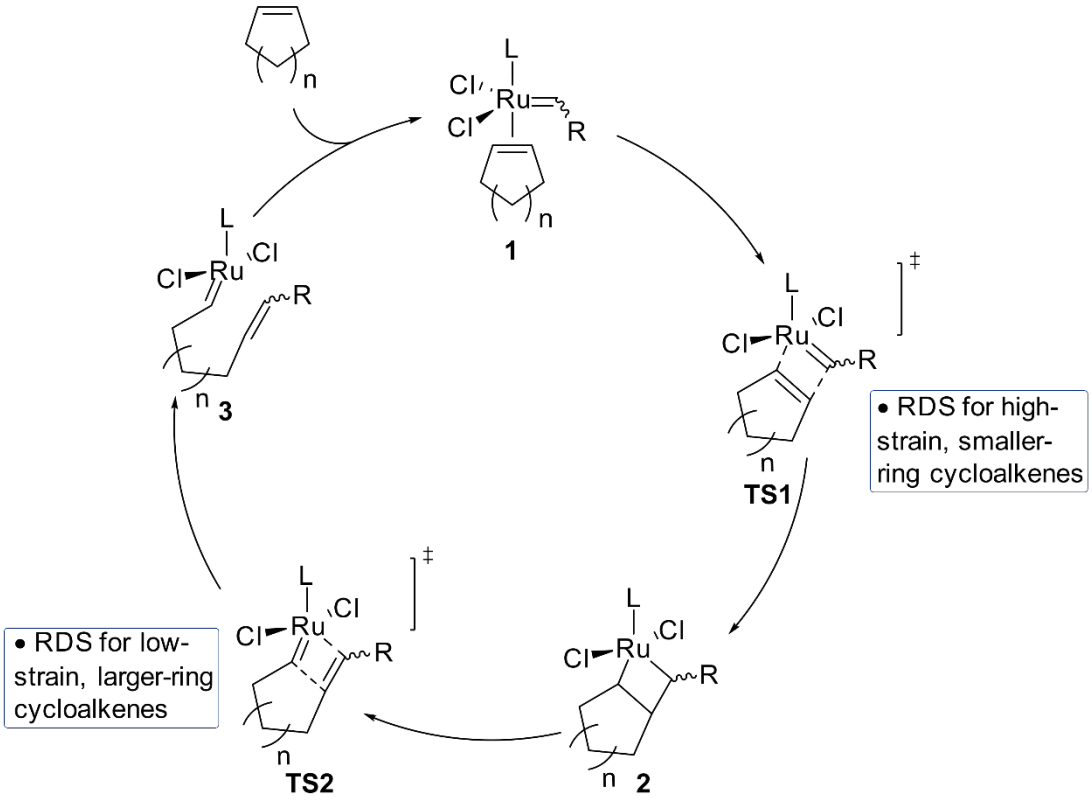

Figure 10. Proposed mechanism and RDS of Ru-catalyzed ROMP of cycloalkenes

Similarly, the proposed reaction mechanism of Ru-catalyzed RCM reactions initiates from **4** with the intramolecular [2+2] cycloaddition (**TS3**) to form the metallacyclobutane (**5**) followed by the metallacyclobutane cleavage (**TS4**). Then the product cycloalkane is released through ligand dissociation from **6**. **4** is then regenerated through an olefin metathesis and the release of an ethylene. In 2011, Hillier and Percy reported the computational studies of a series of α, ω - dienes

that lead to 5-10 membered ring products and the observed RDS for all substrates are the metallacyclobutane cleavage **TS4**.[31] Effects of different ancillary ligands on the relative stability of the metallacyclobutane intermediates have also been investigated. The 14-electron d^4-Ru(IV) center of metallacyclobutane is electron deficient. Previous studies have also concluded the stronger σ-donating NHC ligands stabilizes the metallacyclobutane intermediates comparing to PPh_3 ligands, which suggested the effects of switchable ligand on ruthenacyclobutane intermediate may also contribute to the observed reactivity trend.[32]

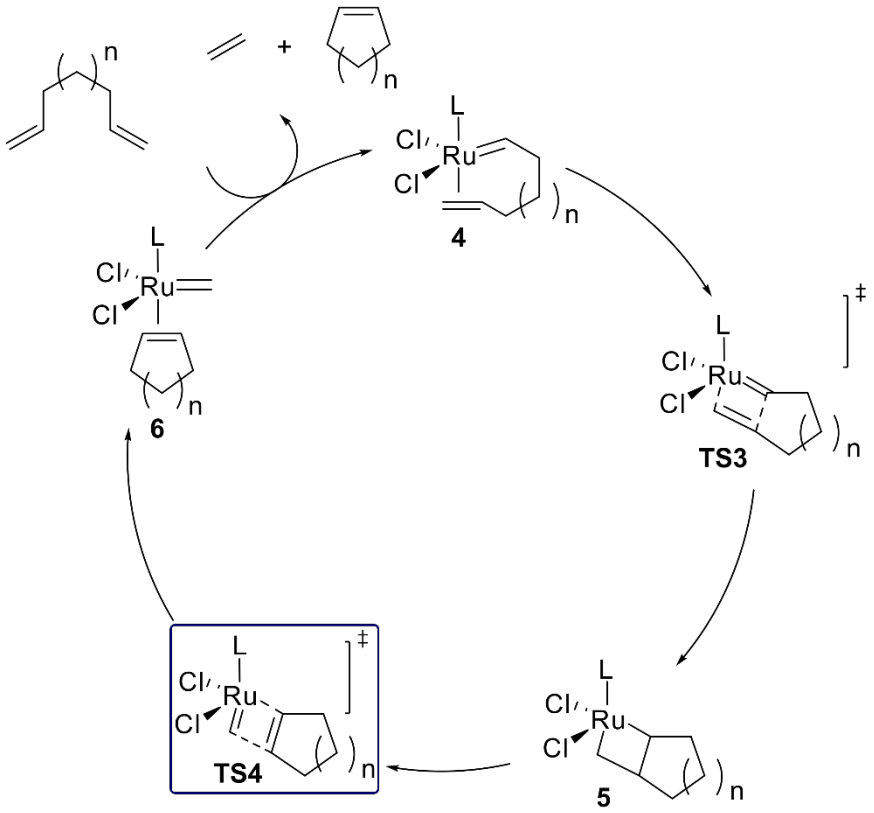

Figure 11. Proposed mechanism and RDS of Ru-catalyzed RCM of α, ω -dienes

In this chapter, I report the first computational analysis on effects of photo- and redox-switchable NHC ligands on the reactivity of Ru-catalyzed ROMP and RCM reactions. Bielawski group [33] and others [34] have demonstrated that the photoinduced electrocyclization of an *N*-

heterocyclic carbene bearing an annulated photochromic [35] dithienylethene (DTE) [36] unit significantly altered the donating ability of the ligand. The photo-cyclized NHC ligand **L1**$_{closed}$ under UV light is proven to be a better donor ligand comparing to the open ligand **L1**$_{open}$, evidenced by the experimental and computed Tolman electronic parameters (TEPs). Building on those results, Bielawski group reported the first photoswitchable olefin metathesis catalyst[37,38] that can be reversibly toggled between two states (**7**$_{open}$ and **7**$_{closed}$) using light and demonstrate the remote modulation of its intrinsic activity in ROMP and RCM reactions (Figure 12). Similar photoswitchable NHC ligand was also incorporated on an Rh-based catalyst to control the reactivity of hydroboration reactions. (Chapter 4)[39]

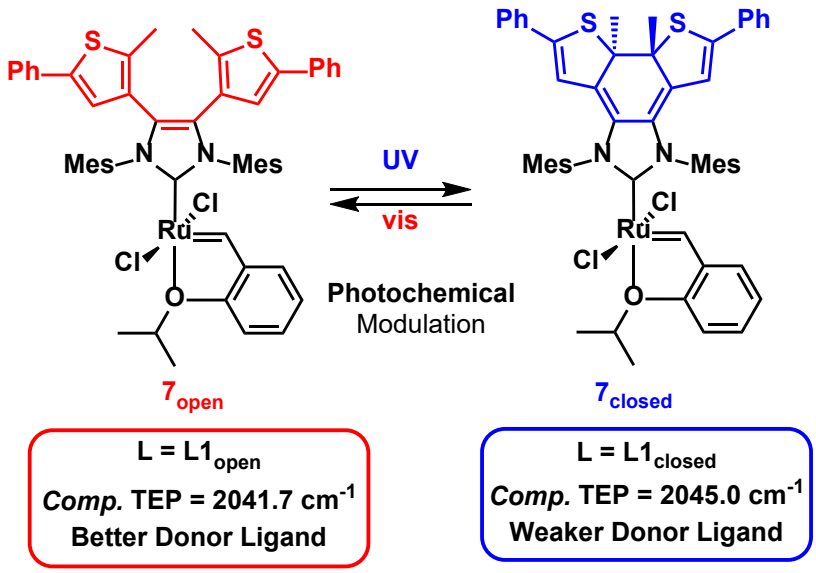

Figure 12. Ru-olefin metathesis catalyst bearing photo-switchable NHC ligand

Kinetic studies on photo-modulated reactivity of ROMP of cyclooctadiene (COD), norbornene derivative **11**, and RCM of **9** to form disubstituted olefin **10** are summarized in Figure 13. Catalyst **1**$_{closed}$ bearing weaker donor ligand **L1**$_{closed}$ facilitates the RCM reaction, evidenced by the observed rate difference (k_c/k_o = 2.1) between the ring-closed and ring-open catalysts. (Figure 13a) Conversely, in ROMP of COD, the relative activities displayed by **2o** and **2c** (k_c/k_o = 0.66)

were opposite to those observed in the aforementioned RCM reactions, which indicated that the effects of ligand could be substrate and reaction dependent. (Figure 13b) In ROMP of norbornene derivative **11**, observed rate difference (k_c/k_o = 0.56) shows same trend as in ROMP of COD. As previous mechanistic studies reported, the rate determining step of ROMP of norbornene derivative **11** is likely to be different from that of ROMP of COD, it is interesting to investigate how ligand effects contribute to different rate determining step with different substrates.

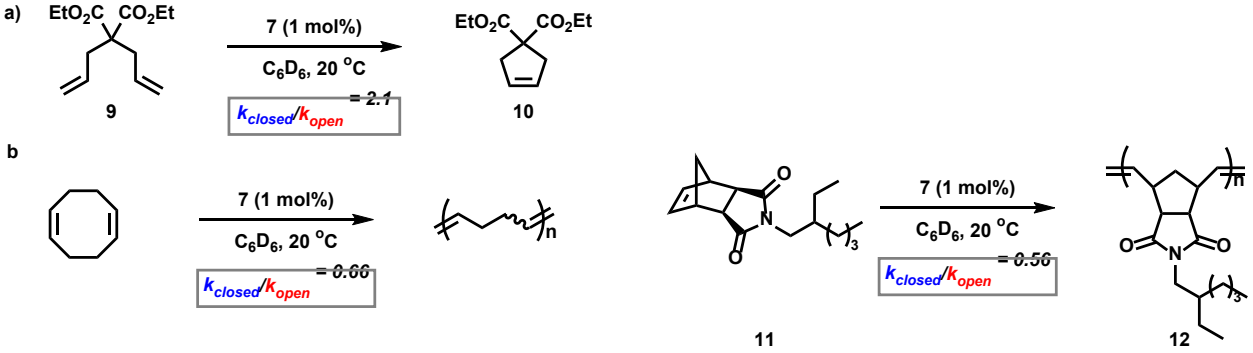

Figure 13. Experimental observed effects of photoswitchable NHC ligand on reactivity of a) RCM of distributed olefin 10 and b) ROMP of COD and norbornene derivative 11

Redox-switchable catalysis is also appealing as many complexes feature multiple oxidation states, each of which may display a unique activity and/or selectivity. Incorporation of a quinone-annulated[40] *N*-heterocyclic carbene[41] into a catalytically active Ru center is being synthesized by our collaborator Bielawski group. The electron donor ability of the NHC ligand increases significantly upon reduction, evidenced by the computed TEPs.[42] (Figure 14) As Ru-catalyzed olefin metathesis reaction reactivity and monomer selectivity are largely controlled by ligand electron donating abilities, different monomers may be selectively polymerized in a manner that depends on the oxidation state of the NHC ligand and potentially lead to redox-controlled copolymerization from a mixture of monomers.

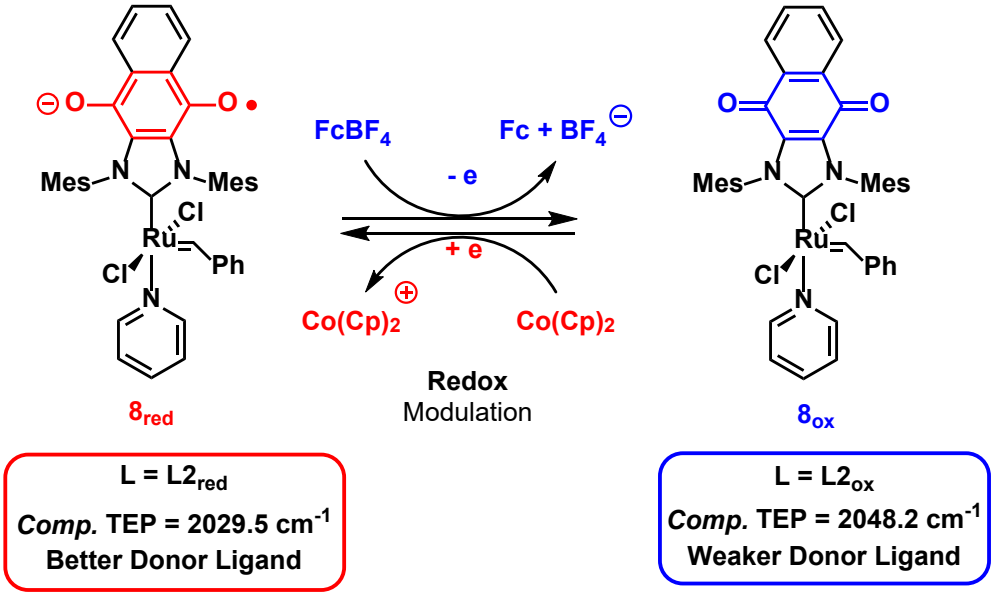

Figure 14. Ru-olefin metathesis catalyst bearing redox-switchable NHC ligand

Experimental kinetic investigations by our collaborator Bielawski group are presented in Figure 15. Consistent with the photo-modulated RCM reaction, catalyst **8ox** bearing weaker donor neutral ligand (**L2ox**) facilitates the RCM reaction at a faster rate comparing to the neutral catalyst **8ox** (k_{ox}/k_{red} = 6.7). (Figure 15a) They also explored the catalytic activities displayed by **8ox** and **8red** in ROMP reactions. In ROMP of norbornene derivative **11**, observed rate difference (k_{ox}/k_{red} = 0.19) indicated better donor ligand (**L2red**) promotes the reactivity. Alternatively, in ROMP of COD, the relative activities displayed by **8ox** and **8red** (k_{ox}/k_{red} = 3.7) were opposite to those observed in the aforementioned photo- modulated catalytic system. This suggested that on top of electron donor ability of the ligand, other factors such as ligand steric repulsion or ligand distortion energy may also contribute to the reactivity trend. (Figure 15b)

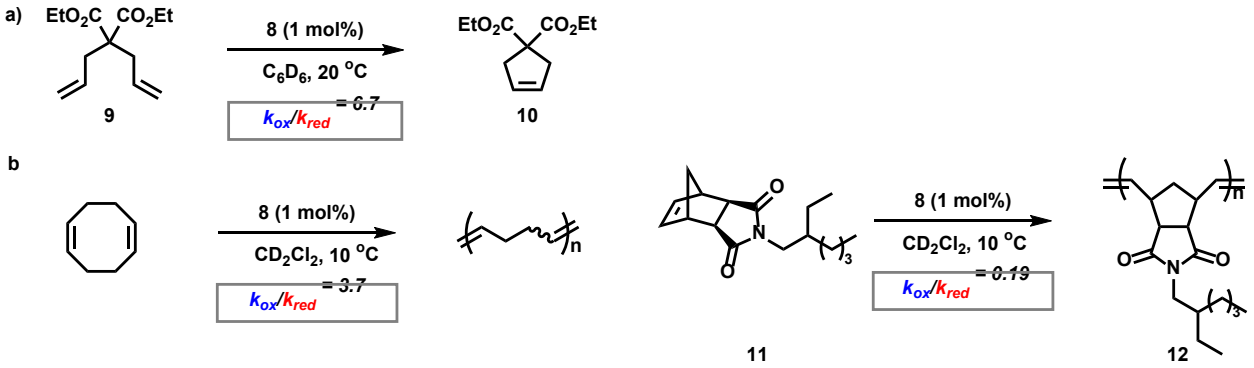

Figure 15. Experimentally observed effects of redox-switchable NHC ligands on reactivity of a) RCM of distributed olefin 9 and b) ROMP of COD and norbornene derivative 11

The overall goal of this chapter is to conduct computational analysis to elucidate effects of the photo- and redox-switchable ligands on reactivity of Ru-catalyzed ROMP and RCM reactions. This chapter aims to gain molecular level of understanding of the electronic and steric properties of the photo- and redox- switchable NHC ligands and consequently the effects of ligands on the experimentally observed reactivity trends.[43] As previous computational studies pointed out, the rate-determining transition state and catalyst resting states are substrate-dependent. As a result, the electronic properties of the NHC ligand along cannot explain the observed reactivity trends. For example, with photo-switchable catalyst **1**, the better donor ligand $\mathbf{L1_{open}}$ promotes reactivity of Ru-catalyzed ROMP of COD; conversely, with redox-switchable catalyst **8**, the weaker donor ligand $\mathbf{L2_{ox}}$ promotes reactivity of Ru-catalyzed ROMP of COD. This interesting observation suggested on top of electronic donor ability, other properties of the switchable ligands may also contribute to the reactivity trend. The achieved mechanistic insights on factors controlling rate and substrate selectivity in Ru-metathesis reactions are expected to aid the design of future switchable catalyst that can perform controlled copolymerization of different monomers with controlled polymer sequence.

3.2 EFFECTS OF PHOTO-SWITCHABLE LIGANDS ON RU-CATALYZED ROMP AND RCM REACTIONS

3.2.1 Computational methods

The B3LYP[18] density functional and a mixed basis set of SDD[44] for Ru and 6-31G(d) for other atoms were used in geometry optimizations. Single-point energies were calculated with M06[11] and a mixed basis set of SDD for Ru and 6-311+G(d,p) for other atoms. Solvation energy corrections were calculated using the SMD[13] model in benzene ($\varepsilon = 2.27$).[14] In accordance with the experimental conditions, benzene was used as solvent in the calculations for the all reactions. All calculations were performed with Gaussian 09.[15]

3.2.2 Effects of photo-switchable L1 on reactivity of Ru-catalyzed ROMP of cyclooctdiene

Figure 16 presents the computed energy profile of Ru(**L1**)Cl_2 catalyzed ROMP of cyclooctdiene (COD) along the proposed reaction mechanism. The reaction initiates from 4-coordinated ruthenium ethylidene complex **13**. The red line represents reaction with $\mathbf{L1_{open}}$ ligand while the blue line with $\mathbf{L1_{closed}}$ ligand. COD coordination then takes place to form the Dewar–Chatt–Duncanson adduct **14** followed by bottom [2+2] cycloaddition trigonal bipyramidal **TS5** to generate the ruthenacyclobutane **15**. **15** then undergoes retro [2+2] cycloaddition **TS6** to generate product complex **16**.

In reactions with both catalysts, the retro-[2+2] cycloaddition **TS6** is the rate-determining step and the ruthenaalkylidene **13** is the catalyst resting state. In this reaction, the identity of resting

state is unclear due to the small energy difference between **13** and **14**. For the easiness of future discussion, **13** is chosen to be the resting state of Ru-catalyzed ROMP of COD. The calculated $\Delta G^{\ddagger}$ with $\mathbf{L1_{open}}$ is 1.1 kcal/mol lower in energy than with $\mathbf{L1_{closed}}$. Note that if **14** is the resting state, the computed $\Delta\Delta G^{\ddagger}$ between $\mathbf{TS6_{open}}$ and $TS6_{closed}$ is 0.7 kcal/mol, which does not change the relative trend.

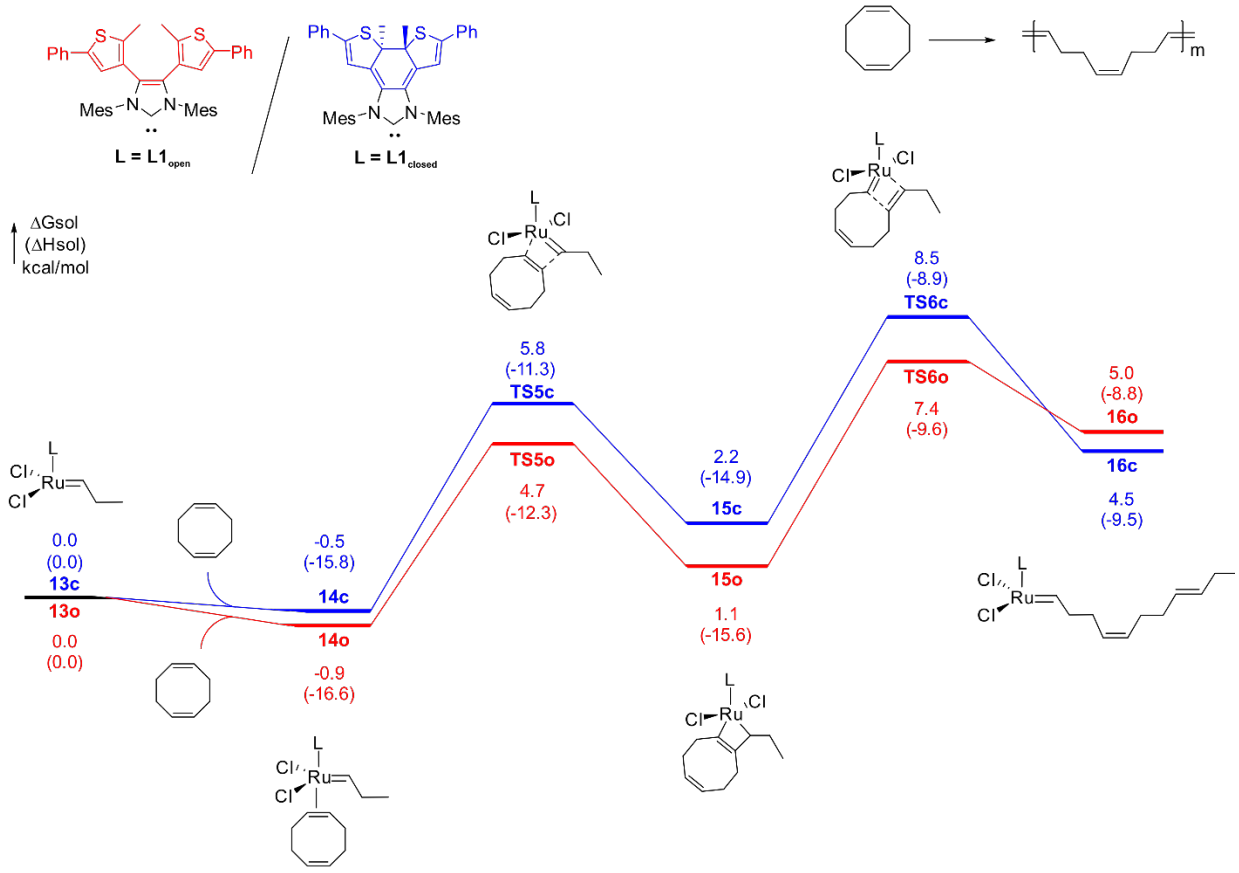

Figure 16. Computed reaction energy profile of the Ru-catalyzed ROMP of cyclooctadiene

The computed $\Delta\Delta G^{\ddagger}$ shows $\mathbf{7_{open}}$ a more efficient catalyst on ROMP of COD, which is in good consistency with the experimentally observed reactivity trend (k_c/k_o = 0.66). The effects of photo-switchable ligands on reaction rate differences were then elucidated by evaluation of the optimized 3-D structure of the rate- determining retro-[2+2] cycloaddition.[45] The computed

activation energies indicate that the ring-opened ligand (**L1$_{open}$**) promotes the barrier required for the retro-[2+2] cycloaddition (7.4kcal/mol) relative to an analogous reaction involving the ring-closed form of the ligand (**L1$_{closed}$**) (8.5kcal/mol). In consistency with experimental kinetic studies, the calculations predicted that the ring-closed catalyst should facilitate the ROMP of COD at a relatively slower rate ($k_{c,theory}/k_{o,theory} = 0.15$), although the rate difference was overestimated when compared to experimental data ($k_c/k_o = 0.66$). In the ROMP of COD, steric interactions with the monomer dominate the difference in reactivity displayed by each form of the catalyst. Upon photocyclization, the NHC backbone undergoes planarization which, in turn, forces the N-mesityl substituents further into the coordination sphere of the ruthenium center. The increased steric bulk in the **L1$_{closed}$** results in an unfavorable steric interaction with the propagating chain, which hinders the retro-[2+2] cycloaddition and thus attenuates the rate of the ROMP.

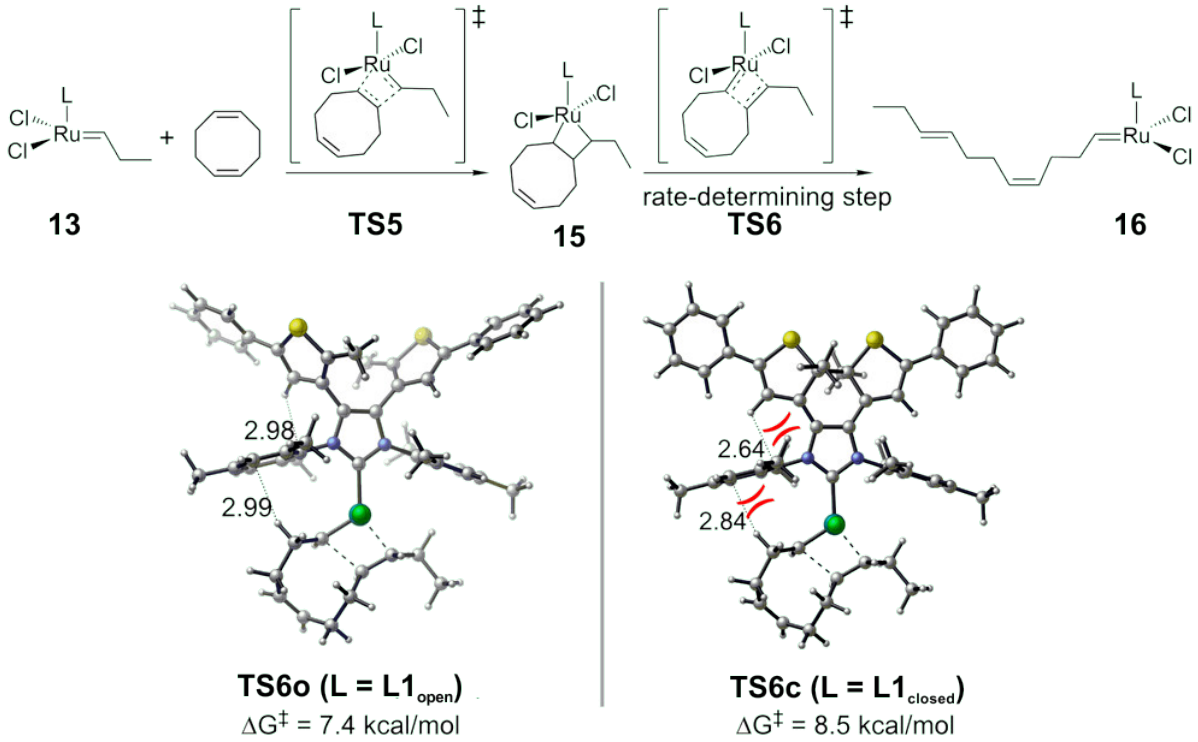

Figure 17. Computed activation Gibbs free energies of ROMP of COD as catalyzed by ruthenium complexed with ring-opened (L1o) or ring-closed (1c) photo-switchable ligands

3.2.3 Effects of photo-switchable ligand L1 on reactivity of Ru-catalyzed ROMP of norbornene

Figure 18 presents the computed reaction energy profile of ROMP of simplified norbornene (NBE) substrate along the proposed reaction mechanism. Ru(**L1**)Cl_2 catalyzed ROMP of NBE initiates from 4-coordinated ruthenium ethylidene resting state **17**. Similar to previous energy profile, the red line represents reaction with $\mathbf{L1_{open}}$ ligand while the blue line with $\mathbf{L1_{closed}}$ ligand. NEB coordination then takes place to form the Dewar–Chatt–Duncanson adduct **18** followed by bottom [2+2] cycloaddition trigonal bipyramidal **TS7** to generate the ruthenacyclobutane **19**. **19** then undergoes retro [2+2] cycloaddition **TS8** to generate product complex **20**.

In reactions with both catalysts, the ruthenaalkylidene **17** serves as catalyst resting state. In consistent with previous computational investigations by Cramer and Hillmyer, the cleavage of ruthenacyclobutane (**TS8**) is promoted by the strained norbornene substrate. Consequently, [2+2] cycloaddition **TS7** that forms ruthenacyclobutane (**TS7**) is the rate-determining step. The computed $\Delta G^{\ddagger}$ of **TS7o** is 2.2 kcal/mol lower in energy than **TS7c**. The computed $\Delta\Delta G^{\ddagger}$ shows $\mathbf{L1_{open}}$ a more efficient catalyst on ROMP of norbornene, which is in good consistency with the experimentally observed reactivity trend ($k_c/k_o = 0.56$).

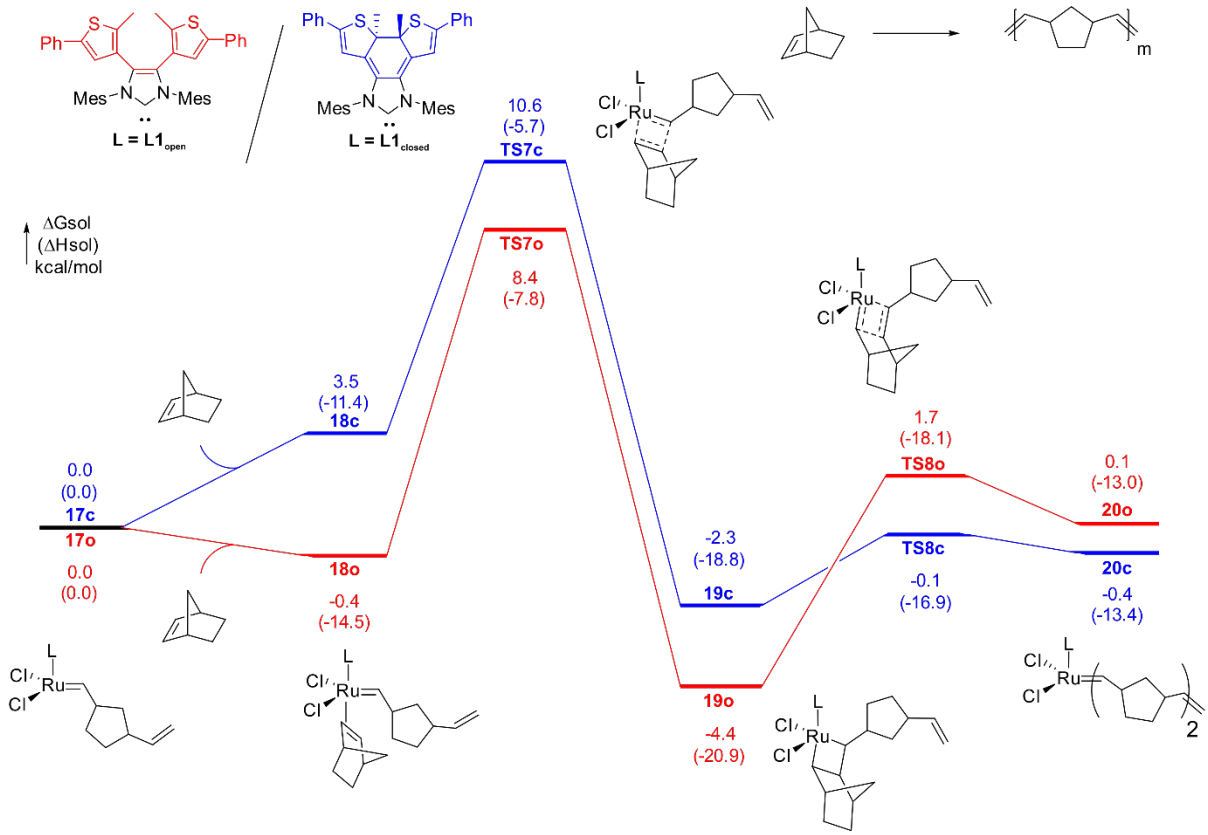

Figure 18. Computed reaction energy profile of Ru-catalyzed ROMP of norbornene

In agreement with the experimental data, DFT calculations indicated that the ring-opened form of the catalyst facilitate the polymerization of the norbornene derivative substrate (8.4kcal/mol) with lower free energy barrier than its ring-closed analogue (10.6 kcal/mol). Closer examination of the optimized **TS7** geometries indicated that steric effects of the ring-opened and ring-closed forms of the NHC ligand are similar during the [2+2]-cycloaddition step with norbornene, which suggested that electronic effects of the photo-switchable ligand dominates the reactivity ROMP of NBE.

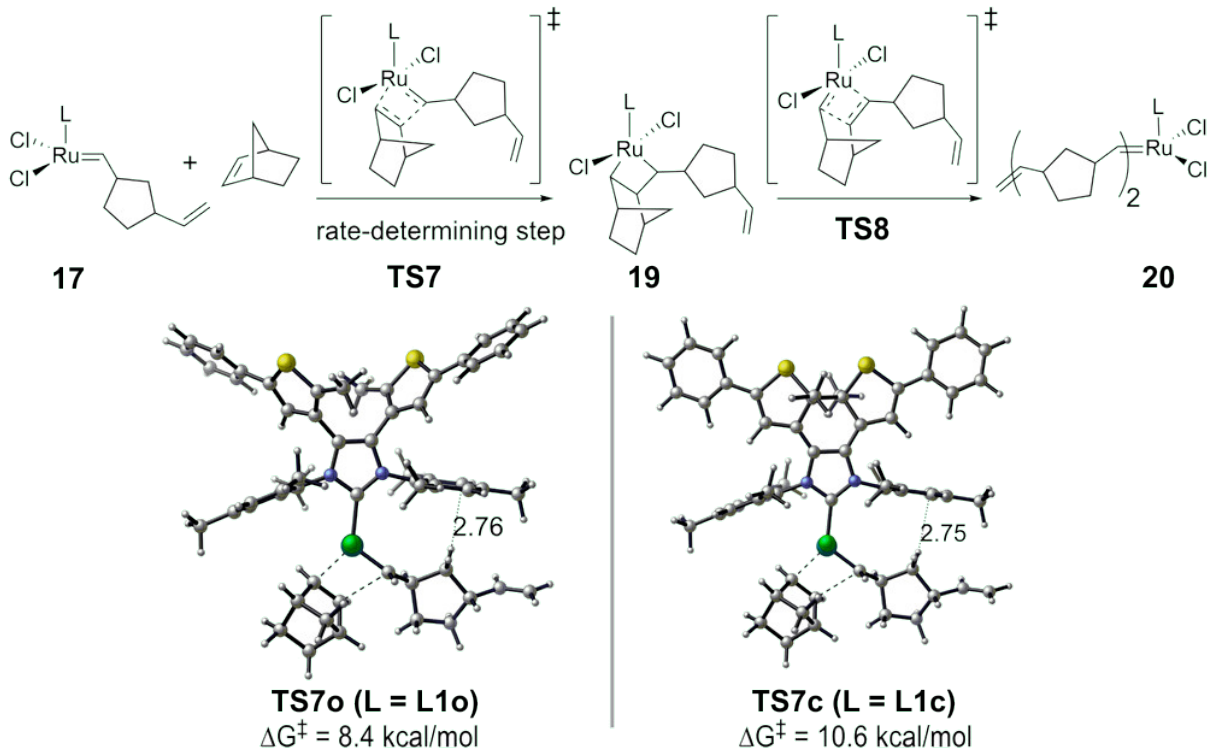

Figure 19. Computed activation Gibbs free energies of ROMP of norbornene as catalyzed by ruthenium complexed with ring-opened ($L1_{open}$) or ring-closed ($L1_{closed}$) photo-switchable ligands

3.2.4 Effects of photo-switchable ligand L1 on reactivity of Ru-catalyzed RCM of 1,6-heptadiene

The reaction energy profile of the complete catalytic cycle of the RCM of 1,6-heptadiene is shown in Figure 20 with the red line represents reaction with $\mathbf{L1_{open}}$ ligand while the blue line with $\mathbf{L1_{closed}}$ ligand. The 1,6-heptadiene substrate binds onto Ru-methylidene catalyst **21** to form the Dewar–Chatt–Duncanson adduct **22**. Subsequent [2+2] – cycloaddition (**TS9**) takes place to form ruthenacyclobutane intermediate **23**, which then undergo retro-[2+2] cycloaddition (**TS10**) to release one molecule of ethylene and alkylidene intermediate **24**. Intermolecular coordination of the terminal double bond forms intermediate **25**, which further undergoes intermolecular [2+2] – cycloaddition (**TS11**) to form the fused ruthenacyclobutane intermediate **26**. The rate-

determining step is the retro-[2+2] cycloaddition (**TS12**) to form the cyclopentene product and the catalyst resting state is the ruthenacyclobutane intermediate **27**. Along the computed reaction energy profile, the fused ruthenacyclobutane intermediate **26** represents the reaction resting state. The activation energy barrier is defined by the barrier difference between **26** and **TS12** for each catalyst.

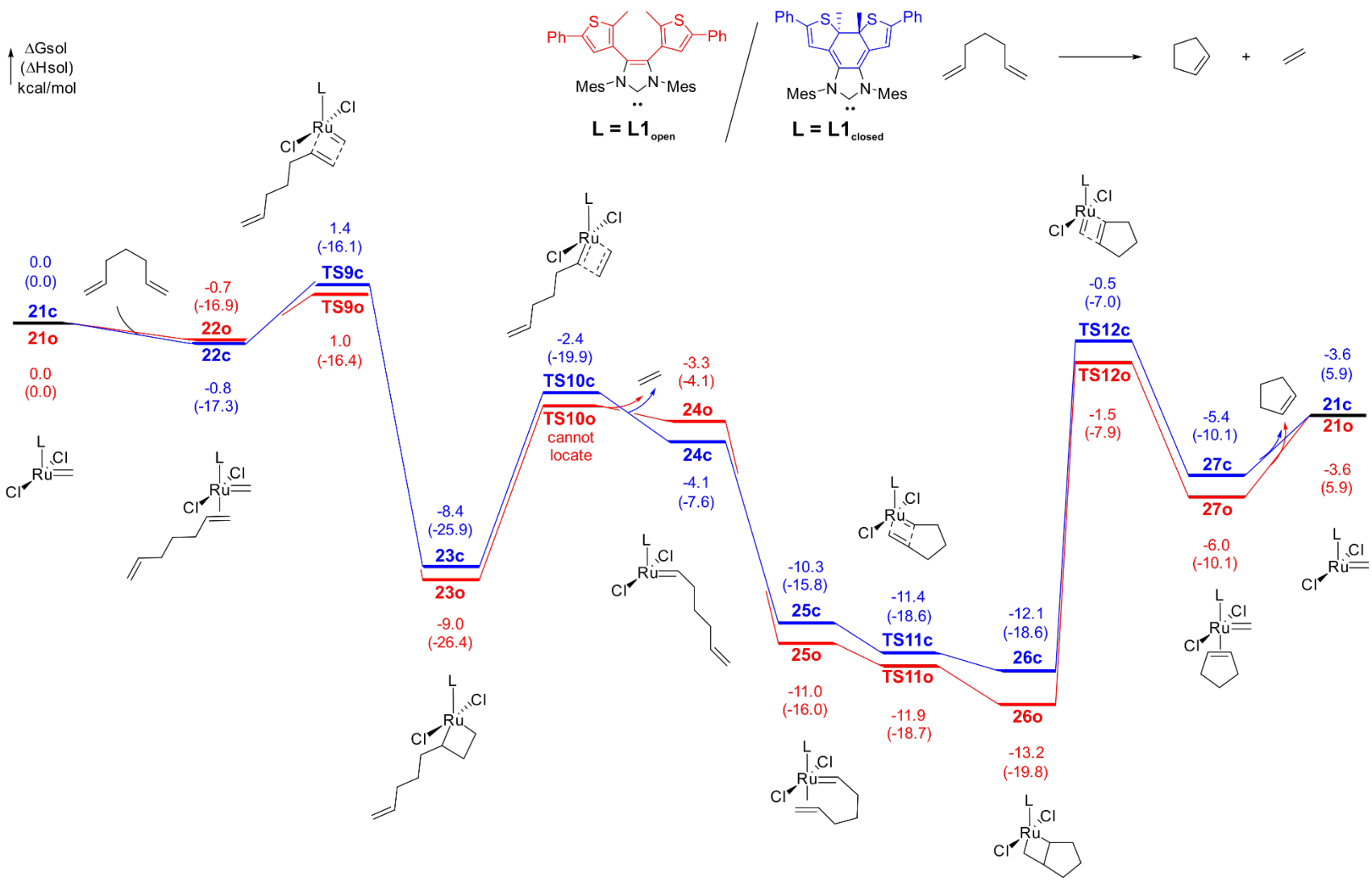

Figure 20. Computed reaction energy profile of the Ru-catalyzed RCM of 1,6-heptadiene

The computed reaction energy profile of Ru-catalyzed RCM model substrate 1,6-heptadiene, revealed that the rate-determining step is the retro-[2+2] cycloaddition (**TS12**) to form the cyclopentene product and that the catalyst resting state is the ruthenacyclobutane intermediate **26**.[46,47]The computed energy barriers indicated that the reaction employing the ring-closed ligand $\mathbf{L1_{closed}}$ required a slightly lower barrier for the retro-[2+2] cycloaddition than the analogous reaction with the ring-opened form ($\mathbf{L1_{open}}$). While the computed activation energies appear to have underestimated the rate constant difference ($k_{c,theory}/k_{o,theory} = 1.2$) compared to that measured by NMR spectroscopy (k_c/k_o = 1.4−1.7), both theory and experiment showed that the RCM reaction was relatively more promoted by the ring-closed ligand $\mathbf{L1_{closed}}$. Since the computed transition state geometries exhibit similar steric interactions between the NHC ligand and the substrate for both forms of the catalyst, the observed rate constant difference was attributed to an electronic effect. In the ring-opened form, the NHC ligand is a stronger donor and stabilizes the Ru(IV) metalacyclobutane intermediate, which results in a higher barrier for the subsequent retro-[2+2] cycloaddition. The $\mathbf{L1_{open}}$ ligand is a better electron donor ligand comparing to $\mathbf{L1_{closed}}$ and promotes the [2+2] - cycloaddition due to stabilization of the ruthenacyclobutane intermediate, and thus results in a faster reaction rate.

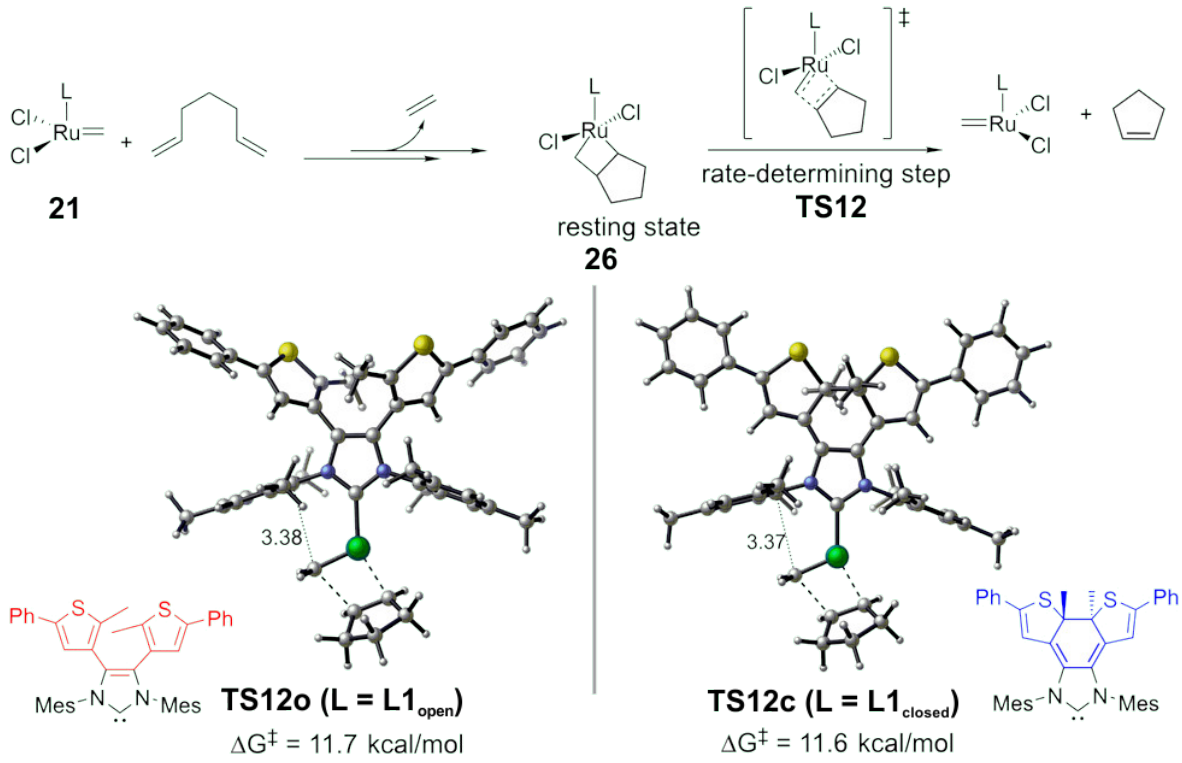

Figure 21. Computed activation Gibbs free energies of the RCM of 1,6-heptadiene norbornene as catalyzed by ruthenium complexed with ring-opened ($L1_{open}$) or ring-closed ($L1_{closed}$) photo-switchable ligands

3.3 EFFECTS OF REDOX-SWITCHABLE LIGANDS ON RU-CATALYZED ROMP AND RCM REACTIONS

3.3.1 Computational methods

The combination of using B3LYP for geometry optimization and M06 for single point energy calculations is the standard method in our recent computational studies of transition metal-catalyzed reactions. We compared the performance of this method with a few other popular methods (as listed in Table 3) for the computational studies of Ru-catalyzed olefin metathesis reactions. The reported Gibbs free energy ($\Delta G^{\ddagger}$) and enthalpy ($\Delta H^{\ddagger}$) are the energies required to

cleave ruthenacyclobutane resting state **(28)** through the rate-determining retro [2+2] cycloaddition (**TS13**). The full energy profile will be presented in 3.3.4.

On top of computational methods, examination on performance of quasiharmonic approximation is also included in Table 3. In column "without quasiharmonic correction", the reported Gibbs free energies and enthalpies include zero-point vibrational energies and thermal corrections at 298 K calculated using a harmonic-oscillator model. In column "with quasiharmonic approximation" the quasiharmonic approximation from Cramer and Truhlar was applied to compute the thermal corrections.[16] In the quasiharmonic approximation, vibrational frequencies lower than 100 cm^{-1} were raised to 100 cm^{-1} as a way to avoid spurious results associated with the harmonic-oscillator model for very low-frequency vibrations.[17] In consistent with previous reported computational studies, the harmonic-oscillator approximation may lead to spurious results for the computed entropies in molecules with low-frequency vibrational modes and lead to inaccurate Gibbs free energy results. As a unimolecular reaction, the computed $\Delta\Delta G^{\ddagger}$ and $\Delta\Delta H^{\ddagger}$ is expected to be relatively close in value. Without quasiharmonic approximation, the $\Delta\Delta G^{\ddagger}$ fluctuation is much higher than that with quasiharmonic approximation. This suggested inclusion of quasiharmonic approximation can significantly improve the entropy calculations in late transition metal catalysis and provide more accurate Gibbs free energy. On the other hand, changing the B3LYP geometry to BP86 with either the SVP basis set or with a mixed basis set with SDD for Ru and SVP for other atoms lead to very small changes in the $\Delta H^{\ddagger}$ and $\Delta G^{\ddagger}$ values computed with the quasiharmonic correction. In summary, the computed $\Delta\Delta H^{\ddagger}$ and $\Delta\Delta G^{\ddagger}$ values are not very sensitive to the choice of density functional and basis set, while the quasiharmonic correction is necessary to achieve consistent results among the methods that are tested.

Table 3. Benchmark of DFT Functional, Basis Set, and Quasiharmonic Correction in Ru-catalyzed RCM Reaction Bearing Redox-switchable NHC Ligands.

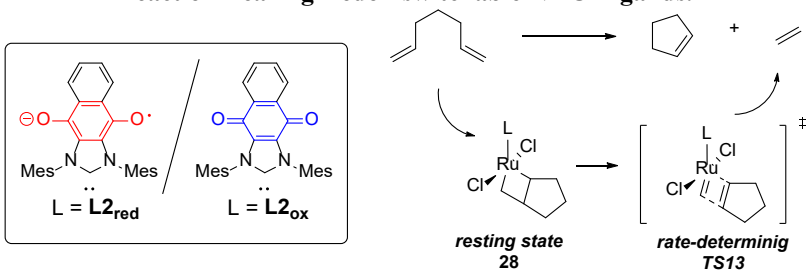

Method	ΔH‡ (**TS13**)	ΔH‡ (**TS13**$_{red}$)	ΔΔH‡	Without quasiharmonic correction ΔG‡ (**TS13**)	Without quasiharmonic correction ΔG‡ (**TS13**$_{red}$)	Without quasiharmonic correction ΔΔG‡	With quasiharmonic correction ΔG‡ (**TS13**)	With quasiharmonic correction ΔG‡ (**TS13**$_{red}$)	With quasiharmonic correction ΔΔG‡
M06/SDD-6-311+G(d,p)/SMD[a] //B3LYP/SDD-6-31G(d)	11.1	11.8	-0.7	10.8	11.2	-0.4	11.0	11.7	-0.7
M06/def2TZVP/SMD[a] //B3LYP/SDD-6-31G(d)	11.8	12.5	-0.7	11.5	11.9	-0.4	11.7	12.4	-0.7
M06/SDD-6-311+G(d,p)/SMD[a] //BP86/SVP	11.1	12.1	-1.0	9.8	12.7	-2.9	10.8	11.9	-1.1
M06/def2TZVP/SMD[a] //BP86/SVP	11.7	12.7	-1.0	10.5	13.3	-2.8	11.4	12.5	-1.1
M06/SDD-6-311+G(d,p)/PCM[a] //BP86/SDD-SVP	10.6	11.6	-1.0	9.8	9.7	0.1	10.2	11.1	-0.9
M06/SDD-6-311+G(d,p)/SMD[a] //M06L/SDD-6-31G(d)/SMD[a]	11.0	11.9	-0.9	12.0	11.3	0.7	11.7	11.7	-0.6

[a] Benzene was used as solvent.

Based on the computational benchmark studies, in this section, B3LYP[18] density functional and a mixed basis set of SDD for Ru and 6-31G(d) for other atoms were used in geometry optimizations. Single-point energies were calculated with M06[11] and a mixed basis set of SDD for Ru and 6-311+G(d,p) for other atoms. Solvation energy corrections were calculated using the SMD[13] model with benzene (ε = 2.27) or CH_2Cl_2 (ε = 8.93)[14] depending the reaction studied. In accordance with the experimental conditions, benzene was used as solvent in the calculations of the RCM of 1,6-heptdiene, while CH_2Cl_2 was used as solvent in calculations of the ROMP of COD and NBE. All calculations were performed with Gaussian 09.[15] To confirm the nature of the

stationary points, vibrational frequency calculations were performed for all optimized structures. All optimized transition state structures have only one imaginary (negative) frequency, and all minima (reactants, products, and intermediates) have no imaginary frequencies. The imaginary frequencies of all transition states and three lowest vibrational frequencies for each optimized structure are provided in the supplementary section below. The Gibbs free energies in solution were calculated at 1 mol/L.

3.3.2 Effects of redox-switchable ligand L2 on reactivity of Ru-catalyzed ROMP of cyclooctadiene

The computed reaction energy profiles for the ROMP of COD is presented in Figure 22. The reaction initiates from 4-coordinated ruthenium ethylidene resting state **29**. The red line represents reaction with the reduced $\mathbf{L1_{red}}$ ligand while the blue line with neutral $\mathbf{L1_{ox}}$ ligand. Cyclooctdiene coordination then takes place to form the Dewar–Chatt–Duncanson adduct **30** followed by trigonal bipyramidal [2+2] cycloaddition **TS14** to generate the ruthenacyclobutane **31**. **31** then undergoes retro [2+2] cycloaddition **TS15** to generate product complex **32**. In reactions with both catalysts, the retro-[2+2] cycloaddition **TS15** is the rate-determining step. The fused ruthenacyclobutane intermediate **31** serves as the catalyst resting state because it is a more stable intermediate than the Dewar–Chatt–Duncanson adduct **30**. The calculated $\Delta G^{\ddagger}$ with $\mathbf{8_{red}}$ is 0.6 kcal/mol lower in energy than with $\mathbf{8_{ox}}$. The change of resting state could be attribute to the electron donor ability of the NHC ligand: the computed smaller TEP suggested both redox-switchable **L2** a generally better donor ligand than both photo-switchable **L1** and could stabilize the electron deficient ruthenacyclobutane intermediates. These computed relative low energy barriers (5.2 and

5.6 kcal/mol with **8ox** and **8red**) are consistent with previous computational studies on the ROMP of COD.

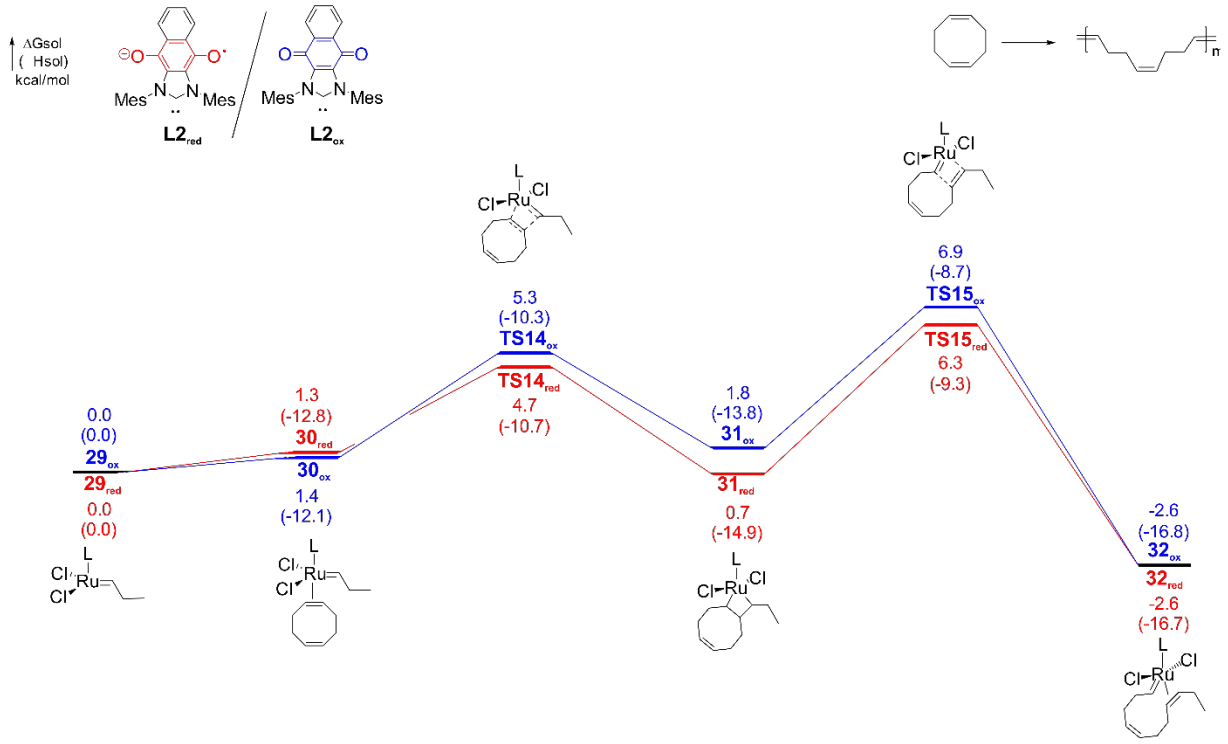

Figure 22. Computed reaction energy profile for the Ru-catalyzed ROMP of cyclooctadiene

The DFT optimized geometry and computed Gibbs free energy of rate-determining retro-[2+2] cycloaddition **TS15** of ROMP of COD is presented in Figure 27. The reduction of **L2ox** does not alter the steric properties of the NHC ligand, evidenced by similar ligand-substrate distances in **TS15ox** and **TS15red**. The reduced ligand suppresses the retro-[2+2] cycloaddition by stabilization of the resting state and results in a slower polymerization ($\Delta G^{\ddagger}_{red}$ = 5.6 kcalmol^{-1} vs. $\Delta G^{\ddagger}_{ox}$=5.2 kcal/mol, $k_1/k_{1red,calc}$=2.6). Although underestimated, the calculated activation energies were in agreement with the relative polymerization rate constants determined by experiment.

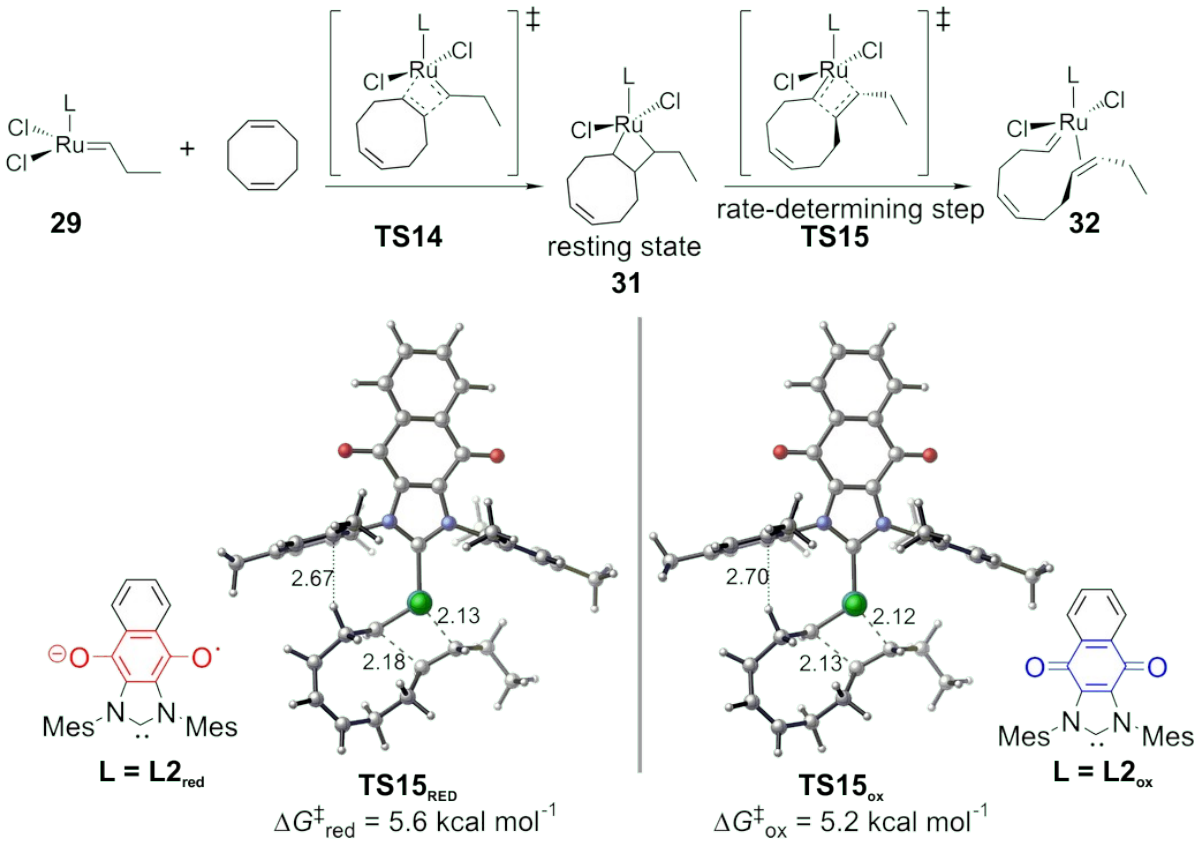

Figure 23. DFT calculations of ligand effects on the activation energies of the rate−determining transition state (TS16) in the Ru-catalyzed ROMP of cyclooctadiene

3.3.3 Effects of redox-switchable ligand L2 on reactivity of Ru-catalyzed ROMP of norbornene

The computed reaction energy profiles for the ROMP of norbornene (NBE) is presented in Figure 24. The reaction initiates from 4-coordinated ruthenium ethylidene resting state **33**. The red line represents reaction with the reduced **L2$_{red}$** ligand while the blue line with neutral **L2$_{ox}$** ligand. NBE coordination then takes place to form the Dewar–Chatt–Duncanson adduct **34** followed by trigonal bipyramidal [2+2] cycloaddition **TS16** to generate the ruthenacyclobutane **35**. **35** then undergoes retro [2+2] cycloaddition **TS17** to generate product complex **36**. In consistent with

previous mechanistic studies, the ring strain of fused ruthenacyclobutane promotes the retro [2+2] cycloaddition. As a result, in reactions with both catalysts, the highest energy [2+2] cycloaddition **TS16** is the rate-determining step. As the lowest energy point on the computed energy profile, the alkylidene intermediate **33** is the catalyst resting state. Although underestimated, the calculated $\Delta\Delta G^{\ddagger}$ trend between $TS19_{ox}$ and $TS19_{red}$ (0.2 kcal/mol) reproduced the experimentally observed larger reactivity with reduced ligand $\mathbf{L2_{red}}$.

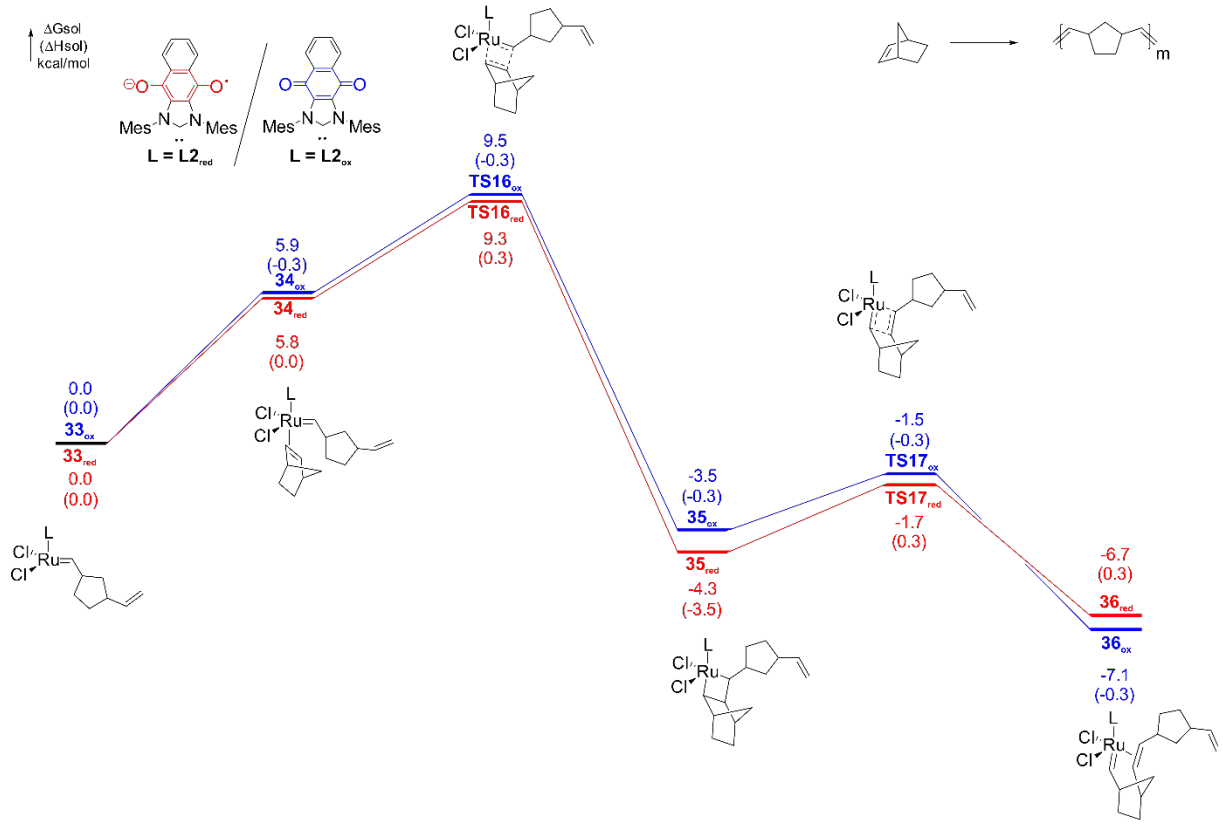

Figure 24. Computed reaction energy profile for the Ru-catalyzed ROMP of norbornene

To ascertain the origins of the experimental observed reactivity trend, the optimized [2+2] cycloaddition transition state geometries are presented in Figure 25. As expected, $\mathbf{L2_{red}}$ and $\mathbf{L2_{ox}}$ exhibit similar steric properties in **TS16** and electronic effects of the ligand dominate the observed

reactivity trend. In its reduced state, the NHC ligand stabilizes the electron-deficient Ru(IV) center and therefore facilitates the polymerization ($\Delta G^{\ddagger}_{red}$= 9.7 kcal/mol vs. $\Delta G^{\ddagger}_{ox}$= 9.9 kcal/mol, k_{1red}/k_1=1.4). Although underestimated, the calculated activation energies were in agreement with the relative polymerization rate constants determined by experiment.

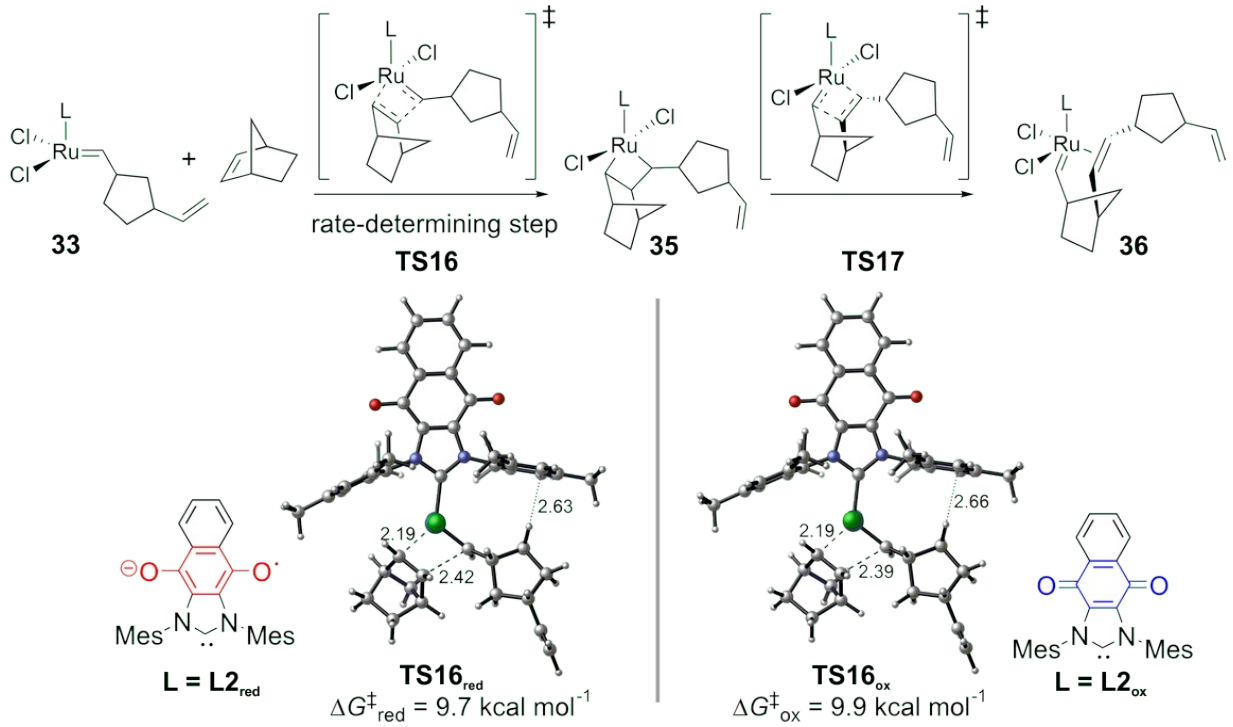

Figure 25. DFT calculations of ligand effects on the activation energies of the rate-determining transition state (TS16) in the Ru-catalyzed ROMP of norbornene

3.3.4 Effects of redox-switchable ligand L2 on reactivity of Ru-catalyzed RCM of 1,6-heptadiene

The reaction energy profile of the complete catalytic cycle of the RCM of 1,6-heptadiene is shown in Figure 26. The red line represents reaction with reduced ligand **L2$_{red}$** while the blue line with neutral ligand **L2$_{ox}$**. The 1,6-heptadiene substrate binds onto Ru-methylidene catalyst **37** to form the Dewar–Chatt–Duncanson adduct **38**. Subsequent [2+2] – cycloaddition (**TS18**) takes

place to form ruthenacyclobutane intermediate **39**, which then undergo retro-[2+2] cycloaddition (**TS19**) to release one molecule of ethylene and alkylidene intermediate **40**. Intermolecular coordination of the terminal double bond forms intermediate **41**, which further undergoes intermolecular [2+2] – cycloaddition (**TS20**) to form the fused ruthenacyclobutane intermediate **28**.

DFT calculations indicate the rate-determining step is the retro-[2+2] cycloaddition to form the cyclopentene product (**TS13**) and the catalyst resting state is the ruthenacyclobutane intermediate **28**. The reaction employing the neutral ligand (**L2$_{ox}$**) requires 0.7 kcal/mol lower barrier for the retro-[2+2] cycloaddition than the reaction with the reduced ligand (**L2$_{red}$**). This is in agreement with the faster reaction rate with the neutral catalyst observed in experiment, although computations underestimated the rate-difference. The experimental rate-constant ratio (100) corresponds to a Gibbs activation energy difference of about 2.7 kcal/mol. The fast reaction rate with the neutral ligand in retro-[2+2] cycloaddition is attributed to an electronic effect. The stronger donor ligand **L2$_{red}$** stabilizes the Ru(IV) metallacyclobutane intermediate (**28$_{red}$**), and thus requires higher barrier for the subsequent retro-[2+2] cycloaddition.

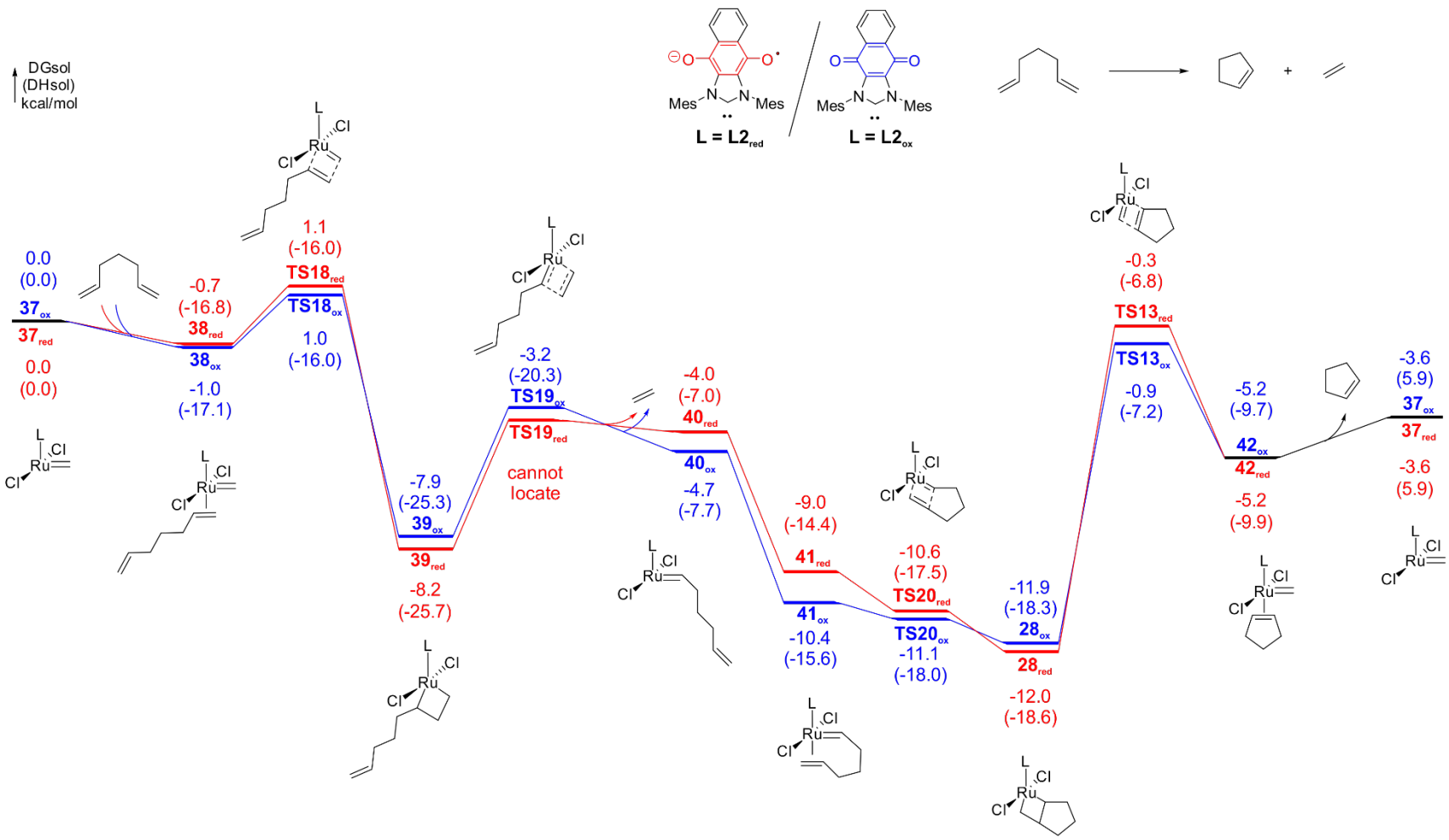

Figure 26. Computed reaction energy profile of the Ru-catalyzed RCM of 1,6-heptadiene

The DFT optimized geometries of retro-[2+2] cycloaddition transition state (**TS16**) is presented in Figure 27. Similar to Ru-catalyzed ROMP of COD and norbornene, the steric properties of the ligand **L2$_{ox}$** does not change significantly upon reduction of the ligand, evidenced by similar ligand-substrate distances in **TS13$_{ox}$** and **TS13$_{red}$**. The more strongly donating reduced form of the NHC ligand electronically stabilized the ruthenacyclobutane transition state, which suppressed the retro-[2+2] cycloaddition and decreased the rate of the reaction ($\Delta G^{\ddagger}_{red}$ = 11.7 kcal/mol vs $\Delta G^{\ddagger}_{ox}$ = 11.0 kcal/mol). Although the calculated rate constant difference for **8$_{ox}$** and **8$_{red}$** mediated RCM of **9** ($k_{2,theory}/k_{2red,theory}$ = 3.3) was significantly lower than the rate differences observed for the RCM reactions of **9** (k_2/k_{2red} = 6.7), the theoretical and experimental data showed that the RCM reactions were promoted by the Ru(II) complex bearing the neutral NHC ligand and was effectively attenuated upon reduction.

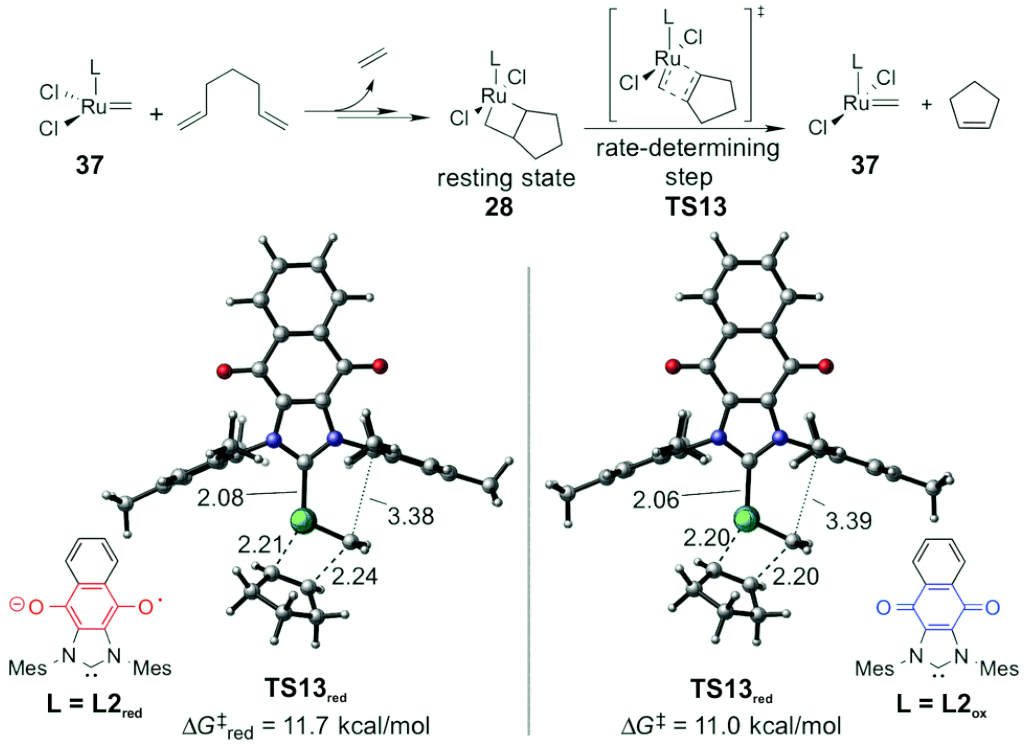

Figure 27. DFT optimized RDS retro-[2 + 2] cycloaddition (TS13) transition states in Ru-catalyzed RCM of 1,6 heptadiene

3.4 SUMMARY

In summary, in collaboration with the Bielawski group, we have investigated the effects of photo- and redox-switchable NHC ligands on the reactivity of Ru-catalyzed ROMP and RCM reactions. In photo-modulated system, the open form ligand **L1$_{open}$** is a better donor and a sterically less demanding ligand when coordinated onto Ru-catalyst as compared to the closed form ligand **L1$_{closed}$**. In redox-modulated system, the reduced ligand **L2$_{red}$** is a better donor ligand comparing to the neutral ligand **L2$_{ox}$**. The steric properties of the redox-switchable NHC ligand remain intact during the switching process.

In consistent with previous mechanistic studies, our DFT calculations also indicated that the rate-determining transition states and resting states are substrate dependent., To be specific, the reaction mechanisms of ROMP reactions are substrate dependent, and consequently electronic and steric effects of the switchable NHC ligands may promote or suppress the ROMP reactivity depending on the substrate. The RDS of ROMP of NBE is formation of ruthenacyclobutane intermediate, namely [2+2]-cycloaddition, which is not a sterically demanding transition state. As a result, electronic properties of the ligand control the observed reactivity. Reactivity of ROMP of NBE is always promoted by better electron donor ligand **L1$_{open}$** and **L2$_{red}$**. The RDS of ROMP of COD is the cleavage of ruthenacyclobutane resting state, namely retro-[2+2]-cycloaddition, which is more sensitive to ligand steric environment. As a result, in photo-modulated system, sterically more demanding ligand **L1$_{closed}$** suppresses the reactivity due to ligand-substrate steric repulsion. In redox-modulated system where ligand steric properties remain intact, better donor ligand **L2$_{red}$** suppresses the reactivity by stabilization of ruthenacyclobutane resting state. The effects of ligands on reactivity trend in RCM of 1,6-heptadie are also elucidated. Both better donor ligands **L1$_{open}$**

and **L2$_{red}$** suppress the RCM of 1,6-heptadiene by stabilization of the metallacycle resting state. The results described in this chapter have established a new strategy to control Ru-catalyzed ROMP and RCM reactions that involve multiple monomers and may facilitate access to new classes of precisely defined copolymers. Indeed, the proof of concept synthesis of cyclooctadiene-norbornene copolymerization has been successfully conducted by our collaborator Bielawski group.

CHAPTER 4. EFFECTS OF N-HETEROCYCLIC CARBENE LIGANDS ON REACTION MECHANISM, REACTIVITY AND REGIOSELECTIVITY OF RH-CATALYZED HYDROBORATION OF STYRENE

A significant part of this chapter was submitted for publication as Shao, H.; Bielawski, C. W.; Liu, P. "Computational Investigation on Effects of *N*-heterocyclic Carbene Ligands on Reaction Mechanism, Reactivity and Regioselectivity of Rh-Catalyzed Hydroboration of Styrene". In this work, I designed and carried out DFT calculations and analysis of computational results.

4.1 INTRODUCTION

N-heterocyclic carbenes (NHCs) are a class of spectator ligands widely applied in homogenous transition metal catalysis due to the tunability of their electronic and steric properties.[48] Although the electronic donor ability of NHC ligands have been investigated, mechanistic insights on the effects of NHC ligands on the mechanism, reactivity, and selectivity in Rh catalyzed hydroboration reactions remain unstudied.[49] With its unique molecular scaffold, modification of NHC backbone and the *N*-substituents could offers novel modes of reactivity and selectivity control in switchable catalysis, in which the structure of the NHC ligand is altered on-the-fly through external stimulus.[35,36,37,38] In 2009, Bielawski group has incorporated a photochromic diarylethene (DAE) into the backbone of an NHC ligand to facilitate the photomodulation of electronic property of the ligand. As illustrated in Scheme 1a, **L1** undergoes reversible photocyclization: UV light promotes the 1,2-dithiophenylethylene cycloaddition to form

the cyclohexadiene derivative **L1c**. Under visible light, 6π-electrocyclic ring opening occurs to form dithiophenyl ethylene form (**L1o**). As reported by Bielawski group, the Rh-L1 catalyst exhibited capability to modulate the reactivity of Rh-catalyzed olefin hydroboration with photo-modulation. Hydroboration of styrene is 9.2 times faster under visible light with **L1o** than that under UV light with **L1c**.[50 51] (Scheme 1b) As presented in Chapter 3, the same class of photo-switchable NHC ligands have been successfully applied to control the reactivity of Ru-catalyzed ROMP and RCM reactions. Our computational analysis suggested that both electronic and steric properties of the photo-switchable NHC ligand are altered upon photo-cyclization and affect the catalyst activity in Ru-catalyzed ROMP and RCM reactions. Therefore, both electronic and steric effects may contribute to the reactivity difference of this photo-switchable catalyst system in the Rh-catalyzed hydroboration reactions.

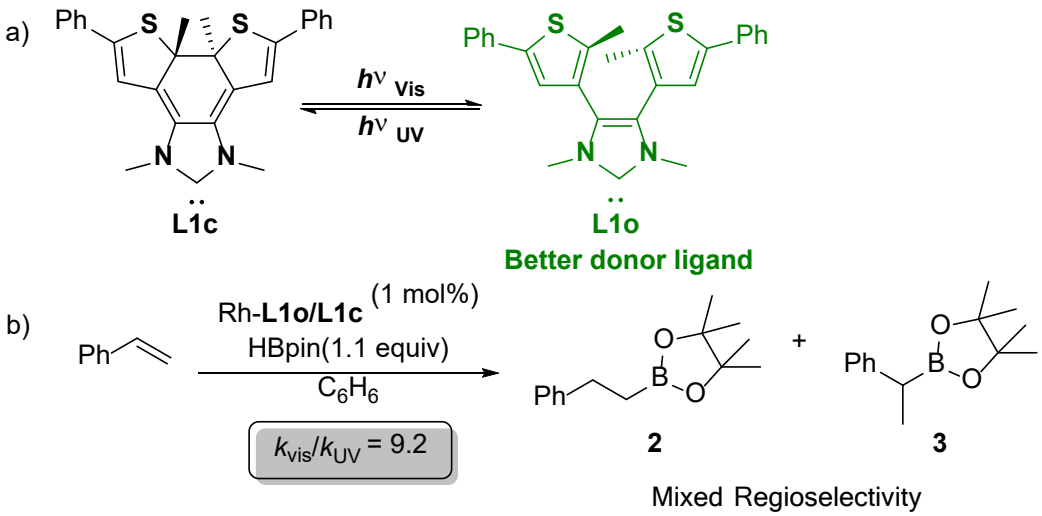

Figure 28. (a). Rh(I) precatalyst with photo-switchable NHC ligands (L1o and L1c); (b). Rh(L1)Cl-catalyzed hydroboration of styrene with distinct reactivity

To computationally evaluate the electronic and steric effects of photo-switchable NHC ligands on reactivity and selectivity, one needs to elucidate the reaction mechanism of Rh-NHC catalyzed hydroboration of styrene. Although the proposed reaction mechanism with 4 competing

pathways leading to two regioisomeric hydroboration products is well accepted, the identity of favored reaction pathway and rate-determining step remain unclear.[52] The detailed proposed mechanism is presented in Figure 29, in which the left two pathways lead to the linear product (**i**) and the right two pathways lead to the branched product (**ii**). All four pathways initiate via ligand exchange of the Rh(I) pre-catalyst **3** to form the reactant complex **4** with agnostic H–Bpin coordination. Oxidative addition of hydrogen-boron bond then takes place to generate the 5-coordinated Rh(III) complex **5**. Subsequent migratory insertion of the olefin may occur via four competing pathways involving either insertion into the Rh-B or the Rh-H bond with two regioisomeric approaches of the olefin. Olefin insertion into the Rh-H bond (*i.e.* hydride migration) forms **7L** and **7B**, which then undergo C-B reductive elimination to release the linear and branched products i and ii, respectively. This hydride migration mechanism is referred to as the Männig-Nöth mechanism, originally proposed by Männig and Nöth in 1985.[52] Alternatively, in the modified Männig-Nöth mechanism, or boryl migration mechanism, olefin inserts into the Rh-B bond to form **6L** and **6B**, which generate corresponding linear and branched products through C-H reductive elimination.

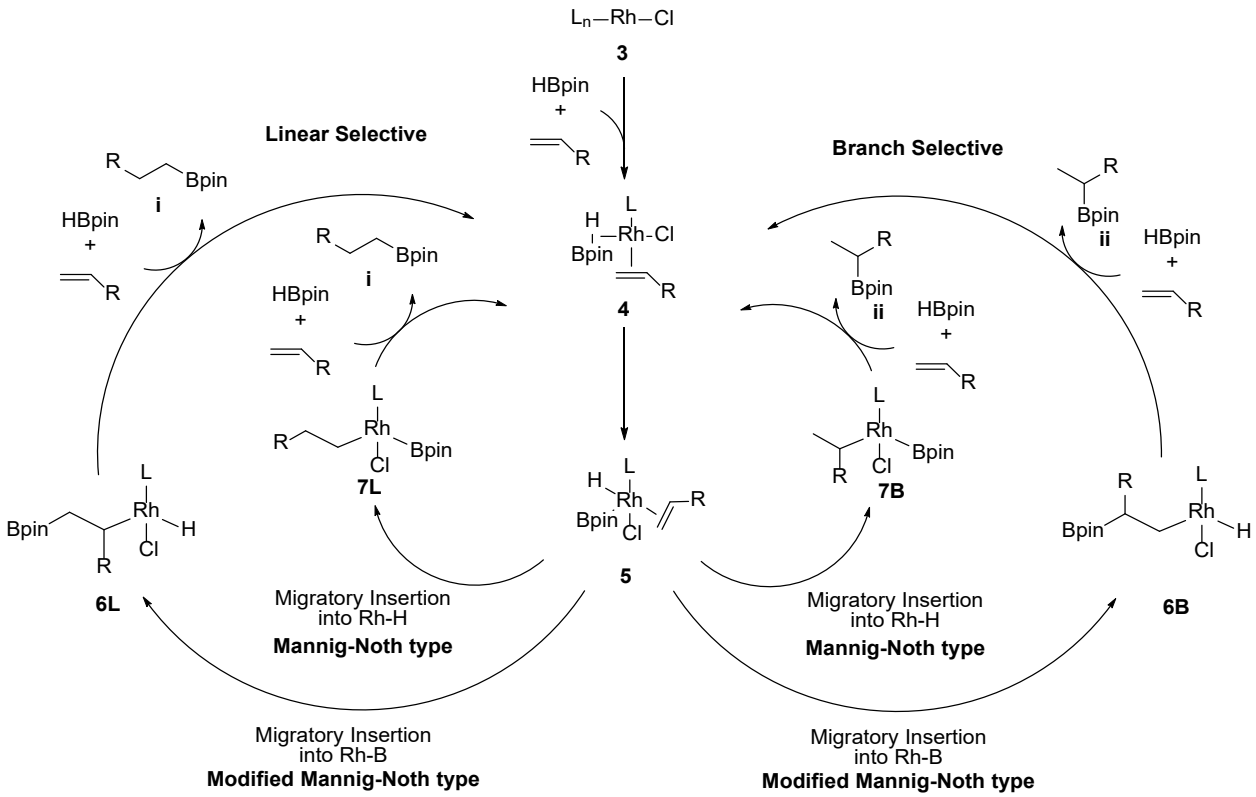

Figure 29. Proposed mechanism of Rh-catalyzed olefin hydroboration reactions

The reaction mechanism of olefin hydroboration utilizing Rh(I) catalyst and phosphine ligands has been probed both experimentally and computationally through the past few decades. Deuterium labeling studies by Evans and Fu in early 1990s concluded that $Rh(PPh_3)_3Cl$ catalyzed hydroboration of styrene proceed via hydride migration followed by rate-determining C-B reductive elimination step. Interestingly, computational mechanistic investigation on reaction mechanism of $Rh(PH_3)_3Cl$ catalyzed hydroboration of ethylene suggested both the Männig-Nöth mechanism through hydride migration and modified Männig-Nöth mechanism through boryl migration pathways are possible.[53-54] (Figure 30) In 1994, computational studies by the Morokuma group suggested boryl migration the favored pathway along the associative mechanism with two PH_3 coordinated in rate-determining boryl migration transition state.[55] A later mechanistic investigation by the Zieglar group in 2000 concluded that hydride migration is significantly

favored over boryl migration along the dissociative mechanism, with C-B reductive elimination as rate determining transition state.[56] The ambiguity in previous computational mechanistic studies suggested the reaction mechanism of Rh-catalyzed hydroboration reactions may change depending on the steric environment created by the ancillary ligands. Moreover, no computational mechanistic studies have been presented to investigate the origin of regioselectivity in Rh-catalyzed hydroboration of styrene.

To resolve the aforementioned mechanistic challenges, this chapter will investigate the reaction mechanisms of $Rh(PPh_3)_3Cl$ and Rh(NHC)Cl catalyzed hydroboration of styrene by elucidating the favored reaction pathways and identifying rate-determining transition state. The difference between NHC and PPh_3 ligands and their effects on reaction mechanism will then be discussed. The effects of photo-switchable ligand on reactivity and regioselectivity of hydroboration of styrene will also be presented to study the structural-function relationship between electronic and steric properties of the NHC ligand and hydroboration reactivity and regioselectivity.

a) Previous computational studies - Morokuma (**1994**)

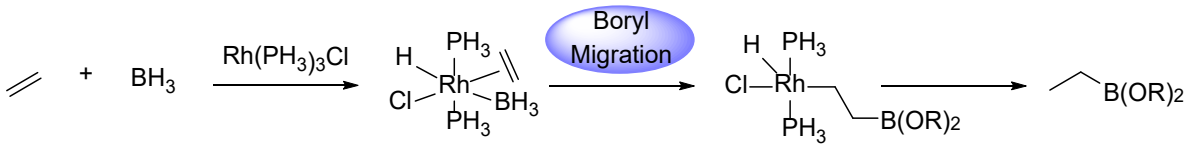

b) Previous computational studies - Ziegler (**2000**)

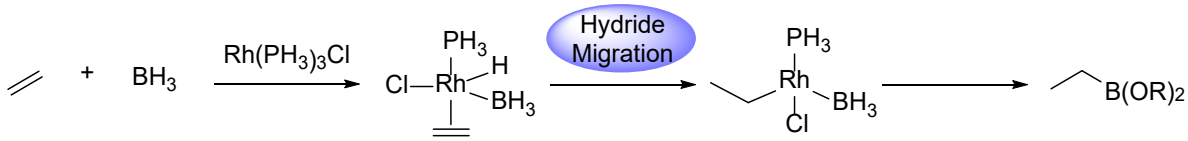

c) Goals of present computational studies:

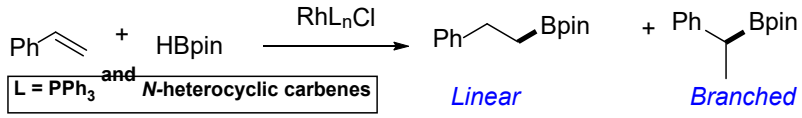

- To identify rate- and regioselectivity- determining step in Rh-catalyzed hydroboration of styrene and the effects of NHC ligand on reaction mechanism
- To study electronic and effects of photoswitchable NHC ligands on observed reactivity and regioselectivity

Figure 30. Proposed mechanism of early computational mechanistic studies on Rh-catalyzed hydroboration with simplified ethylene substrate

4.2 COMPUTATIONAL DETAILS

All geometry optimizations were performed using the B3LYP functional[18] with a mixed basis set of SDD for Rh and 6-31G(d) for other atoms.[44] Single point energies were calculated with M06[11] and a mixed basis set of SDD for Rh and 6-311+G(d,p) for other atoms. Solvation effects were considered by performing single point calculations with the SMD[13] model in benzene (ε = 2.27).[14] All calculations were performed with Gaussian 09.[15]

Reaction energy profiles presented in this study were obtained by optimizing molecular geometries and calculating energies of the reaction intermediates (local minima) and transition states (1st order saddle point) along plausible reaction pathways. Vibrational frequencies were computed at the same level of theory in geometry optimization to confirm whether the structures

are intermediates (no imaginary frequency) or transition states (only one imaginary frequency). Reported Gibbs free energies and enthalpies include thermal corrections computed at 298K.

The reported Gibbs free energies and enthalpies include zero-point vibrational energies and thermal corrections at 298 K calculated using a harmonic-oscillator model. Since the harmonic-oscillator approximation may lead to spurious results for the computed entropies in molecules with low-frequency vibrational modes, the quasiharmonic approximation from Cramer and Truhlar was applied to compute the thermal corrections for a few key transition state structures.[16] In the quasiharmonic approximation, vibrational frequencies lower than 100 cm^{-1} were raised to 100 cm^{-1} as a way to avoid spurious results associated with the harmonic-oscillator model for very low-frequency vibrations.[17] The reported energies in the text were corrected using the quasiharmonic approximation. The Gibbs free energies in solution were calculated at 1 mol/L.

4.3 RESULTS AND DISCUSSION

4.3.1 Reaction mechanisms of Rh-IMe catalyzed hydroboration of styrene

We first investigated the reaction mechanism of Rh-NHC catalyzed hydroboration of pinacolborane (HBpin) and styrene using the 1,3-dimethylimidazol-2-ylidene (IMe) ligand. The computed reaction energy profiles for the four competing pathways are presented in Figure 31. From the reactant complex **4**, B-H oxidative addition takes place via 3-centered transition state **TS1** to form 5-coordinated Rh(III) complex **5**. As discussed earlier, four competing styrene migratory insertion pathways lead to two regioisomeric hydroboration products. The black

pathways represent the hydride migration mechanism, and the red pathways account for the boryl migration mechanism, where styrene inserts into the Rh-B bond. The 2,1-hydride migration (**TS2**), where the hydride migrates onto the terminal carbon of the styrene, and the 1,2-boryl migration (**TS5**), where the Bpin group migrates onto the internal carbon, lead to the branched product **3**. The 2,1-boryl migration (**TS3**) and the 1,2-hydride migration (**TS4**) produce the linear regioisomer **2**. The 2,1-boryl and hydride migrations (**TS3** and **TS2**) to form benzylic rhodium complexes **6** and **7** are favored over corresponding 1,2-migration pathways (**TS4** and **TS5**) due to electronic stabilization of the α-Ph substituent that delocalizes the partial negative charge on the α carbon.[57] Subsequently, the benzylic Rh(III) intermediates **6** and **7** undergo facile C-H and C-B reductive elimination via **TS6** and **TS7** to form the linear and branched products (**2** and **3**), respectively. The reactant complex **4** is regenerated upon the coordination of another molecule of HBpin and styrene. The rate- and regioselectivity determining step (RDS) of the overall hydroboration cycle is the 2,1-migratory insertion of styrene into the Rh-B/Rh-H bond, **TS2** and **TS3** for branched and linear products, correspondingly.

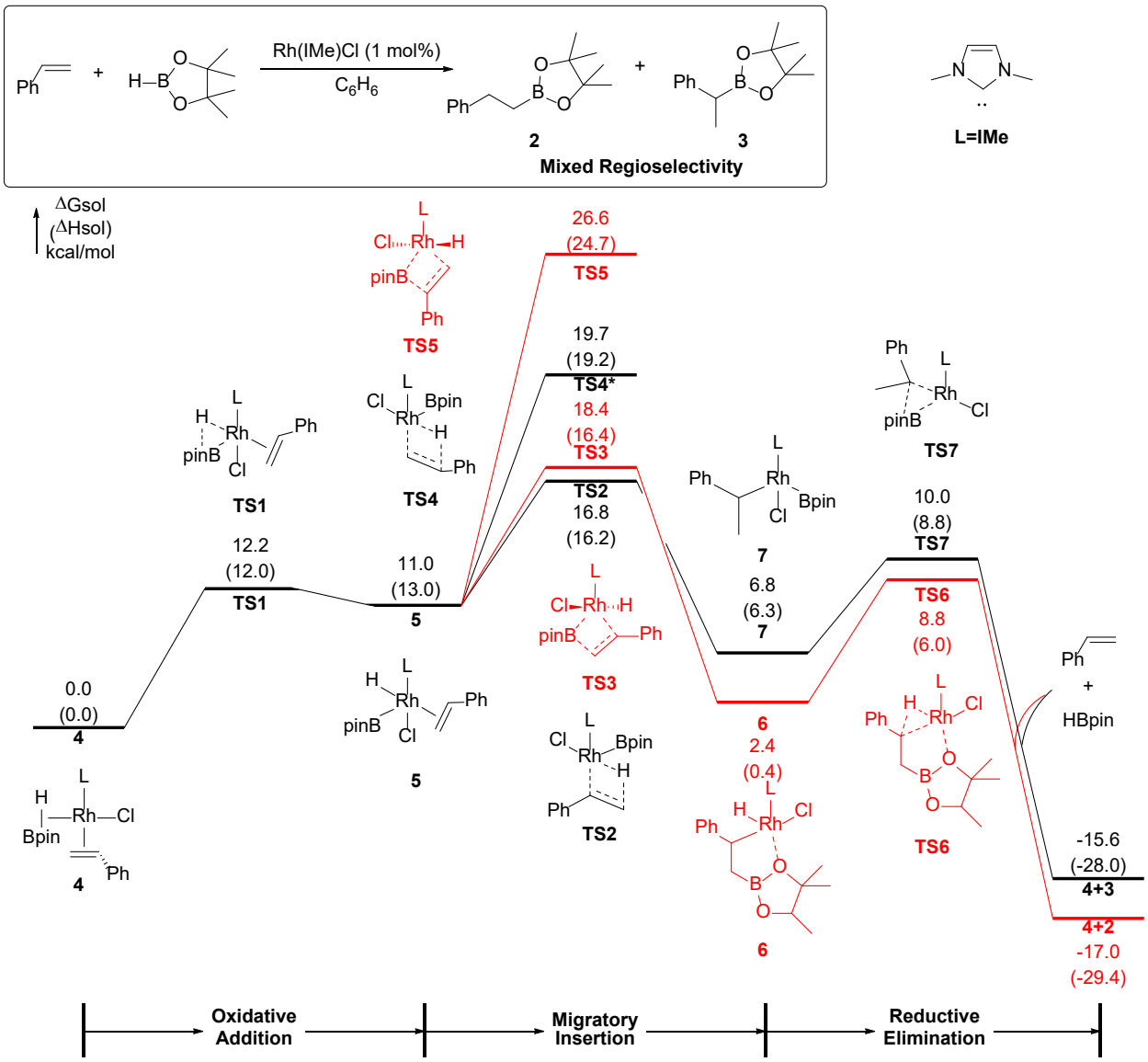

Figure 31. Calculated energy profile for Rh(IMe)Cl catalyzed hydroboration of styrene
(All energies are with respect to the four-coordinate square planar reactant complex 1.)
(*Geometry optimization of TS4 is conducted at B3LYP/LANL2DZ−6-31G(d) level of theory with energy computed at M06/SDD−6-311+G(d,p)/SMD (benzene) level of theory)

The optimized geometries of the two most favorable migratory insertion transition states (**TS2** and **TS3**) are presented in Figure 32. Interestingly, both hydride and boryl migration transition states could potentially adopt two different geometries, namely square-based pyramidal (*sbp*) and trigonal bipyramidal (*tbp*). Both electronic structure of the 5-coordinated Rh(I) complex

and the steric repulsion between ligands contribute to the relative favorability between *sbp* and *tbp* geometries. Early crystal field theory analysis suggested *sbp* conformation is electronically favored due to lower lying d orbitals with C_{4v} symmetry.[58] Consequently, branch-selective hydride migration transition state favors square-based pyramidal (*sbp*) geometry (**TS2**) over trigonal bipyramidal (*tbp*) geometry (**TS2b**) by 6.3kcal/mol due to favored electronic structure of Rh(III) complex. On the other hand, *tbp* conformation is sterically favored due to strain release of ligand-ligand repulsive interaction, the sterically more demanding linear-selective boryl migration favors *tbp* geometry (**TS3**) over *sbp* geometry (**TS3b**) by 11.0 kcal/mol due to strain release. The different favored geometries of hydride and boryl migration transition states will later contribute to the effects of NHC ligands on reaction mechanism and regioselectivity. The square based pyramidal geometry is more sensitive to ligand steric properties, consequently sterically more hindered ligands are expected to suppress hydride migration transition states and promote branch regioselectivity in Rh-NHC catalyzed hydroboration of styrene reactions.

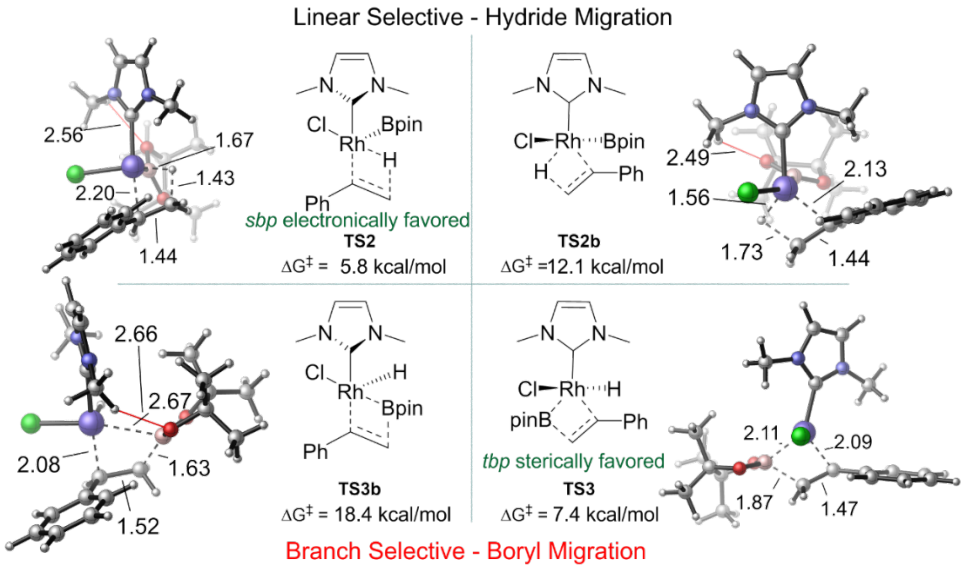

Figure 32. Optimized structures of hydride and boryl migration transition state TS2 and TS3
(All energies are with respect to the four-coordinate square planar reactant complex 1 as in scheme 3.) Geometry optimization of TS3_b is conducted at B3LYP/LANL2DZ−6-31G(d) level of theory with energy computed at M06/SDD−6-311+G(d,p)/SMD (benzene) level of theory

4.3.2 Reaction mechanisms of $Rh(PPh_3)_3Cl$ catalyzed hydroboration of styrene

This section investigates the reaction mechanism on hydroboration of styrene with Wilkinson's catalyst ($Rh(PPh_3)_3Cl$). Figure 33 presents the computed energy profile containing four competing pathways. From 3-coordinated complex **5**, B-H oxidative addition takes place through an associative mechanism to form stable intermediate **6**. Though no oxidative addition transition state is located, this step can be considered energetically facile.[55] Ligand substitution leads to the 5-coordinated Rh(III) intermediate **7**. Similar to last section, subsequent dissociative migratory insertion of styrene occurs via four competing pathways. Due to the steric bulkiness of Bpin ligand, attempts to identify associative 6-coordinated octahedral migratory insertion transition states always fail with the dissociation of one PPh_3 ligand. Both hydride migration transition states (**TS8** and **TS9**) are energetically favored over the boryl migrations (**TS10** and **TS11**).[55] Upon coordination of one PPh_3 ligand, Rh(III) intermediates **8** and **9** then undergo associative C-B reductive elimination via **TS14** and **TS15** to release the linear and branched products respectively.

The reaction energy profile designates the RDS as hydride migration, **TS8** and **TS9**. Interestingly, as reported by Evans, Fu and Calabrese, the regioselectivity of $Rh(PPh_3)_3Cl$ catalyzed hydroboration of styrene is dependent on PPh_3 concentration. With fresh prepared catalyst or by adding excess PPh_3 ligand into the reaction mixture, up to 99% branched selectivity is reported, which agrees with the computationally predicted regioselectivity.[53,59] On the other hand, the oxidation of catalyst can lead to mixed regioselectivity[60], we hypothesized that oxidation

of catalyst could cause dissociation of one PPh_3 ligand from the Rh(III) complex and lead to dissociative reductive elimination transition states. Indeed, the computed dissociative reductive elimination step raises in energy (10.5 kcal/mol) along the branched selective pathway. The computed small ΔΔG (0.1kcal/mol) between rate-determining-step along linear (**TS9**) and branched (**TS15_dissociative**) is in consistent with expected mixed regioselectivity.

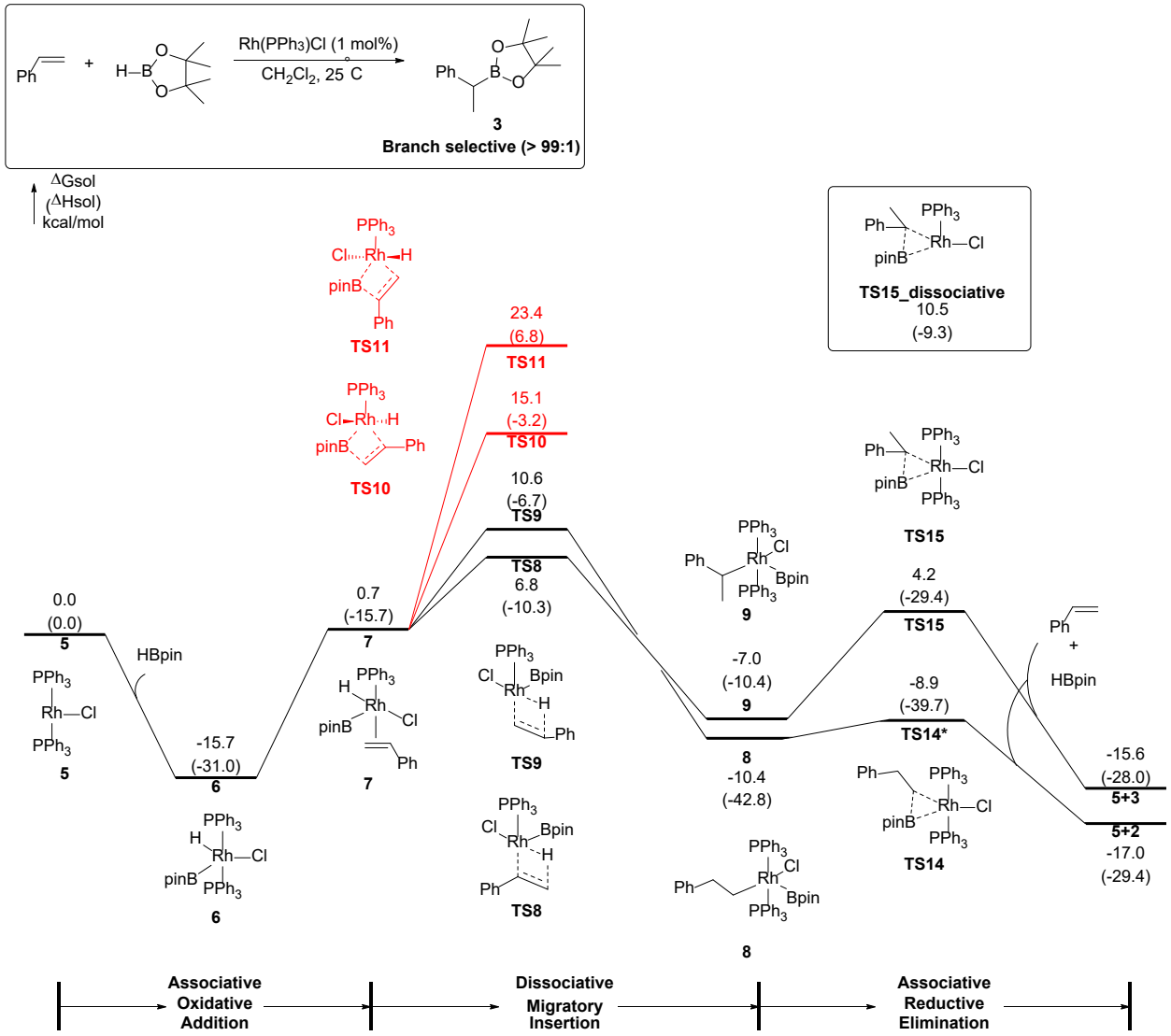

Figure 33. Calculated energy profile for Rh(PPh3)3Cl catalyzed hydroboration of styrene
(All energies are with respect to the four-coordinate square planar reactant complex 5.)
(*Geometry optimization of TS14 is conducted at B3LYP/LANL2DZ−6-31G(d) level of theory with energy computed at M06/SDD−6-311+G(d,p)/SMD (benzene) level of theory)

As the computed reaction mechanism suggested, the Rh-NHC and Rh-PPh_3 catalyzed hydroboration of styrene proceed via different reaction mechanisms. Branched selective styrene hydroboration always proceed via *sbp* 2,1 hydride migration transition states, (**TS2** and **TS8)**. However, linear selective hydroboration of styrene undergoes different reaction pathways as illustrated in Figure 34. With PPh_3 ligand, 1,2 hydride migration **TS9** is 4.5 kcal/mol favored over 2,1 boryl migration **TS10**. With sterically more demanding IMe ligand, evidenced by cone angle, **TS4** is disfavored by 1.3 kcal/mol comparing to **TS3**. The relative bulkier IMe ligand exhibit unfavorable steric clash between IMe *N*-Me substituents and *cis* chloride and Bpin ligands create a sterically demanding environment. This steric environment is created by the inherent electronic and steric difference between PPh_3 and IMe ligands. Firstly, with two *N*-Me substituents point toward the substrate plane, IMe is a bulkier ligand evident by its measured cone angle. Secondly, Rh-C distance in **TS4** is significantly smaller than Rh-P distance in **TS9** for IMe is a stronger donor ligand. As a result of disfavored steric environment, **TS4** raises in energy and 2,1 boryl migration **TS3** thus became the RDS for linear selective pathway of Rh(IMe)Cl catalyzed hydroboration of styrene.

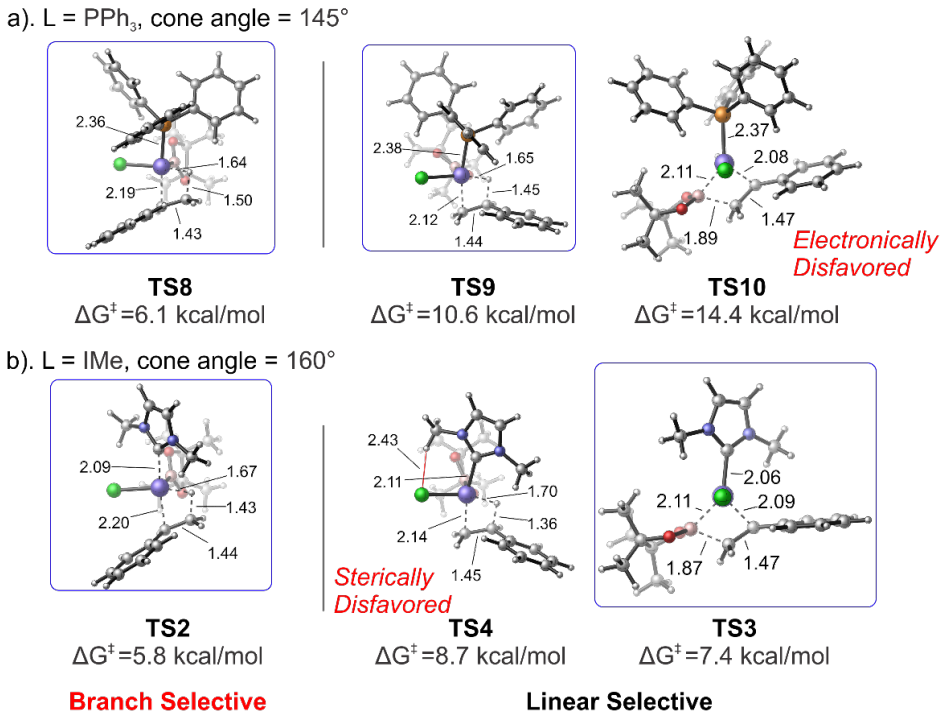

Figure 34. Favored hydride and boryl migration transition states of a). $Rh(PPh_3)_3Cl$ and b). Rh(IMe)Cl catalyzed hydroboration of styrene

(All energies are with respect to the 5-coordinate square based pyramidal intermediates **5** in Figure 31 and **7** in Figure 33)

4.3.3 Effects of photo-switchable NHC ligands on reactivity of Rh-catalyzed hydroboration of styrene

The effects of photo-switchable ligands on rate-determining hydride and boryl migration barriers and consequently the reaction rates of in Rh catalyzed hydroboration of styrene is presented. As previously introduced, experimentally styrene hydroboration with Rh-L1 is 9.2 times faster under visible light with **L1o** than under UV light with **L1c**. Table 4 summarizes the Tolman electronic parameters (TEP) of tested NHC ligands, experimental observed reaction rate, and computed activation energy barriers. The vibrational frequencies are computed with mPW1PW91/6-311$^+$G(2d)-6-311$^+$G(d,p) in the gas phase in $Ni(CO)_3L$ complex. The computed frequencies are scaled with a scaling factor of 0.954. The switchable NHC ligand under visible

light **L1o** has smaller TEP, suggesting it a better electron donor ligand than **L1c** under UV light. The computed TEP values are in good consistence with reported experimental values.[61]

The computed $\Delta G^{\ddagger}$_L is the activation Gibbs free energy of boryl migration, while the computed $\Delta G^{\ddagger}$_B is the activation Gibbs free energy of hydride migration with respect to the corresponding 4-coodinated agostic HBpin Rh-complex. In consistent with experimental observations, both computed $\Delta G^{\ddagger}$ and experimentally measured reaction rate suggest Rh catalyzed hydroboration of styrene proceed faster with **L2** than open form **L1o** ligand than with closed form **L1c** ligand. Electronic property of the photo-switchable ligand is the dominating factor contributes to the observed catalyst activity trend. The Rh center coordination number is reduced from 5 to 4 and is electron deficient during migratory insertion. Thus, a better electron donor ligand stabilizes both hydride and boryl migration and makes the overall reaction kinetically more favorable. Stronger donor ligands **L1o** with smaller TEP clearly promote both boryl and hydride migration.

Interestingly, the computed TEP suggested **L2** a weaker electron donor ligand than **L1o**. Along the linear selective pathway, the computed $\Delta G^{\ddagger}$_L of boryl migration transition state with **L2** follows the observed trend of electronic ligand effect on reactivity. However, along the branched selective pathway, the computed $\Delta G^{\ddagger}$_B of hydride migration transition state with **L2** is lower than that with both ligands. This suggested that on top of ligand electronic effects on reactivity, ligand steric effect cannot be neglected.

Table 4. Electronic Effects of NHC Ligands on Boryl and Hydride Migration Barrier.

	L=L1o	**L=L1c**	**L=L2**
Experimental TEP (cm^{-1})	2049	2055	-
Experimental rate ($mol^{-1}\ s^{-1}$)	2.3×10^{-3}	2.5×10^{-4}	6.0×10^{-2} (vis)
			1.9×10^{-1} (UV)
Calculated TEP (cm^{-1})	2051	2056	2054
$\Delta G^{\ddagger}$_L (kcal/mol)	17.9	19.5	18.4
$\Delta G^{\ddagger}$_B (kcal/mol)	18.0	18.8	16.8

Figure 35 then presents the optimized rate- determining transition states for linear and branched selective hydroboration of styrene with **L2** and photo-switchable NHC ligands **L1o** and **L1c**. Closer examination of computed transition states **TS2o/c** and **TS3o/c** suggests that the steric property of the ligand remain intact during the switching process. The measured *N*-Me and hydride H-H distance is in *sbp* hydride migration **TS2o** and **TS2c (**2.24 Å and 2.22 Å) suggested the existence of ligand-substrate steric clash with both ligands due to backbone repulsion. No unfavorable steric clash in both *tbp* boryl migration **TS3o/c** transition states.

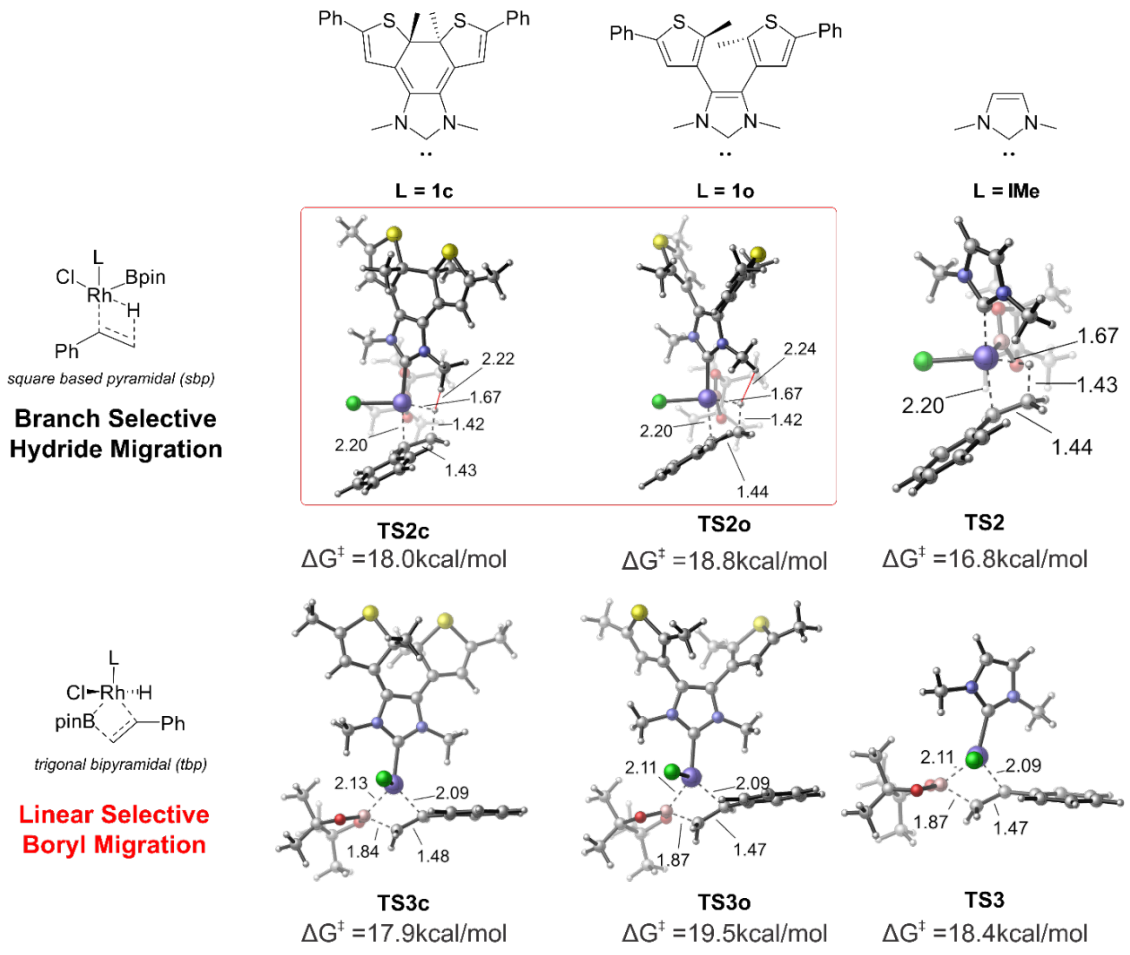

Figure 35. Effects of photo-switchable ligands on reactivity of hydroboration of styrene
(All energies are with respect to its corresponding four-coordinate square planar reactant complex x, Vibrational frequencies computed with mPW1PW91/6-311+G(2d)-6-311+G(d,p) in the gas phase in $Ni(CO)_3L$; computed frequencies are scaled with a scaling factor of 0.954)

4.3.4 Effects of photo-switchable NHC ligands on regioselectivity of Rh-catalyzed hydroboration of styrene

Our currently understanding of the reaction mechanism states *sbp* hydride migration is sensitive to ligand-substrate steric clash, while *tbp* boryl migrations have no significant ligand-substrate steric repulsion. We thus predict that a bulkier NHC ligands will introduce larger steric clash and disfavor branch selective hydride migration and promote linear regioselectivity. To testify this hypothesis, Figure 36 presents computed $\Delta G^{\ddagger}$ of hydride and boryl migration with a group of NHC ligands with distinct steric properties. Among the set, **L3** with no *N*-substituent is the least sterically hindered while **L5** with *t*-Bu *N*-substituent is the most sterically hindered. Blue bars represent $\Delta G^{\ddagger}$ of boryl migration transition states that is not sensitive to steric properties of NHC ligands. The fluctuation of energy is primarily due to electronic effects – qualitatively, better donor ligands with smaller TEP promote reactivity along both pathways. As expected, no linear correlation is observed between $\Delta G^{\ddagger}_{linear}$ and cone angle. The pink bars represent $\Delta G^{\ddagger}$ of hydride migration transition states that is susceptible to ligand steric effect. Good linear correlation (R^2=0.85) is observed between $\Delta G^{\ddagger}_{branched}$ and cone angle. It is clear that sterically less hindered ligands **L3** and **L2** have smaller hydride migration barrier, where sterically bulky ligand **L5** lead to larger hydride migration barrier. As a result, $\Delta\Delta G^{\ddagger}$ with the bulkiest NHC ligand **L5** predicts linear regioselectivity, while the least bulky NHC ligand **L3** predicts branched selectivity.

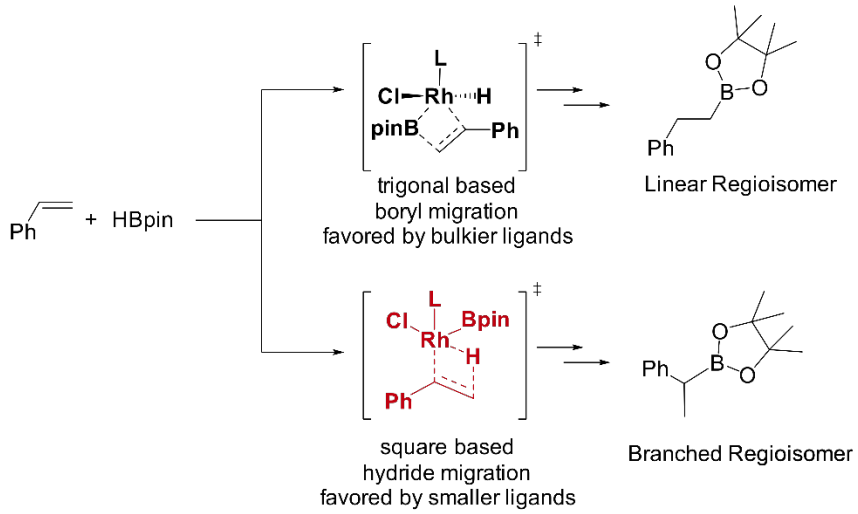

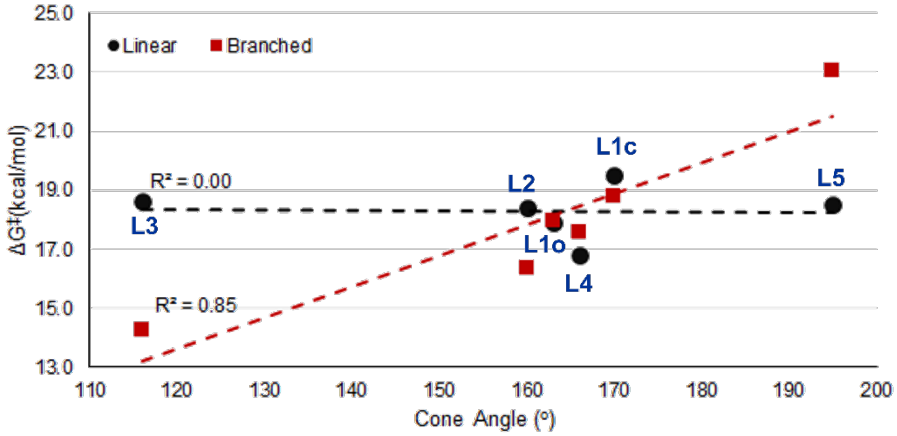

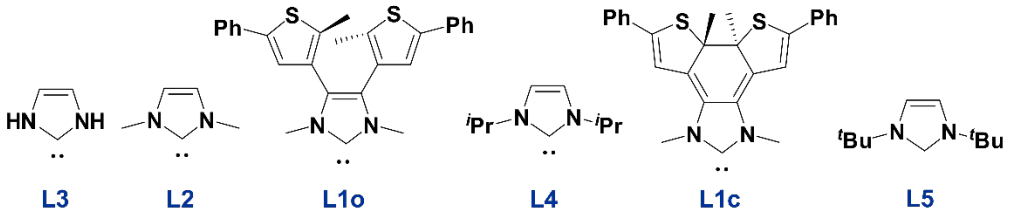

L =	L3	L2	L1o	L4	L1c	L5
Cone Angle (°)	116	160	163	166	170	195
TEP (cm^{-1})	2058	2054	2051	2051	2056	2050
Predicted Regioselectivity	**Branched**	**Branched**	Mixed	Mixed	Mixed	**Linear**

Figure 36. a). Reaction mechanism of Rh(NHC)Cl catalyzed hydroboration of styrene, where linear and branched regioisomers formed through distinct pathways. b). Effects of NHC ligands on reactivity and regioselectivity of hydroboration of styrene

([a.] Vibrational frequencies computed with mPW1PW91/6-311+G(2d)-6-311+G(d,p) in the gas phase in $Ni(CO)_3L$)

4.4 SUMMARY

This chapter presented a computational investigation on reaction mechanism of Rh-catalyzed hydroboration of styrene with PPh_3 and NHC ligand. In contrast to the phosphine-ligated Rh(I) catalyzed hydroboration of styrene, which forms both linear and branched regioisomers through the hydride migration pathway, the favored pathways to form the linear and branched regioisomers with the Rh(NHC)Cl catalyst are boryl migration and hydride migration, respectively. The effects of NHC ligands on reaction mechanism, regioselectivity and reactivity is also presented. As the branched and linear products are formed through fundamentally different rate-determining transition states, the following design principles were concluded for Rh(NHC)Cl catalyzed hydroboration reactions: 1). Better donor ancillary ligands, evidenced by smaller Tolman electronic parameter (TEP), promote formation of both linear and branched products; 2). Bulky NHC ligands with large cone angles suppress hydride migration, which is more sensitive to steric repulsions. This makes the linear-selective boryl migration more favorable; 3). PPh_3 and smaller NHC ligands with smaller cone angles favor the branched product through the hydride migration pathways. These summarized design principles of Rh-NHC catalysts can be used to develop new catalysts with enhanced reactivity and switchable catalysts for otheer hydroboration and other hydrofunctionalization reactions.

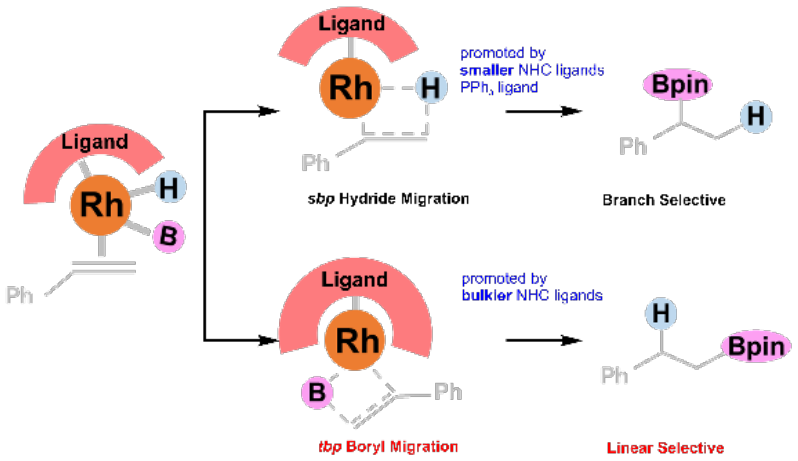

Figure 37. Effects of ligand on reaction mechanism and regioselectivity of Rh-catalyzed hydroboration of styrene

CHAPTER 5. EFFECTS OF SUBSTRATES AND DIRECTING GROUPS ON REGIO- AND ENANTIOSELECTIVITY IN CATALYTIC ASYMMETRIC HYDROBORATION OF ALKENES

5.1 INTRODUCTION

Rh catalyzed asymmetric hydroboration of styrene is an effective approach to install new chiral centers in organic synthesis with highly controlled chemo-, regio-, and enantioselecitivities. The achieved boronic esters can be further functionalized to generate chiral alcohols and amines.[62],[63] Numerous studies have been reported to synthesize primary and secondary chiral organoboron derivatives. For example, various ligands have been reported effective in Rh-catalyzed CAHB of styrene including the chiral bidentate P,P-ligands BINAP[64] and Josiphos[65], the P,N-ligands QUINAP[66], PYPHOS[67], and the ferrocenylpyrazole derivative **1**[68] with good yield, regioselectivity and enantioselectivity. (Figure 38).

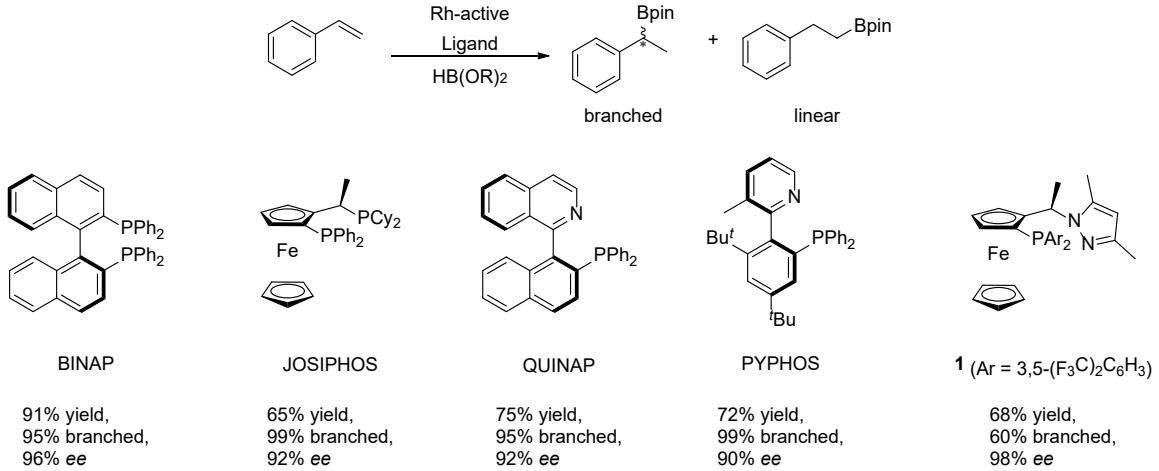

Figure 38. Ligands used in Rh-catalyzed asymmetric hydroboration to generate secondary boronic esters

Synthesis of tertiary boronic esters, despite their importance as precursors to tertiary alcohols, amines, and all carbon quaternary centers, has been a great challenge in transition metal catalyzed hydroboration. Current synthetic approaches are limited to Cu-catalyzed enantioselective borylations with $(Bpin)_2$ as the boryl source. In 2010, Shibasaki[69] and Yun[70] independently developed copper catalyzed conjugate borylation of β, β-substituted aryl substrate (Figure 39 a,b); while Hoveyda group probed the problem by using Cu-NHC catalyst to synthesize tertiary boronic esters.[71](Figure 39 d) One drawback of the Cu-catalyzed borylation protocols is that it always requires the presence of a strong base. In 2015, Tang group presented a study using **L4** incorporated Rh-complex to catalyze enantioselective borylation to synthesis α-amino tertiary boronic esters with moderate yield (69%) and up to 99% ee (Figure 39 d).[72] In all listed hydroboration reactions, $(Bpin)_2$ serves as the borane source, which does not utilize desired atom economy.[73]

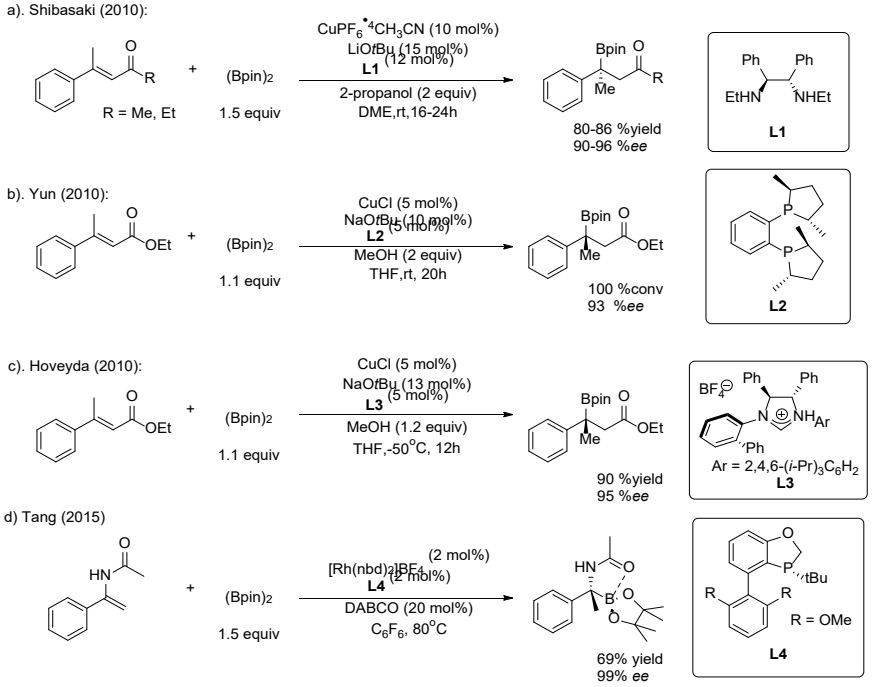

Figure 39. Cu- and Rh-catalyzed non-directed hydroboration of activated aryl olefins to form tertiary boronic esters

Since 2011, the Takacs group at the University of Nebraska-Lincoln published a series of studies in Rh-catalyzed CAHB reactions of *β,γ*-unsaturated substrates with high enantioselectivity under mild conditions.[74] In their earlier publications, they have demonstrated the efficient CAHB of allylic trisubstituted alkenes with oxime and phosphonate directing groups.[75] However, the synthesis of chiral tertiary benzylic boronic esters is not achieved until recently.[76] Using the TADDOL-derived phosphite T1 in combination with a common Rh(I) catalyst precursor, the phosphonate-directed of β-aryl-substituted methylidene substrate **2** undergoes borylation at more substituted position of the alkene, generating β-borylation product (R)-**3** (81%, 97:3 %er) with *re*-facial selectivity (Figure 40a). Interestingly, the TADDOL-derived asymmetric ligand controls the π-facial selectivity of the reaction through two distinct stereo centers on the backbone. The favored conformation and the steric environment of this T1/T2 ligand scaffold and its effect on enantioselectivity in Rh-catalyzed hydroboration reactions have not been investigated computationally. Effects of directing group on regioselectivity of CAHB reactions also remain unclear. With the oxime ether directing group, the CAHB of similar methylidene substrates **4** produces the other regiosomeric γ-borylation product (R)-**5** (70%, 95:5 %er) with same *re*-facial selectivity.

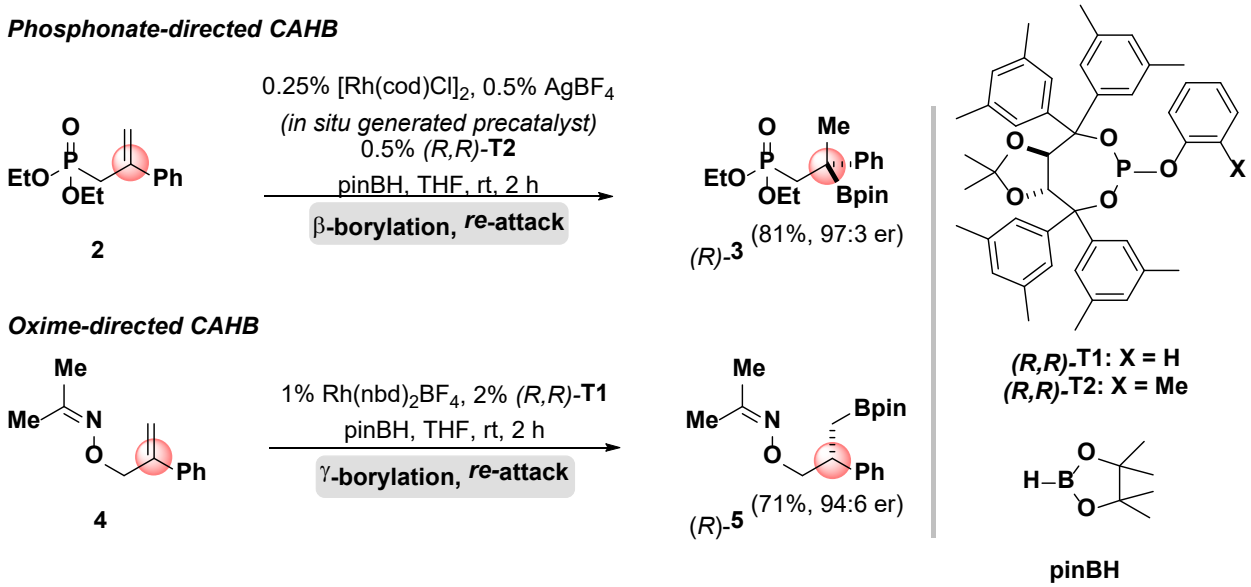

Figure 40. Rh-catalyzed directed CAHB of methylidene vinyl arenes with a). Phosphonate directing group, and b) Oxime directing group

Takacs group presented a ab inito study of the reaction mechanism of Rh-catalyzed cyclic *γ,δ*–unsaturated amide with carbonyl directing group. They investigated the two-point binding mechanism where the directing group of the substrate coordinates onto the Rh-center to form a chelating type of interaction. They concluded that the rate-determining transition state is the secondary C-B bond reductive elimination.[77]

To our knowledge, no computational studies have been presented on the Rh-catalyzed phosphonate directed CAHB of aryl substrates to form the sterically demanding tertiary C- B bond. The generally accepted proposed mechanism is illustrated in Figure 41a.[52] upon coordination of the substrate and the HBpin, complex **6** undergoes oxidative addition to form 5-coordinated Rh(III) complex **7**. Similar to the proposed mechanism in Chapter 4, subsequent migratory insertion of the olefin could occur via four competing pathways involving either insertion into the Rh-B or the Rh-H bond with two regioisomeric approaches of the olefin. 2,1 and 1,2 olefin insertion into Rh-H bond (i.e. hydride migration) form 5-membered metallacycle **8** and 6- membered metallacycle **11**

which then undergo C-B reductive elimination to release the linear and branched products **12** and **3**, respectively. Similarly, 2,1 and 1,2 olefin insertion into the Rh-B bond (i.e. boryl migration) forms 5-membered metallacycle **11** and 6-membered metallacycle **10** which then undergo C-H reductive elimination to release the linear and branched products **12** and **3**, respectively.

In following sections of this chapter, I will first conduct DFT calculations to reveal the favored reaction mechanism of Rh-catalyzed directed CAHB and to identify the rate- and selectivity- determining step. The second goal of computational studies is to determine factors promoting formation of the sterically demanding tertiary C-B bond. One hypothesis is that T1/T2 ligand could serve as a semi-labile ancillary ligand, where the ligand backbone Ar group or the OPh could bind reversibly onto Rh center to stabilize 4-coordinated metallacycle intermediates and/or reductive elimination transition states. (Figure 41b) Based on the computed RDS structures, I will then analyze the conformation of free T1 ligand and its effect on enantioselectivity. The last goal of this chapter is to investigate effects of directing group on regioselectivity and provide guidance in designing directing group controlled CAHB reactions.

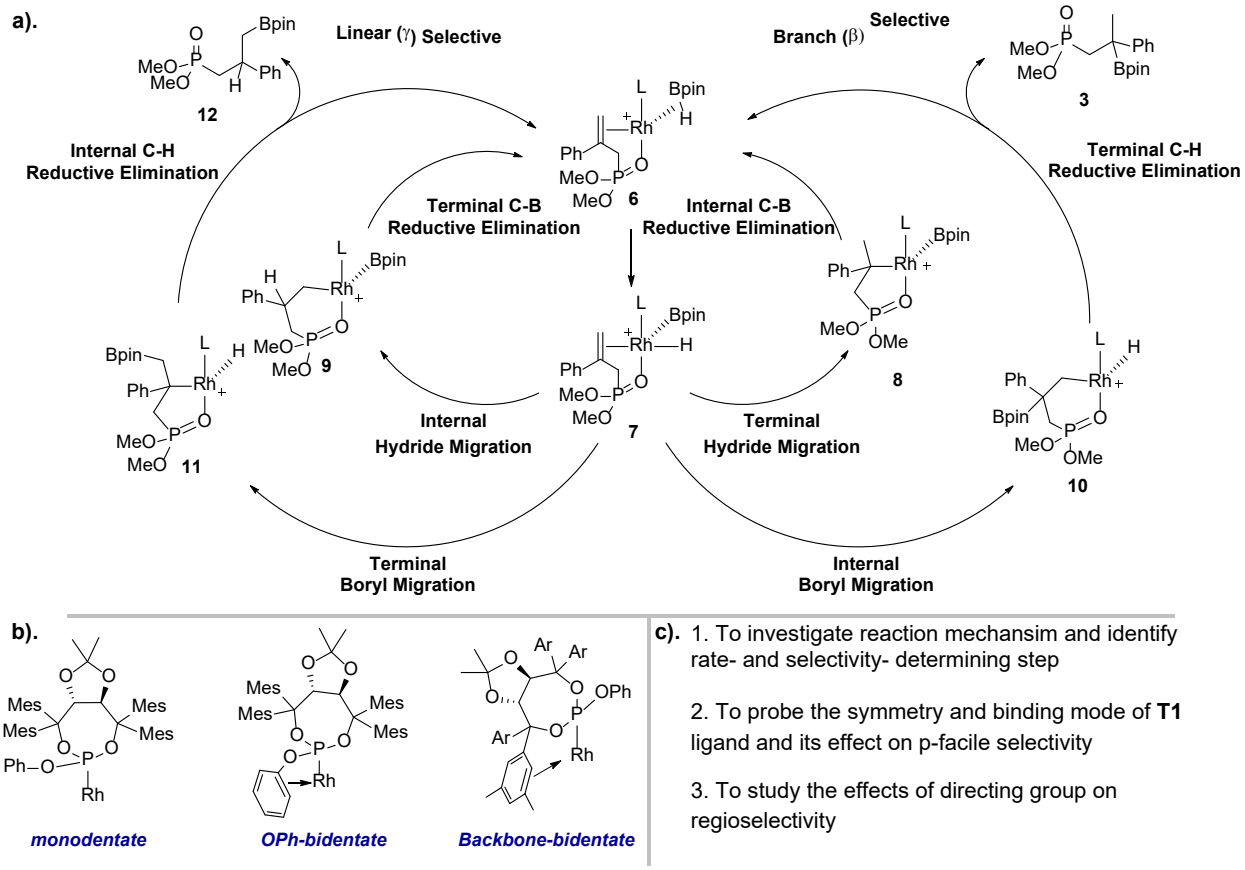

Figure 41. a) Proposed reaction mechanism of Rh-catalyzed CAHB of phosphonate directed methylidene vinyl arenes ; b) Possible binding modes of the asymmetric phosphite ligand on Rh; c) Goals of computational investigation

5.2 COMPUTATIONAL DETAILS

All geometry optimizations were performed using the dispersion corrected B3LYP-D3 functional[18,78] with a mixed basis set of SDD for Rh and 6-31G(d) for other atoms.[44] Single point energies were calculated with M06[11] and a mixed basis set of SDD for Rh and 6-311+G(d,p) for other atoms. Solvation effects were considered by performing single point calculations with the SMD model in THF (ε = 7.4).[13,14] All calculations were performed with Gaussian 16.[79]

Reaction energy profiles presented in this study were obtained by optimizing molecular geometries and calculating energies of the reaction intermediates (local minima) and transition states (1st order saddle point) along plausible reaction pathways. Vibrational frequencies were computed at the same level of theory in geometry optimization to confirm whether the structures are intermediates (no imaginary frequency) or transition states (only one imaginary frequency).

The reported Gibbs free energies and enthalpies include zero-point vibrational energies and thermal corrections at 298 K calculated using a harmonic-oscillator model. Since the harmonic-oscillator approximation may lead to spurious results for the computed entropies in molecules with low-frequency vibrational modes,[16] the quasiharmonic approximation from Cramer and Truhlar[17] was applied to compute the thermal corrections for a few key transition state structures. In the quasiharmonic approximation, vibrational frequencies lower than 100 cm-1 were raised to 100 cm-1 as a way to avoid spurious results associated with the harmonic-oscillator model for very low-frequency vibrations. The reported energies in the text were corrected using the quasiharmonic approximation. The Gibbs free energies in solution were calculated at 1 mol/L.

5.3 RESULTS AND DISCUSSION

5.3.1 Reaction mechanisms of phosphonate directed CAHB

This section presents computational mechanistic investigation of Rh-catalyzed CAHB of x with phosphonate directing group. Oxidative addition of HBpin generates the common Rh(III) intermediate **7**, which act as the resting state in the computed reaction energy profile in Figure 42.

For the sake of clearness, only the four *re*-selective styrene migratory insertion pathways from **7** are presented. The blue pathways represent the hydride migration mechanism, where olefin inserts into Rh-H bond; and the black pathways account for the boryl migration mechanism, where olefin inserts into Rh-B bond. The 2,1-hydride migration (**TS1**), where the hydride migrates onto the terminal carbon, and the 1,2-boryl migration (**TS3**), where the Bpin group migrates onto the internal carbon, lead to the β-borylation product **3**. The 2,1-boryl migration (**TS2**) and the 1,2-hydride migration (**TS4**) produce the gamma borylation product **12**. The 2,1-boryl and hydride migrations (**TS1** and **TS2**) to form benzylic rhodium complexes **8** and **9** are favored over corresponding 1,2-migration pathways (**TS3** and **TS4**) due to electronic stabilization of the α-Ph substituent that delocalizes the partial negative charge on the α carbon. Subsequently, the benzylic Rh(III) intermediates **8** and **11** undergo sterically demanding tertiary C-B reductive elimination **TS5** and energetically facile tertiary C-H reductive elimination **TS6** to form β- and γ- borylation products (**3** and **12**), respectively. The rate- and regioselectivity determining step (RDS) of the β-borylation pathway is sterically demanding tertiary C-B reductive elimination **TS5** with a barrier of 15.8 kcal/mol; the RDS of the γ-borylation pathway is the 2,1 boryl migration **TS2** with a barrier of 16.5 kcal/mol. In consistence with experimental observation, the computed Gibbs free energies suggested β-borylation is favored over γ-borylation.

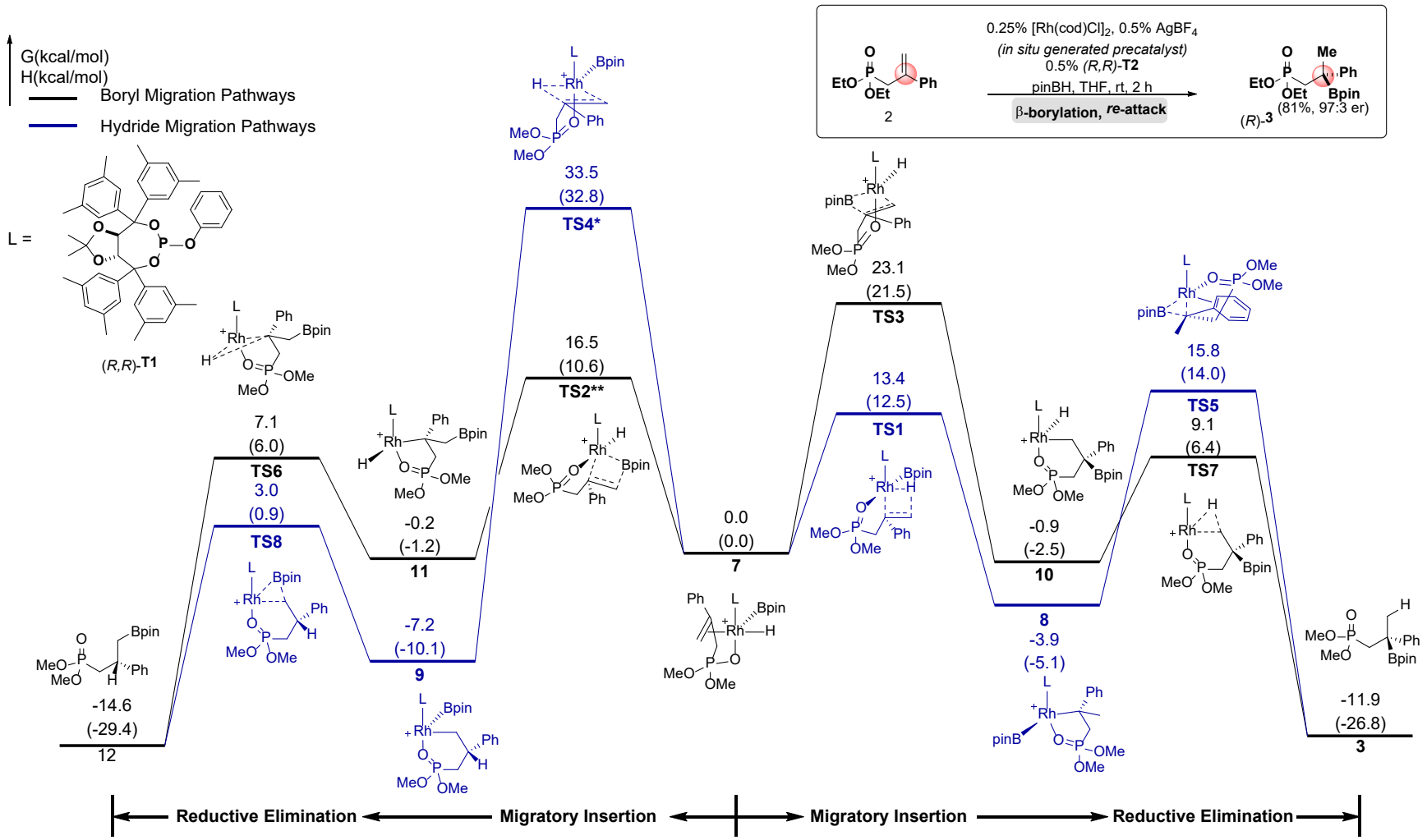

Figure 42. Calculated energy profile for Rh(IMe)Cl catalyzed hydroboration of phosphonate directed aryl alkene with re-facial selectivity
(All energies are with respect to the 5-coordinated Rh(III) complex 2) ((*Geometry optimization of TS2 is conducted at B3LYP-D3/LANL2DZ−6-31G(d) level of theory with energy computed at M06/SDD-6-311+G(d,p)/SMD (THF) level of theory, **The reported energy is estimated from the constrained ModRedundant calculations)

The optimized migratory insertion transition states (**TS1, TS4**) along the favored reaction pathways are presented in Figure 43. Consistent with observations described in Chapter 4, hydride migration **TS1** adapts the electronically favored square based pyramidal (*sbp*) conformation with inserting hydride ligand at apical position, and phosphonate directing group *cis* to ligand. **TS1_bottom** is favored over **TS1_side** due to *trans*-effect of the strong sigma donor ligand Bpin. The phosphonate directing group is a relatively weaker *trans* ligand comparing to the inserting olefin. Boryl migration **TS4** adapts the sterically less demanding trigonal bipyramidal (*tbp*) conformation with hydride and directing group occupying axial positions. The steric repulsion between phosphite ligand and Bpin determines the energy difference between **TS2_bottom** and **TS2_side**. **TS2_bottom** is sterically favored by putting both sterically demanding Bpin and ancillary phosphine ligand in equatorial positions and small hydride and directing phosphonate in axial positions. In consistent with the conclusion of previous section, with relative flexible and sterically less demanding phosphonate ancillary ligand, the hydride migration energetically favored over boryl migration evidenced by the relative energy difference between **TS1_bottom** and **TS1_bottom**.

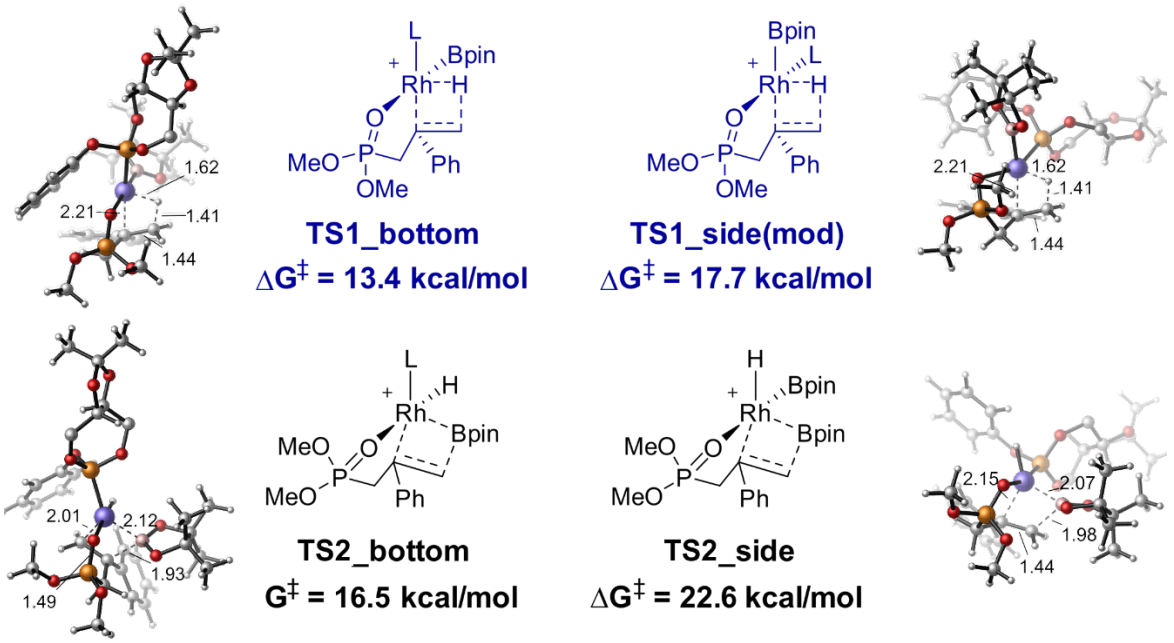

Figure 43. Optimized conformations of square based pyramidal hydride migration transition state (TS1) and trigonal bipyramidal boryl migration transition state (TS4)

A detailed conformational search for resting state complex 2 is also conducted with computed relative energy presented in Figure 44. The 5-coordinated Rh(III) complex adapts square based pyramidal geometry with the phosphonate ligand favors to be *trans* to the directing group, and hydride favors to be *trans* to the alkene substrate. The strongest sigma donor ligand Bpin is located at the apical position. (**7**) The small Gibbs free energy difference between **7** and **14** (2.3 kcal/mol) and **19** (4.4 kcal/mol) ensured easy pseudorotation between intermediates to undergo subsequent migratory insertions.

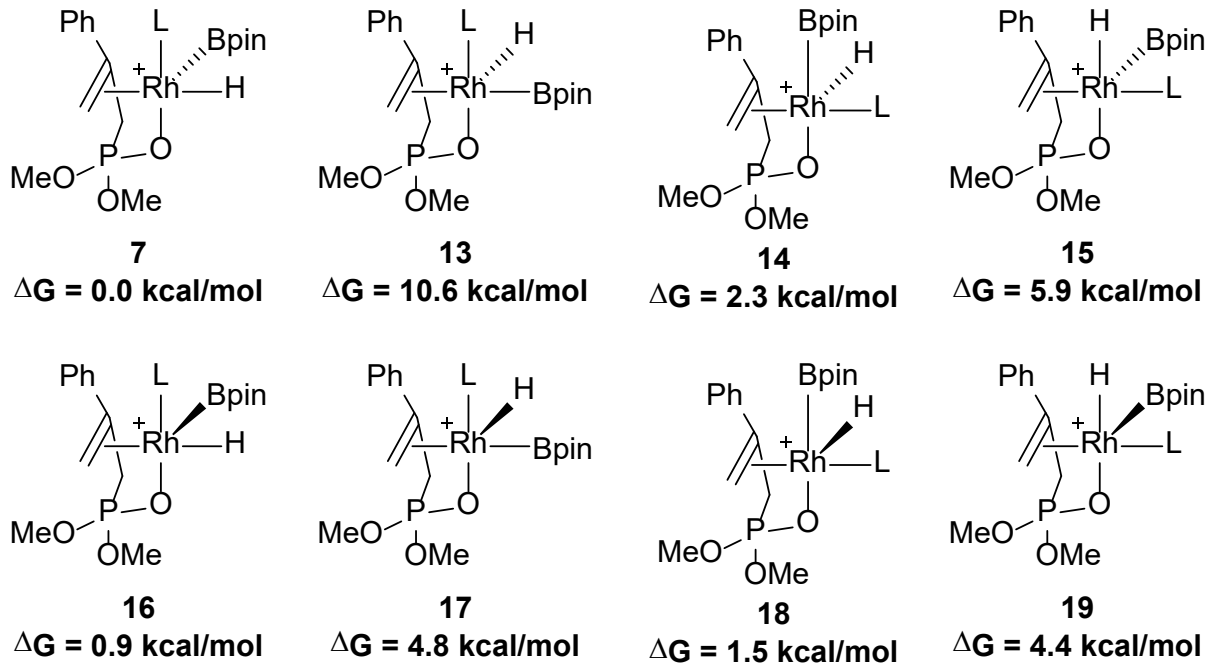

Figure 44. Computed Gibbs free energy of 5-coordinated Rh(III) intermediates

5.3.2 Factors promoting sterically demanding tertiary C-B reductive elimination

One interesting mechanistic feature of this reaction is the formation of β-borylation product through sterically demanding C-B reductive elimination of the tertiary carbon (**TS5**). Detailed conformation search of the metallacycle intermediates **8** and reductive elimination transition state **TS5** revealed that the benzylic group could bind to the Rh-center with a conventional η^1 fashion or a unusual η^3 fashion where the Ph substituent binds onto the Rh center, as evidenced by the relatively short Rh-C distances with the ipso and ortho carbons of the Ph (2.22 Å and 2.29 Å). Consistent with previous studies, formation of the η^3 benzyl complex **8_η³** is disfavored due to loss of aromaticity.[80] The two metallacycle intermediates can interconvert under a Curtin-Hammett condition as illustrated in Figure 47.

Although the benzyl η^3-complexes have been observed, no computational studies have been reported to investigate its role in promoting sterically demanding C-B bond formation in Rh-catalyzed CAHB reactions. In reductive elimination transition states, **TS5_η^3** is energetically favored over **TS5_η^1** by 3.9 kcal/mol. Closer examination of the computed transition state 3-D structures revealed that the η^3 coordination of Ph ring makes **TS5** sterically less crowded. Compared to the C-B distance in **TS5_η^1** (1.89 Å), the enlongated C-B distance in **TS5_η^3** (2.05Å) reduces steric tension between inserting Bpin and the substituent and consequently promotes the reactivity of the sterically demanding tertiary C-B bond reductive elimination. This represents the first example that benzylic η^3 coordination with a Rh center promotes a sterically demanding bond formation.

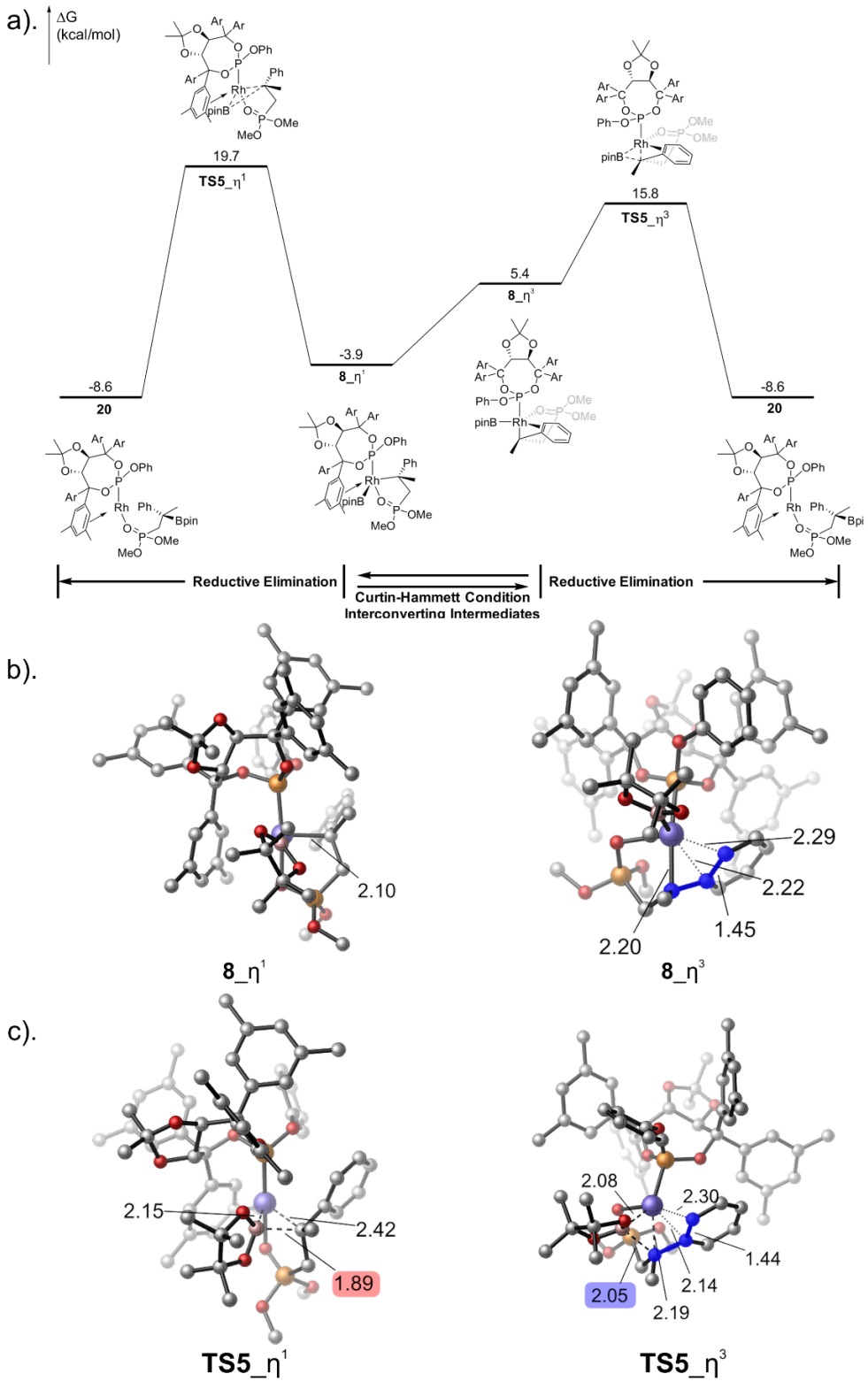

Figure 45. η3-Rh-Ph interaction promoted tertiary C-B reductive elimination by release of steric repulsion [Ar groups on the ligand have been concealed for the sake of clearness][IM_η1 and IM_η3 are in Curtin Hammett condition]

5.3.3 Procedure to generate ligand steric contour plot from optimized ligand geometry

As introduced in first chapter, ligand steric contour plot serves as a great tool to visualize and rationalize ligand conformations. [81] Figure 45 illustrated the procedure to create the steric contour plot of the (*R,R*)-T1 ligand.

a) The ligand structure is optimized at the same level of theory as other calculations in this chapter (B3LYP-D3/SDD-6-31G(d,p)).

- A hypothetical Rh atom is installed in equatorial position at the phosphine atom (with Rh-P distance 2.30 Å), the ligand is then rotated and translated so that the Rh atom is placed at the origin of the Cartesian coordinate system (0.0, 0.0, 0.0).
- The *z* axis is oriented along the Rh-P bond. The ligand is placed in the half-space along the positive *z* axis (with positive *z* coordinates).
- The *x* axis is oriented along the two carbon atoms on the ligand backbone. Note that the definition of these axis can be tailored depending on the system studied.
- An example of the rotated/translated coordinates is provided below:

	x	***y***	***z***
Ir	0.00000	0.00000	0.00000
P	0.00000	0.00000	2.30000
C	1.95269	0.00000	4.37349
C	-1.36784	1.43257	4.33854
…	…	…	…

b) The Van der Waals surface of the ligand was built up using the atomic radii as tabulated in A. Bondi, "Van der Waals Volumes and Radii", *Journal of Physical Chemistry*, Vol. 68, No. 3, pp. 441, 1964. H atoms are included in the Van der Waals surface.

c) The contour map of the ligand was plotted using the matplotlib library in Python. The contour lines are created along the *z* axis. The contour line of zero is drawn through all points on the van der Waals surface having the same *z* coordinate as the Ir atom. The positive contour lines (colored in green and blue) indicate regions on the ligand van der Waals surface having a positive *z* coordinate, *i.e.* more distant from the half-space containing the substrate. The negative contour lines (colored in yellow and red) indicate regions on the ligand surface with a negative *z* coordinate, i.e. closer to the half-space containing the substrate. Thus, if a substrate is placed in a yellow or red region on the ligand contour plot, more significant ligand-substrate interaction is expected. The unit on the colour bar for the contour lines is in Å.

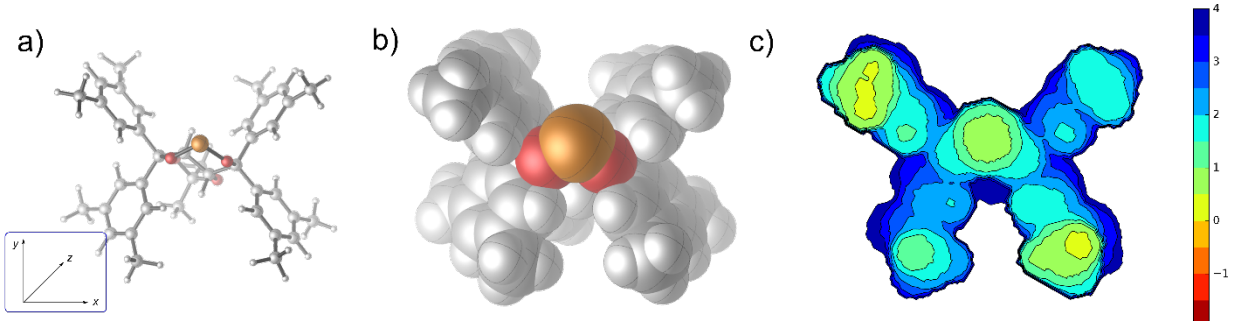

Figure 46. Illustration on the procedure to create steric contour plot from DFT optimized geometry

5.3.4 Application of ligand steric contour plot to study conformation of the asymmetric T1 ligands

To elucidate the steric environment and the mode of chiral induction with the asymmetric **T1** ligand, this section uses steric contour plot and quadrant diagram to study the conformations of monodentate asymmetric phosphite ligand (*R,R*)-T1 and (*S,S*)-T1. Figure 47a revealed that both **T1** ligands adapt chair conformation, where P-O^2-C^4-C^1 locates on the same plane and O^2-C^2-C^3-C^4 locates on another plane. When this ligand coordinates on to an Rh center (highlighted in red), the Rh is expected to locate at the sterically less demanding equatorial position. Take (*R,R*)-T1 ligand for example, the Ar groups at equatorial positions (Ar^2 and Ar^3) are expected to point towards the Rh-center and thus be placed in closer proximity to the metal than the axial Ar groups (Ar^1 and Ar^4). Here, we define the quadrant occupied by the equatorial Ar groups (Ar^2 and Ar^3) as "occupied" quadrants. With (*S,S*)-T1 ligand, Ar^2 and Ar^3 locate at axial positions, while Ar^1 and Ar^4 are in equatorial positions. Indeed, the steric contour plots indicate a pseudo-C_2 symmetry for the **T1** ligand. (Figure 47c) In (*R,R*)-T1 ligand, Ar^1 and Ar^4 in first and third quadrant tilt away from the Rh center creating relative open pockets, while Ar^2 and Ar^3 in second and fourth quadrant tilts toward Rh center creating relative occupied pocket. While, in (*S,S*)-T1 ligand, Ar^2 and Ar^3 lie in relative open pockets, while Ar^1 and Ar^4 in relative occupied pocket. The stereocenters on **T1** ligand backbone introduces an achiral environment around the metal center through the four Ar groups on the ligand backbone.

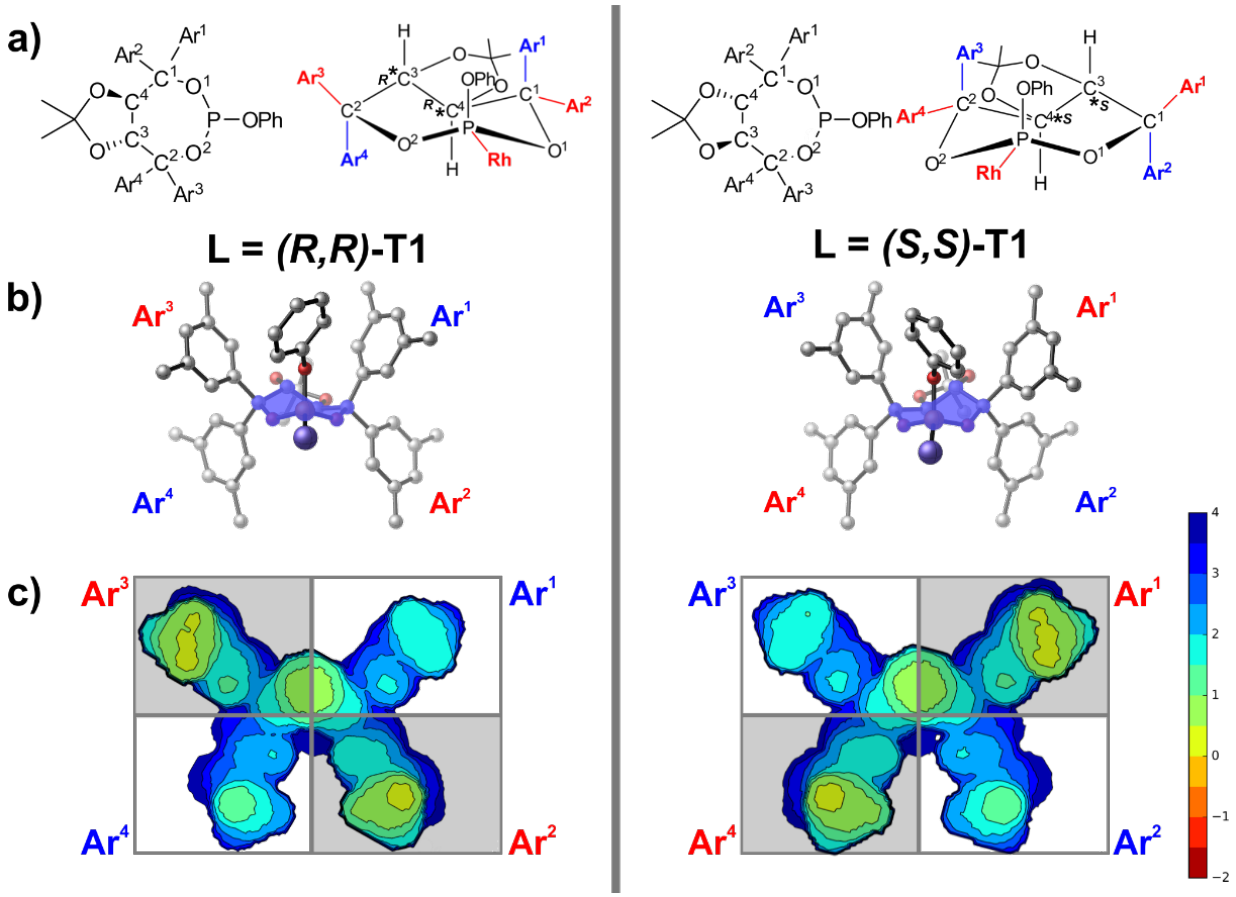

Figure 47. Conformation and steric environment of asymmetric (R,R)-T1 and (S,S)-T1 ligands, a) chair conformation of the asymmetric ligands; b) computed 3-D structures of the T1 ligands; c) Steric contour plot and the quadrant diagram of the ligand, view from Rh-P
(all hydrogens concealed for the sake of clearness)

5.3.5 Origin of enantioselectivity in phosphonate directed CAHB

Following the discussion of pseudo-C_2 symmetric (*R,R*)-**T1** ligand, this section further elucidates the origin of enantioselectivity in Rh-catalyzed phosphonate directed CAHB reactions. The computed Gibbs free energy of **TS5_*R*** and **TS5_*S*** with respect to the common Rh(III) intermediate **2** is presented along with the optimized 3-D structures. Consistent with experimental observation, **TS5_*R*** is energetically favored over **TS5_*S*** by 1.4 kcal/mol, leading to *re* facial selectivity. As presented in Figure 48, the ligand in **TS5_*S*** is clearly more distorted. This is

evidenced by the computed $E_{distortion}$ and the loss of C_2 symmetry, suggesting ligand distortion energy is the one major contributor to observed facial selectivity.

The origin of ligand distortion in **TS5_*S*** is then analyzed with ligand steric contour overlay plot. The steric contour plot is created following procedures described in previous section with substrates overlaid on top of it. The significant change of ligand shape in **TS5_*S*** is in consistent with the higher ligand distortion energy ($E_{distortion}$=5.5kcal/mol). Closer examination of the ligand conformation in computed transition states revealed the origin of disfavored ligand distortion in **TS5_*S***. As discussed in section 5.3.1, the favored reductive elimination transition state **TS5** adapts square based pyramidal conformation, where the phosphonate directing group and the η^3 coordinated Ph ring are in axial position. The η^3 coordinated Ph ring represent the most steric demanding group (highlighted in red) *cis* to the phosphine ligand. As illustrated in Figure 48b, in favored **TS5_*R***, the Ph ring locates at the open quadrant 1 below Ar^1, resulting in less ligand distortion and favored Gibbs free energy ($\Delta G^{\ddagger}$=15.8 kcal/mol); In disfavored **TS5_*S***, the Ph ring locates at the occupied second quadrant below Ar^3, resulting in more significant and disfavored Gibbs free energy of activation ($\Delta G^{\ddagger}$=17.2kcal/mol).

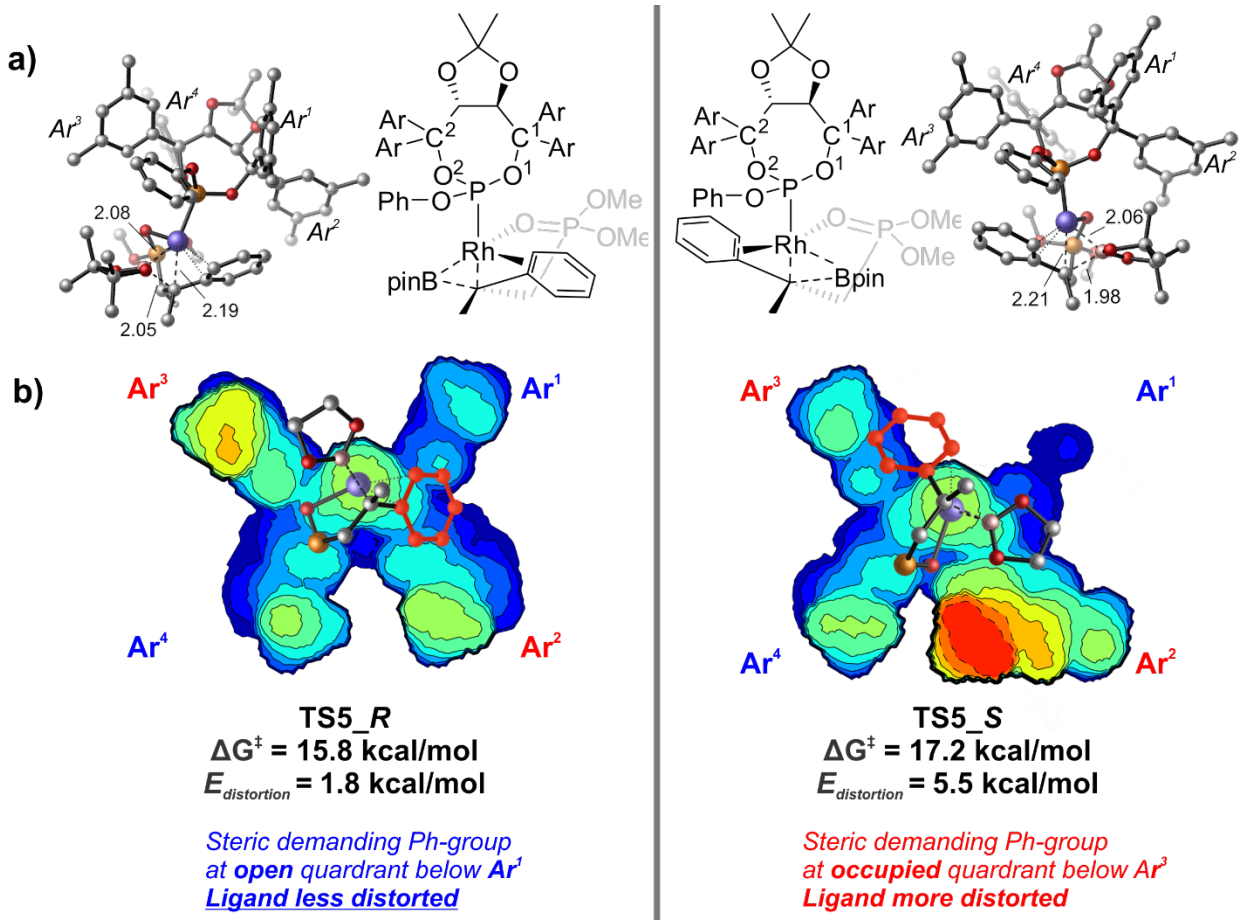

Figure 48. Demonstration of the origin of enantioselectivity. a) computed 3-D structures of the tertiary reductive elimination transition states; b) Steric contour plot with substrate overlaid on the top (all hydrogens concealed for clarity) (the most steric demanding Ph-group is labeled red)

5.3.6 Reaction mechanism of oxime directed CAHB

This section presents mechanistic investigation of Rh-catalyzed CAHB of x with the oxime directing group. The computed reaction energy profiles containing four competing reaction pathways are presented in Figure 49. From the reactant complex **21**, four competing styrene migratory insertion pathways lead to two regioisomeric hydroboration products. The blue pathways represent the hydride migration mechanism, where olefin inserts into Rh-H bond; and the black pathways account for the boryl migration mechanism, where olefin inserts into Rh-B

bond. The 2,1-hydride migration (**TS9**), where the hydride migrates onto the terminal carbon, and the 1,2-boryl migration (**TS11**), where the Bpin group migrates onto the internal carbon, lead to the beta-borylation product **5**. The 2,1-boryl migration (**TS10**) and the 1,2-hydride migration (**TS12**) eventually produce the γ-borylation product **26**. The 2,1-hydride and boryl migrations (**TS9** and **TS10**) to form benzylic rhodium complexes **22** and **25** are favored over corresponding 1,2-migration pathways (**TS11** and **TS12**) due to electronic stabilization of the α-Ph substituent that delocalizes the partial negative charge on the α carbon. Subsequently, the benzylic Rh(III) intermediates **22** and **25** undergo sterically demanding tertiary C-B reductive elimination **TS13** and relative facile tertiary C-H reductive elimination **TS16** to form β- and γ- borylation products (**5** and **26**), respectively. The (RDS) of the beta-borylation pathway is sterically demanding C-B reductive elimination **TS13** with a barrier of 22.9 kcal/mol; the RDS of the γ-borylation pathway is the C-H reductive elimination **TS16** with a barrier of 16.6 kcal/mol. In consistence with experimental observation, the computed Gibbs free energies suggested γ-borylation is favored over β-borylation.

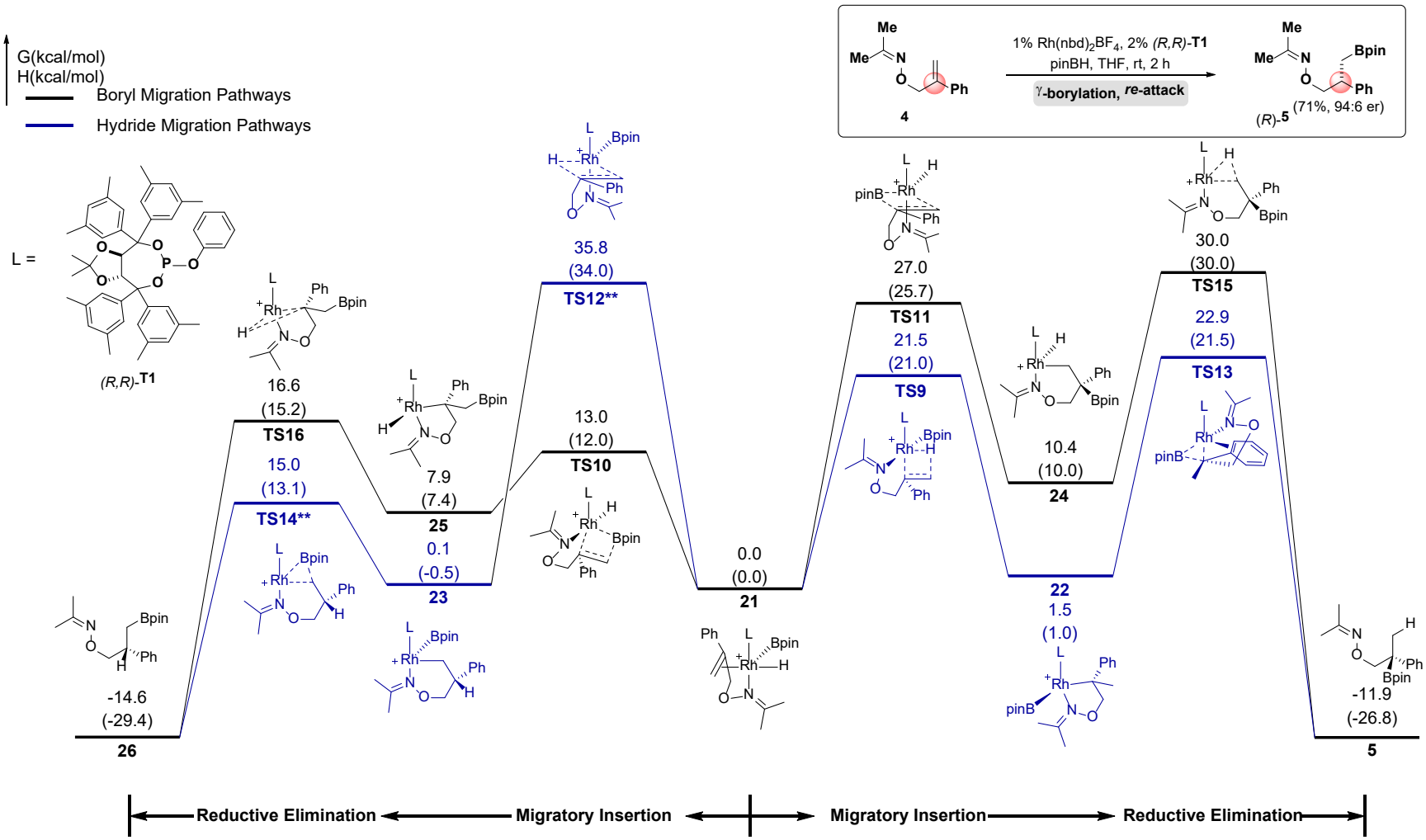

Figure 49. Calculated energy profile for Rh(IMe)Cl catalyzed hydroboration of oxime directed aryl alkene with *re*-facial selectivity

(All energies are with respect to the 5-coordinated Rh(III) complex 2)

((*Geometry optimization of TS2 is conducted at B3LYP-D3/LANL2DZ−6-31G(d) level of theory with energy computed at M06/SDD−6-311+G(d,p)/SMD (THF) level of theory**The reported energy is estimated from the constrained ModRedundant calculations)

5.3.7 Effect of directing group on regioselectivity

One interesting observation is that the regioselectivity is completely reversed to favor γ-borylation with the oxime directing group. Examination of the optimized RDS indicated that two factors contribute to the increased free energy barrier in **TS13_*R***. Electronically, the η^3-Ph coordination is weakened in **TS13_*R*** evidenced by the elongated Rh-C distances (2.36Å and 2.17Å) comparing to those in **TS5_*R*** (2.30Å and 2.14Å). This could be attributed to the electronic effect of the directing group: giving its weaker electronegativity, N lone pair serves as a stronger electron donor ligand than O lone pair and makes the Rh center more electron-rich. Sterically, the oxime directing group is more sterically demanding comparing to the phosphonate directing group, leading to significant steric repulsion between the N-Me group and the O on ligand backbone. In combination, **TS13_*R*** is disfavored both electronically and sterically, leading to the revision of regioselectivity.

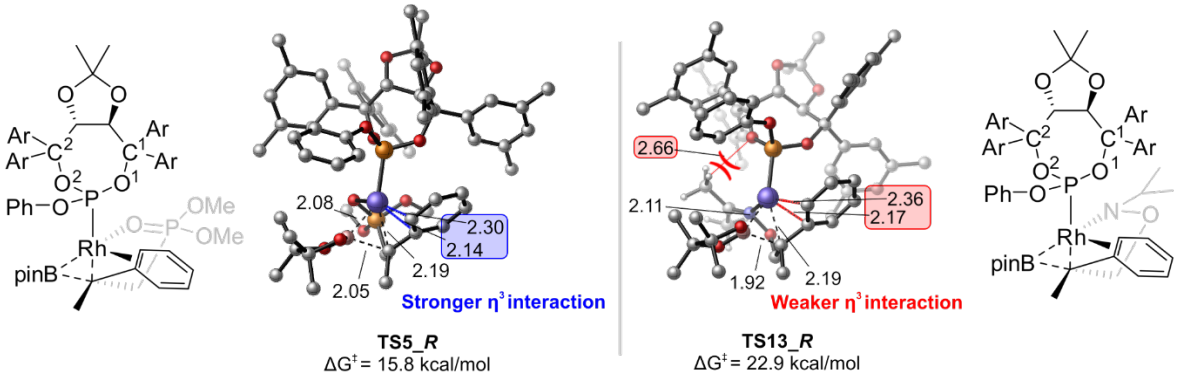

Figure 50. Effects of oxime directing group on regioselectivity determining tertiary C-B bond reductive elimination

5.4 SUMMARY

This chapter presented a computational investigation on Rh-catalyzed phosphonate- and oxime- directed asymmetric hydroboration with asymmetric phosphite ligand **T1** to generate chiral tertiary benzylic boronic esters. The reaction mechanism is investigated by construction of the computed energy profile, where the rate- and selectivity- determining transition state along the β-borylation mechanism is the tertiary C-B reductive elimination. Closer examination of the optimized reductive elimination transition states revealed that an η^3 isomer of the benzylic Rh complex promotes the sterically demanding reductive elimination. The mechanism of chiral induction using **T1** ligand and the ligand effect on enantioselectivity is then investigated. Steric contour plot of the ligand revealed that the monodentate phosphite ligand **T1** adapts a pseudo-C_2 symmetric conformation. The asymmetric **T1** ligand suppresses the *si*-facial selectivity due to disfavored ligand-substrate repulsion with the coordinated η^3-benzyl group. The effects of directing group on regioselectivity is also demonstrated. The tertiary C-B reductive elimination in oxime directed CAHB reaction is disfavored both electronically, through a weaker η^3-coordination, and sterically, as evidenced by the greater steric repulsion between the directing group and the ligand backbone. Overall, this chapter presented the computational investigation on the reaction mechanism of Rh-**T1** catalyzed CAHB reaction. The molecular level of understanding granted from mechanistic studies shall aid future asymmetric catalyst design of directed hydroboration and other hydrofunctionalization reactions.

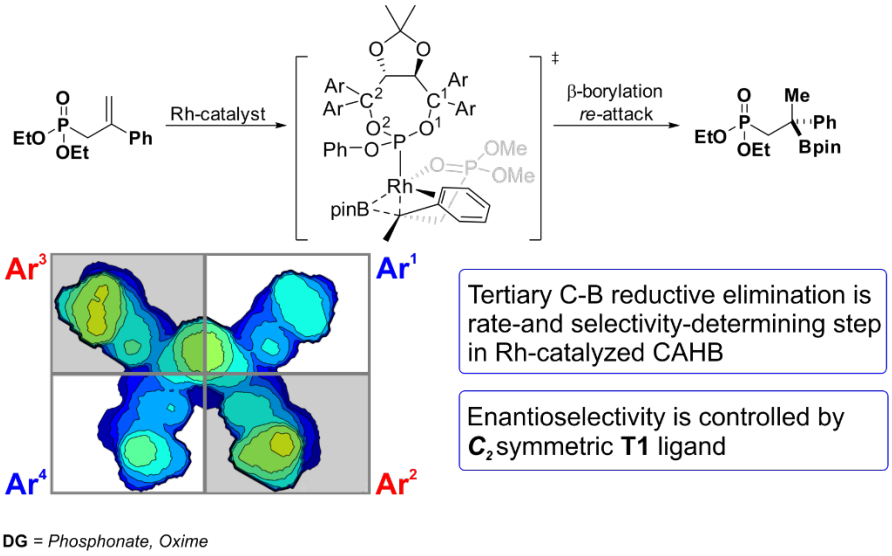

Figure 51. Energetically facile tertiary C-B reductive elimination promoted by η^3-benzyl coordinatio

APPENDIX 1: PUBLICATION AND PRESENTATION LIST

1. **Huiling Shao**.; Yuening Wang.; Christopher W. Bielawski.; Peng Liu: "Computational Study on Effects of Ligands on Mechanism, Reactivity and Selectivity of Rh-catalyzed Hydroboration Reactions," Manuscript in preparation.
2. 6. Crystal K. Chu.; Tzu-Pin Liu.; **Huiling Shao**.; Allegra L. Liberman-Martin.; Peng Liu.; and Robert H. Grubbs: "Disentangling Ligand Effects on Metathesis Catalyst Activity: Experimental and Computational Studies of Ruthenium-Aminophosphine Complexes," *J. Am. Chem. Soc.,* **2018**, 140, 5634-5643
3. 5. Jessica M. Grandner.; **Huiling Shao**.; Robert H. Grubbs.; Peng Liu.; and K. N. Houk: "The Origins of the Stereoretentive Mechanism of Olefin Metathesis with Ru-Dithiolate Catalysts," *J. Org. Chem.* **2017**, 82, 10595-10600
4. Dominika N. Lastovickova.; Aaron J. Teator.; **Huiling Shao**.; Peng Liu.; and Christopher W. Bielawski: "A Redox-Switchable Ring-Closing Metathesis Catalyst," *Inorganic Chemistry Frontiers,* **2017**, 4, 1525-1532
5. 3. Dominika N. Lastovickova.; **Huiling Shao**.; Gang Lu.; Peng Liu.; and Christopher W. Bielawski.: "A Ring-Opening Metathesis Polymerization Catalyst That Exhibits Redox-Switchable Monomer Selectivities," *Chem. Eur. J.* **2016**, 23, 5994-6000.
6. 2. Aaron J. Teator.; **Huiling Shao**.; Gang Lu.; Peng Liu.; and Christopher W. Bielawski.: "A Photoswitchable Olefin Metathesis Catalyst," *Organometallics*. **2016**, 36, 490-497.

7. Gang Lu, **Huiling Shao**, Humair Omer, Peng Liu: “Issues Particular to Organometallic Reactions” in “Applied Theoretical Organic Chemistry”, Dean J Tantillo, World Scientific (2016)

APPENDIX 2: LIST OF CONFERENCE PRESENTATIONS

1. **Huiling Shao**, Christopher W. Bielawski, Peng Liu, *Effects of Ligand on Mechanism, Reactivity and Selectivity of Rh-catalyzed Hydroboration of Styrene,* Poster presented at Gordon Research Conference on Computational Chemistry, July 2018, West Dover, VT
2. **Huiling Shao**, Christopher W. Bielawski, Peng Liu, *Effects of Ligand on Mechanism, Reactivity and Selectivity of Rh-catalyzed Hydroboration of Styrene,* Poster presented at Pittsrbugh Quantum Institute-2018 Meeting, April 2018, Pittsburgh, PA
3. **Huiling Shao**, Peng Liu, *Computational Study of Photo- and Redox-Switchable Ring- Opening Metathesis Polymerization,* Oral presentational at 254TH American Chemical Society National Meeting & Exposition – Chemistry's Impact on the Global Economy, August 2017, Washington, DC
4. **Huiling Shao**, Christopher W. Bielawski, Peng Liu, *Effects of Ligands on Mechanism, Reactivity and Selectivity of Rh-catalyzed Hydroboration of Styrene,* Poster presented at Pittsrbugh Quantum Institute-2017 Meeting, April 2018, Pittsburgh, PA

BIBLIOGRAPHY

1. Sutthasupa, S., Shiotsuki, M., & Sanda, F. (2010). Recent advances in ring-opening metathesis polymerization, and application to synthesis of functional materials.*Polymer journal*,*42*(12), 905.

2. For reviews of olefin metathesis in industry, see: a). Mol, J. C. (2004). Industrial applications of olefin metathesis. *Journal of Molecular Catalysis A: Chemical*, *213*(1), 39-45.; .b) Grela, K. (2014). *Olefin metathesis: theory and practice*. John Wiley & Sons. pp 329−333.

3. For reviews, see: a). Trnka, T. M., & Grubbs, R. H. (2001). The development of L2X2Ru CHR olefin metathesis catalysts: an organometallic success story. *Accounts of Chemical Research*, *34*(1), 18-29. (b) Blechert, S., & Connon, S. J. (2003). Recent developments in olefin cross-metathesis. *Angew. Chem. Int. Ed.*, *42*, 1900-1923.; c). Schrock, R. R., & Hoveyda, A. H. (2003). Molybdenum and tungsten imido alkylidene complexes as efficient olefin-metathesis catalysts. *Angewandte Chemie International Edition*, *42*(38), 4592-4633.; d). Grubbs, R. H. (2004). Olefin metathesis. *Tetrahedron*, *60*(34), 7117-7140.; e). Hoveyda, A. H., & Zhugralin, A. R. (2007). The remarkable metal-catalysed olefin metathesis reaction. *Nature*, *450*(7167), 243.; f). Hoveyda, A. H. (2014). Evolution of catalytic stereoselective olefin metathesis: from ancillary transformation to purveyor of stereochemical identity. *The Journal of organic chemistry*, *79*(11), 4763-4792.

4. For more reviews, see: a). Buchmeiser, M. R. (2000). Homogeneous metathesis polymerization by well-defined group VI and group VIII transition-metal alkylidenes: fundamentals and applications in the preparation of advanced materials. *Chemical reviews*, *100*(4), 1565-1604.; b). Grela, K. (2014). *Olefin metathesis: theory and practice*. John Wiley & Sons.

5. Schwab, P., Grubbs, R. H., & Ziller, J. W. (1996). Synthesis and applications of RuCl2 (CHR ')(PR3) 2: the influence of the alkylidene moiety on metathesis activity. *Journal of the American Chemical Society*, *118*(1), 100-110.

6. Scholl, M., Ding, S., Lee, C. W., & Grubbs, R. H. (1999). Synthesis and activity of a new generation of ruthenium-based olefin metathesis catalysts coordinated with 1, 3-dimesityl-4, 5-dihydroimidazol-2-ylidene ligands. *Organic Letters*, *1*(6), 953-956.

7. a). Samojłowicz, C., Bieniek, M., & Grela, K. (2009). Ruthenium-based olefin metathesis catalysts bearing N-heterocyclic carbene ligands. *Chemical reviews*, *109*(8), 3708-3742.; b). Vougioukalakis, G. C., & Grubbs, R. H. (2009). Ruthenium-based heterocyclic carbene-coordinated olefin metathesis catalysts. *Chemical reviews*, *110*(3), 1746-1787.; c). Getty, K., Delgado-Jaime, M. U., & Kennepohl, P. (2007). An electronic rationale for observed initiation rates in ruthenium-mediated olefin metathesis: Charge donation in phosphine and N-heterocyclic carbene ligands. *Journal of the American Chemical Society*, *129*(51), 15774-15776.

8. (a) Van der Eide, E. F., & Piers, W. E. (2010). Mechanistic insights into the ruthenium-catalysed diene ring-closing metathesis reaction. *Nature chemistry*, *2*(7), 571-576.; b). Nelson, D. J.,

Manzini, S., Urbina-Blanco, C. A., & Nolan, S. P. (2014). Key processes in ruthenium-catalysed olefin metathesis. *Chemical Communications*, *50*(72), 10355-10375.

9. For computational studies of the dissociative pathway for second-generation ruthenium catalysts, see: a) Vyboishchikov, S. F., Bühl, M., & Thiel, W. (2002). Mechanism of olefin metathesis with catalysis by ruthenium carbene complexes: density functional studies on model systems. *Chemistry–A European Journal*, *8*(17), 3962-3975.; b). Cavallo, L. (2002). Mechanism of ruthenium-catalyzed olefin metathesis reactions from a theoretical perspective. *Journal of the American Chemical Society*, *124*(30), 8965-8973.; c). Adlhart, C., & Chen, P. (2004). Mechanism and activity of ruthenium olefin metathesis catalysts: The role of ligands and substrates from a theoretical perspective. *Journal of the American Chemical Society*, *126*(11), 3496-3510.; d). Minenkov, Y., Occhipinti, G., Heyndrickx, W., & Jensen, V. R. (2012). The nature of the barrier to phosphane dissociation from Grubbs olefin metathesis catalysts. *European Journal of Inorganic Chemistry*, *2012*(9), 1507-1516.
10. Grubbs, R. H., & Wenzel, A. G. (2015). O, Leary, DJ; Khosravi, E. *Handbook of Metathesis*, *2*, 246-292.
11. Zhao, Y., & Truhlar, D. G. (2008). The M06 suite of density functionals for main group thermochemistry, thermochemical kinetics, noncovalent interactions, excited states, and transition elements: two new functionals and systematic testing of four M06-class functionals and 12 other functionals. *Theoretical Chemistry Accounts*, *120*(1-3), 215-241.
12. a). Schäfer, A., Horn, H., & Ahlrichs, R. (1992). Fully optimized contracted Gaussian basis sets for atoms Li to Kr. *The Journal of Chemical Physics*, *97*(4), 2571-2577.; b). Schäfer,

A., Horn, H., & Ahlrichs, R. (1992). Fully optimized contracted Gaussian basis sets for atoms Li to Kr. *The Journal of Chemical Physics*, *97*(4), 2571-2577.; c). Schäfer, A., Huber, C., & Ahlrichs, R. (1994). Fully optimized contracted Gaussian basis sets of triple zeta valence quality for atoms Li to Kr. *The Journal of Chemical Physics*, *100*(8), 5829-5835.

13. Marenich, A. V., Cramer, C. J., & Truhlar, D. G. (2009). Universal solvation model based on solute electron density and on a continuum model of the solvent defined by the bulk dielectric constant and atomic surface tensions. *The Journal of Physical Chemistry B*, *113*(18), 6378-6396.

14. Weaver, J. H., & Frederikse, H. P. R. (1977). Crc handbook of chemistry and physics. *CRC Press, Boca Raton*, *76*, 12-156.

15. Frisch, M. J. E. A., Trucks, G. W., Schlegel, H. B., Scuseria, G. E., Robb, M. A., Cheeseman, J. R., ... & Nakatsuji, H. (2009). Gaussian 09, revision a. 02, gaussian. *Inc., Wallingford, CT*, *200*.

16. Ribeiro, R. F., Marenich, A. V., Cramer, C. J., & Truhlar, D. G. (2011). Use of solution-phase vibrational frequencies in continuum models for the free energy of solvation. *The Journal of Physical Chemistry B*, *115*(49), 14556-14562.

17. Grimme, S. (2012). Supramolecular binding thermodynamics by dispersion-corrected density functional theory. *Chemistry–A European Journal*, *18*(32), 9955-9964.

18. a). Lee, C., Yang, W., & Parr, R. G. (1988). Development of the Colle-Salvetti correlation-energy formula into a functional of the electron density. *Physical review B*, *37*(2), 785. b). Becke, A. D. (1988). Density-functional exchange-energy approximation with correct

asymptotic behavior. *Physical review A*, *38*(6), 3098.; (c) Miehlich, B., Savin, A., Stoll, H., & Preuss, H. (1989). Results obtained with the correlation energy density functionals of Becke and Lee, Yang and Parr. *Chemical Physics Letters*, *157*(3), 200-206.; (d) Becke, A. D. (1993). Density-functional thermochemistry. III. The role of exact exchange. *The Journal of chemical physics*, *98*(7), 5648-5652.

19. Check, C. E., Faust, T. O., Bailey, J. M., Wright, B. J., Gilbert, T. M., & Sunderlin, L. S. (2001). Addition of polarization and diffuse functions to the LANL2DZ basis set for p-block elements. *The Journal of Physical Chemistry A*, *105*(34), 8111-8116.
20. Alecu, I. M., Zheng, J., Zhao, Y., & Truhlar, D. G. (2010). Computational thermochemistry: scale factor databases and scale factors for vibrational frequencies obtained from electronic model chemistries. *Journal of chemical theory and computation*, *6*(9), 2872-2887.
21. a). Zhao, Y., & Truhlar, D. G. (2007). Attractive noncovalent interactions in the mechanism of Grubbs second-generation Ru catalysts for olefin metathesis. *Organic letters*, *9*(10), 1967-1970.; b). Minenkov, Y., Occhipinti, G., & Jensen, V. R. (2009). Metal− Phosphine Bond Strengths of the Transition Metals: A Challenge for DFT. *The Journal of Physical Chemistry A*, *113*(43), 11833-11844.; c). Zhao, Y., & Truhlar, D. G. (2009). Benchmark energetic data in a model system for Grubbs II metathesis catalysis and their use for the development, assessment, and validation of electronic structure methods. *Journal of chemical theory and computation*, *5*(2), 324-333.; (d) Liu, P., Xu, X., Dong, X., Keitz, B. K., Herbert, M. B., Grubbs, R. H., & Houk, K. N. (2012). Z-selectivity in olefin metathesis with chelated Ru catalysts: computational studies of mechanism and selectivity. *Journal of*

the American Chemical Society, *134*(3), 1464-1467.; e). Śliwa, P., & Handzlik, J. (2010). Assessment of density functional methods for the study of olefin metathesis catalysed by ruthenium alkylidene complexes. *Chemical Physics Letters*, *493*(4-6), 273-278.

22. For a discussion and study of the structure of tris(dialkylamino) phosphines, see: Gonbeau, D., Sanchez, M., & Pfister-Guillouzo, G. (1981). Electronic structure of tris (dialkylamino) phosphines and 1, 3-dimethyl-1, 3, 2-diazaphospholanes. A novel and critical study. *Inorganic Chemistry*, *20*(7), 1966-1973.

23. DAVIDSON, B. (1997). 1 Scandium, Yttrium and the Lanthanides The FT emission IR spectra of ScH and ScD show that a> e is 1546.9730 (14) cm-1 (H) or 1141.2650 (31) cm-1 (D). 1 An ab initio calculation has been made of the vibrational force field of ScF3 and hence of its IR and Raman spectra. 2 Similar studies were reported for MF63_, where M= Sc, Y or La, ZrF62_ and TaF6-. 3. *Spectroscopic Properties of Inorganic and Organometallic Compounds*, *30*, 277.

24. Kroshefsky, R. D., & Verkade, J. G. (1975). Staudinger reactions of aminophosphines. Influence of phosphorus basicity. *Inorganic Chemistry*, *14*(12), 3090-3095.

25. Moloy, K. G., & Petersen, J. L. (1995). N-Pyrrolyl Phosphines: An Unexploited Class of Phosphine Ligands with Exceptional. pi.-Acceptor Character. *Journal of the American Chemical Society*, *117*(29), 7696-7710.

26. a) Stoll, R. S., & Hecht, S. (2010). Artificial light-gated catalyst systems. *Angewandte Chemie International Edition*, *49*(30), 5054-5075.; b) Lüning, U. (2012). Switchable catalysis. *Angewandte Chemie International Edition*, *51*(33), 8163-8165.; c) Neilson, B.

M., & Bielawski, C. W. (2013). Illuminating photoswitchable catalysis. *ACS Catalysis*, *3*(8), 1874-1885.; d) Göstl, R., Senf, A., & Hecht, S. (2014). Remote-controlling chemical reactions by light: towards chemistry with high spatio-temporal resolution. *Chemical Society Reviews*, *43*(6), 1982-1996.; e) Blanco, V., Leigh, D. A., & Marcos, V. (2015). Artificial switchable catalysts. *Chemical Society Reviews*, *44*(15), 5341-5370.; f) Teator, A. J., Lastovickova, D. N., & Bielawski, C. W. (2015). Switchable polymerization catalysts. *Chemical reviews*, *116*(4), 1969-1992.

27. a) Leibfarth, F. A., Mattson, K. M., Fors, B. P., Collins, H. A., & Hawker, C. J. (2013). External regulation of controlled polymerizations. *Angewandte Chemie International Edition*, *52*(1), 199-210.; b) Erbas-Cakmak, S., Leigh, D. A., McTernan, C. T., & Nussbaumer, A. L. (2015). Artificial molecular machines. *Chemical Reviews*, *115*(18), 10081-10206.; c) Ogawa, K. A., Goetz, A. E., & Boydston, A. J. (2016). Developments in externally regulated ring-opening metathesis polymerization. *Synlett*, *27*(02), 203-214.; d) Chen, M., Zhong, M., & Johnson, J. A. (2016). Light-controlled radical polymerization: Mechanisms, methods, and applications. *Chemical reviews*, *116*(17), 10167-10211.; e) Corrigan, N., Shanmugam, S., Xu, J., & Boyer, C. (2016). Photocatalysis in organic and polymer synthesis. *Chemical Society Reviews*, *45*(22), 6165-6212.; f) Dadashi-Silab, S., Doran, S., & Yagci, Y. (2016). Photoinduced electron transfer reactions for macromolecular syntheses. *Chemical reviews*, *116*(17), 10212-10275.

28. Grubbs, R. H., & Wenzel, A. G. (Eds.). (2015). *Handbook of Metathesis, Volume 1: Catalyst Development and Mechanism* (Vol. 1). John Wiley & Sons.

29. (a) Dewar, J. S. (1951). A review of the pi-complex theory. *Bulletin de la Societe Chimique de France*, *18*(3-4), C71-C79.; (b) Chatt, J., & Duncanson, L. A. (1953). 586. Olefin co-ordination compounds. Part III. Infra-red spectra and structure: attempted preparation of acetylene complexes. *Journal of the Chemical Society (Resumed)*, 2939-2947.; (c) Chatt, J., Duncanson, L. A., & Venanzi, L. M. (1955). Directing effects in inorganic substitution reactions. Part I. A hypothesis to explain the trans-effect. *Journal of the Chemical Society (Resumed)*, 4456-4460.

30. a). Martinez, H., Miro, P., Charbonneau, P., Hillmyer, M. A., & Cramer, C. J. (2012). Selectivity in ring-opening metathesis polymerization of Z-cyclooctenes catalyzed by a second-generation Grubbs catalyst. *ACS Catalysis*, *2*(12), 2547-2556.; b). Irie, M. (2000). Diarylethenes for memories and switches. *Chemical Reviews*, *100*(5), 1685-1716.

31. Hillier, I. H., Pandian, S., Percy, J. M., & Vincent, M. A. (2011). Mapping the potential energy surfaces for ring-closing metathesis reactions of prototypical dienes by electronic structure calculations. *Dalton Transactions*, *40*(5), 1061-1072.

32. Cavallo, L. (2002). Mechanism of ruthenium-catalyzed olefin metathesis reactions from a theoretical perspective. *Journal of the American Chemical Society*, *124*(30), 8965-8973.

33. a) Neilson, B. M., Lynch, V. M., & Bielawski, C. W. (2011). Photoswitchable N-Heterocyclic Carbenes: Using Light to Modulate Electron-Donating Properties. *Angewandte Chemie*, *123*(44), 10506-10510.; b) Neilson, B. M., & Bielawski, C. W. (2012). Photoswitchable organocatalysis: using light to modulate the catalytic activities of N-heterocyclic carbenes. *Journal of the American Chemical Society*, *134*(30), 12693-12699.;

c) Teator, A. J., Tian, Y., Chen, M., Lee, J. K., & Bielawski, C. W. (2015). An Isolable, Photoswitchable N-Heterocyclic Carbene: On-Demand Reversible Ammonia Activation. *Angewandte Chemie International Edition*, *54*(39), 11559-11563.

34. a) Lee, P. H. M., Ko, C. C., Zhu, N., & Yam, V. W. W. (2007). Metal coordination-assisted near-infrared photochromic behavior: a large perturbation on absorption wavelength properties of N, N-donor ligands containing diarylethene derivatives by coordination to the rhenium (I) metal center. *Journal of the American Chemical Society*, *129*(19), 6058-6059.; b) Nakashima, T., Goto, M., Kawai, S., & Kawai, T. (2008). Photomodulation of ionic interaction and reactivity: reversible photoconversion between imidazolium and imidazolinium. *Journal of the American Chemical Society*, *130*(44), 14570-14575.; c) Yam, V. W. W., Lee, J. K. W., Ko, C. C., & Zhu, N. (2009). Photochromic diarylethene-containing ionic liquids and N-heterocyclic carbenes. *Journal of the American Chemical Society*, *131*(3), 912-913.; d) Duan, G., Zhu, N., & Yam, V. W. W. (2010). Syntheses and Photochromic Studies of Dithienylethene-Containing Imidazolium Derivatives and Their Reactivity towards Nucleophiles. *Chemistry–A European Journal*, *16*(44), 13199-13209.; e) Duan, G., Wong, W. T., & Yam, V. W. W. (2011). Synthesis and photochromic studies of η 6-mesitylene ruthenium (II) complexes bearing N-heterocyclic carbene ligands with the dithienylethene moiety. *New Journal of Chemistry*, *35*(10), 2267-2278.

35. Irie, M. (2000). Diarylethenes for memories and switches. *Chemical Reviews*, *100*(5), 1685-1716.

36 . a) Irie, M., Sakemura, K., Okinaka, M., & Uchida, K. (1995). Photochromism of dithienylethenes with electron-donating substituents. *The Journal of Organic Chemistry*, *60*(25), 8305-8309.; b) Fernández-Acebes, A., & Lehn, J. M. (1999). Optical switching and fluorescence modulation properties of photochromic metal complexes derived from dithienylethene ligands. *Chemistry–A European Journal*, *5*(11), 3285-3292.; c) Irie, M. (2000). Diarylethenes for memories and switches. *Chemical Reviews*, *100*(5), 1685-1716.; d) Akita, M. (2011). Photochromic organometallics, a stimuli-responsive system: an approach to smart chemical systems. *Organometallics*, *30*(1), 43-51.; e) Tsuji, Y., & Hoffmann, R. (2014). Frontier orbital control of molecular conductance and its switching. *Angewandte Chemie International Edition*, *53*(16), 4093-4097.; f) Herder, M., Schmidt, B. M., Grubert, L., Pätzel, M., Schwarz, J., & Hecht, S. (2015). Improving the fatigue resistance of diarylethene switches. *Journal of the American Chemical Society*, *137*(7), 2738-2747.; Herder, M., Schmidt, B. M., Grubert, L., Pätzel, M., Schwarz, J., & Hecht, S. (2015). Improving the fatigue resistance of diarylethene switches. *Journal of the American Chemical Society*, *137*(7), 2738-2747.; Harvey, E. C., Feringa, B. L., Vos, J. G., Browne, W. R., & Pryce, M. T. (2015). Transition metal functionalized photo-and redox-switchable diarylethene based molecular switches. *Coordination Chemistry Reviews*, *282*, 77-86.

37. For examples of switchable olefin metathesis catalysts that undergo photochemical initiation, see: a). Ben-Asuly, A., Aharoni, A., Diesendruck, C. E., Vidavsky, Y., Goldberg, I., Straub, B. F., & Lemcoff, N. G. (2009). Photoactivation of ruthenium olefin metathesis

initiators. *Organometallics*, *28*(16), 4652-4655.; b) Diesendruck, C. E., Iliashevsky, O., Ben-Asuly, A., Goldberg, I., & Lemcoff, N. G. (2010, July). Latent and switchable olefin metathesis catalysts. In *Macromolecular symposia* (Vol. 293, No. 1, pp. 33-38). Weinheim: WILEY-VCH Verlag.; Sashuk, V., & Danylyuk, O. (2016). A Thermo-and Photo-Switchable Ruthenium Initiator For Olefin Metathesis. *Chemistry–A European Journal*, *22*(19), 6528-6531.

38. For recent reports of latent, including photoinitiated, olefin metathesis catalysts, see: a). Keitz, B. K., & Grubbs, R. H. (2009). A tandem approach to photoactivated olefin metathesis: Combining a photoacid generator with an acid activated catalyst. *Journal of the American Chemical Society*, *131*(6), 2038-2039.; b). Monsaert, S., Vila, A. L., Drozdzak, R., Van Der Voort, P., & Verpoort, F. (2009). Latent olefin metathesis catalysts. *Chemical Society Reviews*, *38*(12), 3360-3372.; c). Khalimon, A. Y., Leitao, E. M., & Piers, W. E. (2012). Photogeneration of a Phosphonium Alkylidene Olefin Metathesis Catalyst. *Organometallics*, *31*(15), 5634-5637.; d) Weitekamp, R. A., Atwater, H. A., & Grubbs, R. H. (2013). Photolithographic olefin metathesis polymerization. *Journal of the American Chemical Society*, *135*(45), 16817-16820.; Naumann, S., & Buchmeiser, M. R. (2014). Latent and delayed action polymerization systems. *Macromolecular rapid communications*, *35*(7), 682-701.

39. Neilson, B. M., & Bielawski, C. W. (2013). Photoswitchable Metal-Mediated Catalysis: Remotely Tuned Alkene and Alkyne Hydroborations. *Organometallics*, *32*(10), 3121-3128.

40. Sanderson, M. D., Kamplain, J. W., & Bielawski, C. W. (2006). Quinone-annulated N-heterocyclic carbene− transition-metal complexes: observation of π-backbonding using FT-IR spectroscopy and cyclic voltammetry. *Journal of the American Chemical Society*, *128*(51), 16514-16515.

41. a) Samojłowicz, C., Bieniek, M., & Grela, K. (2009). Ruthenium-based olefin metathesis catalysts bearing N-heterocyclic carbene ligands. *Chemical reviews*, *109*(8), 3708-3742.; b) G. C. Vougioukalakis, R. H. Grubbs, Chem. Rev. 2010, 110, 1746 – 1787; c) Kelly Iii, R. A., Clavier, H., Giudice, S., Scott, N. M., Stevens, E. D., Bordner, J., ... & Nolan, S. P. (2007). Determination of N-heterocyclic carbene (NHC) steric and electronic parameters using the [(NHC) Ir (CO) 2Cl] system. *Organometallics*, *27*(2), 202-210.

42. Rosen, E. L., Varnado Jr, C. D., Tennyson, A. G., Khramov, D. M., Kamplain, J. W., Sung, D. H., ... & Bielawski, C. W. (2009). Redox-active N-heterocyclic carbenes: Design, synthesis, and evaluation of their electronic properties. *Organometallics*, *28*(23), 6695-6706.

43. Neilson, B. M., & Bielawski, C. W. (2013). Illuminating photoswitchable catalysis. *ACS Catalysis*, *3*(8), 1874-1885.

44. Roy, L. E., Hay, P. J., & Martin, R. L. (2008). Revised basis sets for the LANL effective core potentials. *Journal of chemical theory and computation*, *4*(7), 1029-1031.

45. Benitez, D., Tkatchouk, E., & Goddard III, W. A. (2009). Conformational Analysis of Olefin− Carbene Ruthenium Metathesis Catalysts. *Organometallics*, *28*(8), 2643-2645.

46. Adlhart, C., & Chen, P. (2004). Mechanism and activity of ruthenium olefin metathesis catalysts: The role of ligands and substrates from a theoretical perspective. *Journal of the American Chemical Society*, *126*(11), 3496-3510.

47. Martinez, H., Miro, P., Charbonneau, P., Hillmyer, M. A., & Cramer, C. J. (2012). Selectivity in ring-opening metathesis polymerization of Z-cyclooctenes catalyzed by a second-generation Grubbs catalyst. *ACS Catalysis*, *2*(12), 2547-2556.

48. a). Nolan, S. P. (Ed.). (2006). *N-Heterocyclic carbenes in synthesis*. John Wiley & Sons.; b). Herrmann, W. A., & Koecher, C. (1997). N-Heterocyclic carbenes. *Angewandte Chemie International Edition in English*, *36*(20), 2162-2187.; c) Herrmann, W. A. (2002). N-heterocyclic carbenes: a new concept in organometallic catalysis. *Angewandte Chemie International Edition*, *41*(8), 1290-1309.; Diez-Gonzalez, S., Marion, N., & Nolan, S. P. (2009). N-heterocyclic carbenes in late transition metal catalysis. *Chemical Reviews*, *109*(8), 3612-3676.; d) Crudden, C. M., & Allen, D. P. (2004). Stability and reactivity of N-heterocyclic carbene complexes. *Coordination chemistry reviews*, *248*(21-24), 2247-2273.

49. a). Hopkinson, M. N., Richter, C., Schedler, M., & Glorius, F. (2014). An overview of N-heterocyclic carbenes. *Nature*, *510*(7506), 485.; b). Kelly Iii, R. A., Clavier, H., Giudice, S., Scott, N. M., Stevens, E. D., Bordner, J., ... & Nolan, S. P. (2007). Determination of N-heterocyclic carbene (NHC) steric and electronic parameters using the [(NHC) Ir (CO) 2Cl] system. *Organometallics*, *27*(2), 202-210.; c) Dorta, R., Stevens, E. D., Scott, N. M., Costabile, C., Cavallo, L., Hoff, C. D., & Nolan, S. P. (2005). Steric and electronic

properties of N-heterocyclic carbenes (NHC): a detailed study on their interaction with Ni (CO) 4. *Journal of the American Chemical Society*, *127*(8), 2485-2495.

50. Neilson, B. M., Lynch, V. M., & Bielawski, C. W. (2011). Photoswitchable N-Heterocyclic Carbenes: Using Light to Modulate Electron-Donating Properties. *Angewandte Chemie*, *123*(44), 10506-10510.

51. Teator, A. J., Shao, H., Lu, G., Liu, P., & Bielawski, C. W. (2017). A Photoswitchable Olefin Metathesis Catalyst. *Organometallics*, *36*(2), 490-497.

52. Männig, D., & Nöth, H. (1985). Catalytic hydroboration with rhodium complexes. *Angewandte Chemie International Edition in English*, *24*(10), 878-879.

53. (a). Evans, D. A., Fu, G. C., & Anderson, B. A. (1992). Mechanistic study of the rhodium (I)-catalyzed hydroboration reaction. *Journal of the American Chemical Society*, *114*(17), 6679-6685.; (b). Dorigo, A. E., & von Ragué Schleyer, P. (1995). An Ab Initio Investigation of the RhI-Catalyzed Hydroboration of C = C Bonds: Evidence for Hydrogen Migration in the Key Step. *Angewandte Chemie International Edition in English*, *34*(1), 115-118.

54. Edwards, D. R., Hleba, Y. B., Lata, C. J., Calhoun, L. A., & Crudden, C. M. (2007). Regioselectivity of the Rhodium-Catalyzed Hydroboration of Vinyl Arenes: Electronic Twists and Mechanistic Shifts. *Angewandte Chemie*, *119*(41), 7945-7948.

55. Musaev, D. G., Mebel, A. M., & Morokuma, K. (1994). An ab initio molecular orbital study of the mechanism of the rhodium (I)-catalyzed olefin hydroboration reaction. *Journal of the American Chemical Society*, *116*(23), 10693-10702.

56. Widauer, C., Grützmacher, H., & Ziegler, T. (2000). Comparative Density Functional Study of Associative and Dissociative Mechanisms in the Rhodium (I)-Catalyzed Olefin Hydroboration Reactions. *Organometallics*, 19(11), 2097-2107.

57. Xi, Y., & Hartwig, J. F. (2017). Mechanistic studies of copper-catalyzed asymmetric hydroboration of alkenes. *Journal of the American Chemical Society*, *139*(36), 12758-12772.

58. a) SAccoNI, L. (1968). Five coordination in 3d metal complexes. *Pure and Applied Chemistry*, *17*(1), 95-128.; b) Gillespie, R. J. (1963). The valence-shell electron-pair repulsion (VSEPR) theory of directed valency. *Journal of Chemical Education*, *40*(6), 295.

59. Burgess, K., Van der Donk, W. A., Westcott, S. A., Marder, T. B., Baker, R. T., & Calabrese, J. C. (1992). Reactions of catecholborane with Wilkinson's catalyst: implications for transition metal-catalyzed hydroborations of alkenes. *Journal of the American Chemical Society*, *114*(24), 9350-9359.

60. Burgess, K., Van der Donk, W. A., & Kook, A. M. (1991). On deuterium-labeling studies for probing rhodium-catalyzed hydroboration reactions. *The Journal of Organic Chemistry*, *56*(9), 2949-2951.

61. Gusev, D. G. (2009). Electronic and steric parameters of 76 N-heterocyclic carbenes in Ni (CO) 3 (NHC). *Organometallics*, *28*(22), 6458-6461.

62. a) Jacobsen, E. N., Pfaltz, A., & Yamamoto, H. (Eds.). (2003). *Comprehensive Asymmetric Catalysis: Supplement 1* (Vol. 1). Springer Science & Business Media.; b). Beletskaya, I.,

& Pelter, A. (1997). Hydroborations catalysed by transition metal complexes. *Tetrahedron*, *53*(14), 4957-5026.;

63. Crudden, C. M., & Edwards, D. (2003). Catalytic Asymmetric Hydroboration: Recent Advances and Applications in Carbon− Carbon Bond-Forming Reactions. *European Journal of Organic Chemistry*, *2003*(24), 4695-4712.

64. Hayashi, T., Matsumoto, Y., & Ito, Y. (1989). Catalytic asymmetric hydroboration of styrenes. *Journal of the American Chemical Society*, *111*(9), 3426-3428.

65. Crudden, C. M., Hleba, Y. B., & Chen, A. C. (2004). Regio-and enantiocontrol in the room-temperature hydroboration of vinyl arenes with pinacol borane. *Journal of the American Chemical Society*, *126*(30), 9200-9201.

66 Doucet, H., Fernandez, E., Layzell, T. P., & Brown, J. M. (1999). The Scope of Catalytic Asymmetric Hydroboration/Oxidation with Rhodium Complexes of 1, 1′-(2-Diarylphosphino-1-naphthyl) isoquinolines. *Chemistry–A European Journal*, *5*(4), 1320-1330.

67. Kwong, F. Y., Yang, Q., Mak, T. C., Chan, A. S., & Chan, K. S. (2002). A new atropisomeric P, N ligand for rhodium-catalyzed asymmetric hydroboration. *The Journal of organic chemistry*, *67*(9), 2769-2777.

68. Schnyder, A., Togni, A., & Wiesli, U. (1997). Electronic effects in asymmetric catalysis. Synthesis and structure of model rhodium complexes containing ferrocenyl ligands for use in the hydroboration reaction. *Organometallics*, *16*(2), 255-260.

69. Chen, I. H., Kanai, M., & Shibasaki, M. (2010). Copper (I)− Secondary Diamine Complex-Catalyzed Enantioselective Conjugate Boration of Linear β, β-Disubstituted Enones. *Organic letters*, *12*(18), 4098-4101.

70. Chea, H., Sim, H. S., & Yun, J. (2009). Copper-Catalyzed Conjugate Addition of Diboron Reagents to α, β-Unsaturated Amides: Highly Reactive Copper-1, 2-Bis (diphenylphosphino) benzene Catalyst System. *Advanced Synthesis & Catalysis*, *351*(6), 855-858.

71. O'Brien, J. M., Lee, K. S., & Hoveyda, A. H. (2010). Enantioselective Synthesis of Boron-Substituted Quaternary Carbons by NHC− Cu-Catalyzed Boronate Conjugate Additions to Unsaturated Carboxylic Esters, Ketones, or Thioesters. *Journal of the American Chemical Society*, *132*(31), 10630-10633.

72. Hu, N., Zhao, G., Zhang, Y., Liu, X., Li, G., & Tang, W. (2015). Synthesis of chiral α-amino tertiary boronic esters by enantioselective hydroboration of α-arylenamides. *Journal of the American Chemical Society*, *137*(21), 6746-6749.

73 . a) Trost, B. M. (1991). The atom economy--a search for synthetic efficiency. *Science*, *254*(5037), 1471-1477.; b) Trost, B. M. (1995). Atom economy—a challenge for organic synthesis: homogeneous catalysis leads the way. *Angewandte Chemie International Edition in English*, *34*(3), 259-281.; c) Trost, B. M. (2002). On inventing reactions for atom economy. *Accounts of chemical research*, *35*(9), 695-705.

74. a) Smith, S. M., Uteuliyev, M., & Takacs, J. M. (2011). Catalytic asymmetric hydroboration of β, γ-unsaturated Weinreb amides: striking influence of the borane. *Chemical*

Communications, *47*(27), 7812-7814.; b) Moteki, S. A., Toyama, K., Liu, Z., Ma, J., Holmes, A. E., & Takacs, J. M. (2012). Two-stage optimization of a supramolecular catalyst for catalytic asymmetric hydroboration. *Chemical Communications*, *48*(2), 263-265.; c) Smith, S. M., Hoang, G. L., Pal, R., Khaled, M. O. B., Pelter, L. S., Zeng, X. C., & Takacs, J. M. (2012). γ-Selective directed catalytic asymmetric hydroboration of 1, 1-disubstituted alkenes. *Chemical Communications*, *48*(100), 12180-12182.; d) Hoang, G. L., Yang, Z. D., Smith, S. M., Pal, R., Miska, J. L., Pérez, D. E., ... & Takacs, J. M. (2015). Enantioselective Desymmetrization via Carbonyl-Directed Catalytic Asymmetric Hydroboration and Suzuki–Miyaura Cross-Coupling. *Organic letters*, *17*(4), 940-943.

75. a) Shoba, V. M., Thacker, N. C., Bochat, A. J., & Takacs, J. M. (2016). Synthesis of Chiral Tertiary Boronic Esters by Oxime-Directed Catalytic Asymmetric Hydroboration. *Angewandte Chemie International Edition*, *55*(4), 1465-1469.; b) Chakrabarty, S., & Takacs, J. M. (2017). Synthesis of Chiral Tertiary Boronic Esters: Phosphonate-Directed Catalytic Asymmetric Hydroboration of Trisubstituted Alkenes. *Journal of the American Chemical Society*, *139*(17), 6066-6069.

76. Chakrabarty, S., & Takacs, J. M. (2018). Phosphonate-Directed Catalytic Asymmetric Hydroboration: Delivery of Boron to the More Substituted Carbon, Leading to Chiral Tertiary Benzylic Boronic Esters. *ACS Catalysis*, *8*(11), 10530-10536.

77. Yang, Z. D., Pal, R., Hoang, G. L., Zeng, X. C., & Takacs, J. M. (2014). Mechanistic Insights into Carbonyl-Directed Rhodium-Catalyzed Hydroboration: ab Initio Study of a Cyclic γ, δ-Unsaturated Amide. *ACS catalysis*, *4*(3), 763-773.

78. Grimme, S. (2006). Semiempirical GGA-type density functional constructed with a long-range dispersion correction. *Journal of computational chemistry*, *27*(15), 1787-1799.

79. Gaussian 16, Revision B.01, Frisch, M. J.; Trucks, G. W.; Schlegel, H. B.; Scuseria, G. E.; Robb, M. A.; Cheeseman, J. R.; Scalmani, G.; Barone, V.; Petersson, G. A.; Nakatsuji, H.; Li, X.; Caricato, M.; Marenich, A. V.; Bloino, J.; Janesko, B. G.; Gomperts, R.; Mennucci, B.; Hratchian, H. P.; Ortiz, J. V.; Izmaylov, A. F.; Sonnenberg, J. L.; Williams-Young, D.; Ding, F.; Lipparini, F.; Egidi, F.; Goings, J.; Peng, B.; Petrone, A.; Henderson, T.; Ranasinghe, D.; Zakrzewski, V. G.; Gao, J.; Rega, N.; Zheng, G.; Liang, W.; Hada, M.; Ehara, M.; Toyota, K.; Fukuda, R.; Hasegawa, J.; Ishida, M.; Nakajima, T.; Honda, Y.; Kitao, O.; Nakai, H.; Vreven, T.; Throssell, K.; Montgomery, J. A., Jr.; Peralta, J. E.; Ogliaro, F.; Bearpark, M. J.; Heyd, J. J.; Brothers, E. N.; Kudin, K. N.; Staroverov, V. N.; Keith, T. A.; Kobayashi, R.; Normand, J.; Raghavachari, K.; Rendell, A. P.; Burant, J. C.; Iyengar, S. S.; Tomasi, J.; Cossi, M.; Millam, J. M.; Klene, M.; Adamo, C.; Cammi, R.; Ochterski, J. W.; Martin, R. L.; Morokuma, K.; Farkas, O.; Foresman, J. B.; Fox, D. J. Gaussian, Inc., Wallingford CT, 2016.

80. a) Johns, A. M., Tye, J. W., & Hartwig, J. F. (2006). Relative rates for the amination of η3-allyl and η3-benzyl complexes of palladium. *Journal of the American Chemical Society*, *128*(50), 16010-16011.; b) Trost, B. M., & Czabaniuk, L. C. (2014). Structure and Reactivity of Late Transition Metal η3-Benzyl Complexes. *Angewandte Chemie International Edition*, *53*(11), 2826-2851.; c) Carroll, A. M., O'Sullivan, T. P., & Guiry, P.

J. (2005). The Development of Enantioselective Rhodium-Catalysed Hydroboration of Olefins. *Advanced Synthesis & Catalysis*, *347*(5), 609-631.

81. a) Wucher, P., Caporaso, L., Roesle, P., Ragone, F., Cavallo, L., Mecking, S., & Göttker-Schnetmann, I. (2011). Breaking the regioselectivity rule for acrylate insertion in the Mizoroki–Heck reaction. *Proceedings of the National Academy of Sciences*, *108*(22), 8955-8959.; b) Liu, P., Montgomery, J., & Houk, K. N. (2011). Ligand steric contours to understand the effects of N-heterocyclic carbene ligands on the reversal of regioselectivity in Ni-catalyzed reductive couplings of alkynes and aldehydes. *Journal of the American Chemical Society*, *133*(18), 6956-6959.; c) Hong, X., Liu, P., & Houk, K. N. (2013). Mechanism and origins of ligand-controlled selectivities in [Ni (NHC)]-catalyzed intramolecular (5+ 2) cycloadditions and homo-ene reactions: a theoretical study. *Journal of the American Chemical Society*, *135*(4), 1456-1462.; d) Wang, T., Yu, Z., Hoon, D. L., Huang, K. W., Lan, Y., & Lu, Y. (2015). Highly enantioselective construction of tertiary thioethers and alcohols via phosphine-catalyzed asymmetric γ-addition reactions of 5 H-thiazol-4-ones and 5 H-oxazol-4-ones: scope and mechanistic understandings. *Chemical science*, *6*(8), 4912-4922.; e) Huang, G., & Liu, P. (2016). Mechanism and Origins of Ligand-Controlled Linear Versus Branched Selectivity of Iridium-Catalyzed Hydroarylation of Alkenes. *ACS Catalysis*, *6*(2), 809-820.